INVESTIGATING EFFECTS OF HEAT TREATMENT PROCESSES ON MICROSTRUCTURAL AND MECHANICAL PROPERTIES OF ADDITIVELY MANUFACTURED 18Ni300 MARAGING STEEL

A THESIS SUBMITTED TO
THE GRADUATE SCHOOL OF NATURAL AND APPLIED SCIENCES
OF
MIDDLE EAST TECHNICAL UNIVERSITY

BY

İBRAHİM AYDIN

IN PARTIAL FULFILLMENT OF THE REQUIREMENTS
FOR
THE DEGREE OF MASTER OF SCIENCE
IN
METALLURGICAL AND MATERIALS ENGINEERING

SEPTEMBER 2020

Approval of the thesis:

INVESTIGATING EFFECTS OF HEAT TREATMENT PROCESSES ON MICROSTRUCTURAL AND MECHANICAL PROPERTIES OF ADDITIVELY MANUFACTURED 18NI300 MARAGING STEEL

submitted by **İBRAHİM AYDIN** in partial fulfillment of the requirements for the degree of **Master of Science in Metallurgical and Materials Engineering Department, Middle East Technical University** by,

Prof. Dr. Halil Kalıpçılar
Dean, Graduate School of **Natural and Applied Sciences** _____

Prof. Dr. Cemil Hakan Gür
Head of Department, **Metallurgical and Materials Engineering** _____

Prof. Dr. Cemil Hakan Gür
Supervisor, **Metallurgical and Materials Engineering, METU** _____

Examining Committee Members:

Prof. Dr. Rıza Gürbüz
Metallurgical and Materials Engineering, METU _____

Prof. Dr. Cemil Hakan Gür
Metallurgical and Materials Engineering, METU _____

Prof. Dr. Bilgehan Ögel
Metallurgical and Materials Engineering, METU _____

Prof. Dr. Arcan Fehmi Dericioğlu
Metallurgical and Materials Engineering, METU _____

Assist. Prof. Dr. Kemal Davut
Metallurgical and Materials Engineering, Atılım University _____

Date: 22.09.2020

I hereby declare that all information in this document has been obtained and presented in accordance with academic rules and ethical conduct. I also declare that, as required by these rules and conduct, I have fully cited and referenced all material and results that are not original to this work.

Name, Surname: İbrahim Aydın

Signature:

ABSTRACT

INVESTIGATING EFFECTS OF HEAT TREATMENT PROCESSES ON MICROSTRUCTURAL AND MECHANICAL PROPERTIES OF ADDITIVELY MANUFACTURED 18NI300 MARAGING STEEL

Aydın, İbrahim
Master of Science, Metallurgical and Materials Engineering
Supervisor: Prof. Dr. Cemil Hakan Gür

September 2020, 91 pages

18Ni300 maraging steel (MS300) has exceptional mechanical properties due to nano-size intermetallic precipitates in martensitic matrix. It is preferred for critical aircraft components that require high strength and toughness. Very low C-content leads to good weldability and thus it is an attractive candidate for additive manufacturing (AM) techniques. In recent years, production of maraging steel components via AM techniques instead of traditional processes has gained importance in aerospace industry due to easy production of complex geometries at one step together with reduction in production time, amount of scrap, and cost. To achieve the design requirements related to the mechanical properties and to eliminate the anisotropic material behavior, the as-built parts need optimized post-AM heat treatments. Moreover, establishing easy, rapid and reliable non-destructive measurement procedures for monitoring the variations in the microstructure and mechanical properties is a challenging issue. In this study, the effects of solution and aging treatments on the microstructure and mechanical properties of 18Ni300 maraging steel that was additively produced by the selective laser melting (SLM) method were investigated. Optical microscopy, scanning electron microscopy, x-ray diffraction, hardness test, tensile test, and ultrasound velocity measurements have been performed

to characterize the specimens. The results show that as-built specimens consist of sub-micron dendritic cellular structures in the horizontal cross-section and elongated acicular structures in the vertical cross-section. Excess number of dislocations in the lath type bcc-martensite provides favorable nucleation sites for precipitates. After aging treatment, the hardness increased from 370 HV to nearly 610 HV due to precipitation of Ni_3Ti, Ni_3Mo and Fe_2Mo. Meanwhile, the ultimate tensile strength increased from 1200 MPa up to 2100 MPa with a corresponding 60 percent reduction in the % elongation. There are correlations between ultrasonic wave velocity and some mechanical properties, such as elastic modulus and hardness. This makes the sound velocity measurement a potential tool for non-destructive characterization of the microstructure and mechanical properties and monitoring of their variations in the additively manufactured and heat-treated maraging steel components.

Keywords: Maraging Steel, Additive Manufacturing, Selective Laser Melting, Heat Treatment, Non-Destructive Material Characterization, Sound Velocity

ÖZ

ISIL İŞLEMLERİN EKLEMELİ İMALAT İLE ÜRETİLMİŞ 18Nİ300 MARYAŞLANMA ÇELİĞİNİN MİKROYAPISINA VE MEKANİK ÖZELLİKLERİNE ETKİLERİNİN İNCELENMESİ

Aydın, İbrahim
Yüksek Lisans, Metalurji ve Malzeme Mühendisliği
Tez Danışmanı: Prof. Dr. Cemil Hakan Gür

Eylül 2020, 91 sayfa

18Ni300 maryaşlandırma çeliği (MS300), martensitli matriste oluşan nano boyutlu intermetalik çökeltiler nedeniyle istisnai mekanik özelliklere sahiptir. Bu çelik, yüksek mukavemet ve tokluk gerektiren kritik uçak parçaları için tercih edilmektedir. İçeriğindeki çok düşük karbon miktarı nedeniyle iyi kaynaklanabilirliğe sahiptir ve dolayısıyla katmanlı imalat teknikleri için çok uygun bir adaydır. Havacılık sektöründe, karmaşık geometrilerin tek aşamada kolayca üretilmesi ve üretim süresinin, kayıp malzeme miktarının ve maliyetin azalması nedeniyle geleneksel prosesler yerine eklemeli imalat teknikleri ile maryaşlandırma çelik parçaların üretimi önem kazanmaktadır. Mekanik özellikler ile ilgili tasarım kriterlerini sağlamak ve izotropik olmayan malzeme davranışını iyileştirmek için eklemeli imalat sonrasında optimize edilmiş ısıl işlemlerin uygulanması gereklidir. Ayrıca, mikroyapı ve mekanik özelliklerdeki değişiklikleri tespit etmek için kolay, hızlı ve güvenilir tahribatsız ölçüm prosedürlerinin oluşturulmasına ihtiyaç vardır. Bu çalışmada, seçici lazer ergitme (SLE) yöntemi ile üretilen 18Ni300 maryaşlandırma çeliğine uygulanan çözeltiye alma ve yaşlandırma ısıl işlemlerinin mikroyapıya ve mekanik özelliklere etkileri araştırılmıştır. Numuneleri karakterize etmek için optik mikroskop, tarama elektron mikroskobu, x-ışını kırınımı, sertlik testi, çekme testi ve ultrasonik dalga hızı

ölçümleri yapılmıştır. Sonuçlar, üretilen numunelerin yatay kesitte mikron altı dendritik hücresel yapılardan ve dikey kesitte ise uzatılmış asiküler yapılardan oluştuğunu göstermektedir. İğnemsi bcc-martensit fazında bulunan aşırı miktarda dislokasyon, çökeltiler için uygun çekirdeklenme alanları sağlamaktadır. Yaşlandırma tavı sonrasında, Ni_3Ti, Ni_3Mo ve Fe_2Mo intermetaliklerinin çökelmesi nedeniyle sertlik 370 HV'den yaklaşık 610 HV'ye yükselmiştir. Ayrıca, maksimum çekme dayanımı 1200 MPa'dan 2100 MPa'ya yükselmiş ve % uzama değerinde yüzde 60 azalma meydana gelmiştir. Ultrasonik dalga hızı ile esneklik katsayısı ve sertlik gibi bazı mekanik özellikler arasında korelasyonlar tespit edilmiştir. Bu sonuçlar ultrasonik dalga hızı ölçümünü, eklemeli imalat yöntemleri ile üretilmiş ve ısıl işlem uygulanmış çelik numunelerin mikroyapı ve mekanik özelliklerinin tahribatsız olarak karakterizasyonu ve meydana gelebilecek değişimlerin izlenmesi için potansiyel bir yöntem haline getirmektedir.

Anahtar Kelimeler: Maryaşlandırma Çeliği, Eklemeli İmalat, Seçici Lazer Ergitme, Isıl İşlem, Tahribatsız Malzeme Karakterizasyonu, Ses Hızı

To my beloved family …

ACKNOWLEDGEMENTS

Firstly, I would like to express my deepest gratitude to my supervisor Prof. Dr. Cemil Hakan GÜR for his guidance, understanding and continuous support throughout the study.

I am grateful to Dr. Süha TİRKEŞ for his guidance and assistance. I would not have completed this study without his support.

I would gratefully appreciate to EOS company, especially Aydın YAĞMUR for specimens supports for my thesis.

I would like to thank to my colleagues Hasan İlker YELBAY, Tuğçe KALELİ, Orcan KOLANKAYA, Seyhan ÇAMLIGÜNEY, Başak Güneş ORHAN, and Murat Tolga ERTÜRK from METU WTNDT for their help, support and interest.

I would like to thank the employees of the laboratories in Metallurgical and Materials Engineering and METU WTNDT. I am especially grateful to Yusuf YILDIRIM and Mevlüt BAĞCI, who helped in the preparation of the specimens.

I especially thank to Çağlar BAYRAK, Orhan Berk AYTUNA, Elif YEŞİLAY, Anıl ERDAL and Enver Burak ALDOĞAN for their sincere friendship during my graduate life and for giving me the strength to finish my degree by sharing all the good and the bad times. I am also grateful to Çağlar POLAT, Berkay ÇAĞAN, Esra SÜTÇÜ, Pelin GÜNDOĞMUŞ, and Seren ÖZEN. I am especially grateful to Anıl MADEN and Ahmet Faruk YILDIRIM who are my childhood friends for their support and encouragement. Additional thanks go to various friends including Enes DAĞ, Faruk AYDIN, Şevki Bekir KOCADAĞ, Süleyman Emre ÖZÖZEN, Göktan Muhammed FIRAT and Tuğçe Harika SAY who believe and support me throughout whole life.

Finally, I owe gratefulness to every individual of my beloved family for their warm support in any case. I feel so lucky to have such a great family. I wish to indicate my special appreciation to my mom and dad, Ayşe and İsmail AYDIN. I am so glad to have them. I wish to express my gratitude to my siblings Hilal and Samet AYDIN.

TABLE OF CONTENTS

LIST OF TABLES

TABLES

LIST OF FIGURES

FIGURES

LIST OF ABBREVIATIONS

ABBREVIATIONS

AM: Additive Manufacturing

3D Printing: Three-Dimensional Printing

CAD: Computer-Aided Design

MS300: Maraging Steel Grade 300

SLM: Selective Laser Melting

LBPF: Laser Powder Bed Fusion

EBM: Electron Beam Melting

DED: Direct Energy Deposition

ST: Solution Treatment

AT: Aging Treatment

DSC: Differential scanning calorimetry

TGA: Thermogravimetric Analysis

XRD: X-ray Diffraction

SEM: Scanning Electron Microscope

ToF: Time of Flight

MPa: Mega Pascal

GPa: Giga Pascal

BCC: Body Centered Cubic

FCC: Face Centered Cubic

LIST OF SYMBOLS

SYMBOLS

Å: Angstrom

°C: Degree Celsius

K: Kelvin

R_a: Arithmetic Average Roughness

M_s: Martensite Start

E_s: Energy Density

P: Laser Power

v: Scan Speed

d: Spot Diameter

⌀: Diameter

μm: Micrometer

HV: Vickers Hardness

ρ: Density

E: Elastic Modulus

G: Shear Modulus

ν: Poisson's Ratio

V_L: Longitudinal Sound Velocity

V_T: Transverse Sound Velocity

CHAPTER 1

INTRODUCTION

1.1 General

Maraging steels are special kind of high strength martensitic carbon-free iron-nickel alloys that contain a high amount of alloying elements. They are usually used in the special areas where high specific strength is required, such as rocket motor cases, landing gears, helicopter undercarriages. Maraging steels consist of martensitic structure, and their superior mechanical properties and hardness are achieved via aging treatment. At first, when maraging steels are cooled in air, soft iron-nickel bcc martensitic structure with supersaturated molybdenum and cobalt solid solution is obtained. Aging treatment at a suitable temperature hardens the matrix due to precipitation of Ni – Mo, Fe – Mo, and Fe – Ni intermetallic compounds in the martensitic structure. Thus, optimization of aging temperature and time is critical to obtain desired properties.

Recently, the production of engineering components with superior mechanical properties and high dimensional stability has become very important, especially in aerospace and aircraft industries. For this purpose, advanced manufacturing methods have gained importance. Additive Manufacturing (AM), also known as 3D printing, is used to produce physical components from a digital CAD design. AM methods have many advantages compared to traditional methods in terms of physical and mechanical properties; in some cases, also costs. Therefore, many studies related to the optimization of process parameters and heat treatment are done in AM of complex-shaped engineering components with desired properties. Due to the different microstructural features of the additively manufactured parts, optimization of heat treatment processes becomes a critical issue.

Due to their superior strength and fracture toughness with low weight, the production of some aerospace compounds from 18Ni300 maraging steel (MS300) via AM is a challenging research topic. Among the existing AM techniques, Selective Laser Melting (SLM), also known as Laser Powder Bed Fusion (LPBF), is the most used method for the production of maraging steels.

In the literature, AM of MS 300 steels are considered in terms of several aspects, such as process parameter optimization of SLM to obtain high relative density, heat treatment optimization to improve mechanical properties and to eliminate the anisotropic behavior. For instance, Caselino et al. [1] have reported that the MS300 specimens with the relative density higher than 99 % were obtained if the laser power is higher than 90 W, and scanning speed is less than 220 mm/s. Bai et al. [2] found the optimum process parameters as 160 W laser power, 400 mm/s scanning speed by conducting orthogonal experiments to obtain higher than 99 % relative density. The study of J.Mutua et al.[3] has shown that a scan speed of 700 mm/s and a laser power of 300 W resulted in a 99.8 % maximum relative density with a surface roughness (Ra) value of 35 μm.

Mutua [3] and Suryawanshi [4] have investigated the tensile anisotropic behavior of the selective laser melted MS300 specimen in both as-produced and heat-treated conditions, and they concluded that anisotropic properties in the as-built specimens disappear after heat treatment. High cooling rates of selective laser melting, between 10^3 – 10^8 K/s, make the microstructure strongly anisotropic with respect to building direction. As-built MS300 specimens do not have maximum strength and toughness. Various researches have achieved the highest mechanical properties after aging treatment by optimizing the aging temperature and time, such as Yin et al. [5], Casati et al. [6], [7], Tan et al.[8]–[10], Bai et al. [11], and Kempen et al. [12].

1.2 Aim of the Study

The objective of this study is to understand the effects solution treatment and aging treatment on mechanical properties of MS300 maraging steel specimens manufactured by selective laser melting, and to establish correlations between the hardness, elastic properties and ultrasonic wave velocity. This thesis consists of five chapters. The literature review about the additive manufacturing of maraging steels and their post heat treatment is given in Chapter 2. In Chapter 3, the experimental setup and the principles of the characterization methods are introduced. In the fourth chapter, the results are presented and discussed focusing on microstructural and mechanical aspects. Finally, the conclusions and recommendations for future studies are given in Chapter 5.

CHAPTER 2

LITERATURE REVIEW

2.1 Additive Manufacturing

2.1.1 Introduction

Additive Manufacturing (AM) is one of the novel manufacturing technologies used for the production of 3D objects layer by layer from the CAD model. Because of its production speed and method, it is also called as Rapid prototyping (RP). In ASTM standards, this method is described as " a process of joining materials to make objects from 3D model data, usually layer upon layer, as opposed to subtractive manufacturing methodologies" [13]. The final product with high dimensional tolerances, which does not require any other process, can be obtained with AM technology. In parallel to the development of computers, software, lasers, and machines, the applicability of AM is increasing continuously. Nowadays, considerable numbers of engineering components are manufactured via additive manufacturing technology from all types of materials.

AM technologies based on the model which is generated by using a 3D Computer-Aided Design (CAD) system. 3D objects are produced from this model without any extra process planning. In conventional manufacturing methods, part geometries and dimensions must be analyzed in detail to specify each step of process plans. In other words, what tools, fixtures, and machines must be used at which stage must be identified in advance, and each step must be controlled carefully to obtain parts with desired properties in conventional methods. However, it is not needed for additive manufacturing technology. After the creation of the 3D CAD model, AM enables mass production of parts with high dimensional accuracy if how additive manufacturing machines works will be clearly understood [14].

The basic principle of AM technology is based on obtaining the whole part by adding the layers, which are thin cross-sections of the part. The geometry of the part is identified in the 3D CAD model, and it is divided into layers. The thicknesses of each layer are determined from the final shape of the produced part. Nowadays, all AM methods use a layer-based approach. The only differences between them are the used materials, the creation way of layers, the technique used for bond each layer such as melting or deposition. These differences determine the dimensional accuracy and not only the physical but also mechanical properties of final products. Moreover, production speed and cost also differentiate with manufacturing methods [15].

Generally, additive manufacturing can be identified as the production of final parts from a 3D CAD model in one step. Although there are different AM types and devices, AM methods involve a series of steps that are nearly same for all types. These process sequences are [16][17];

i. Generation of Computer-Aided Design model

ii. Conversion of 3D CAD model to Stereolithography (STL) format

iii. Manipulation of STL file to AM machine

iv. Adjusting of AM device setup

v. Building of the part

vi. Removal of the part from the device and cleanup

vii. Post-processing of the part, such as painting, polishing, or sandpapering

viii. Usage of the part in application

2.1.2 Advantages of Additive Manufacturing

Conventional manufacturing methods such as casting, forging, and machining have some disadvantages like long production times and high material wastage due to the subtractive nature of the processes. It is not possible to manufacture a complicated shaped part in one step with conventional methods. Since these drawbacks of traditional manufacturing methods can be eliminated with AM technologies, they are accepted as a *next-generation technology.* Additive manufacturing enables mass production of engineering components in a short time with high dimensional accuracy and minimum material wastage. Moreover, since it does not require any further processing at the end of production and it does not depend on any other facilities, manufacturing with AM technology reduces production and shipping costs [16]–[19].

The remarkable advantages of AM are their production speed, design freedom, cost-saving, energy saving, material saving, and green manufacturing [16].

2.1.3 Additive Manufacturing Methods

There is a continual development of AM methods for all types of materials since the requested properties in engineering applications are increasing. Since, AM methods used for one material type could not be used for others. Several AM methods are available, that differ from each other in terms of layer deposition type, operating principle, and form of initial material. While melting or softening of materials is the main principle in selective laser sintering (SLS) or selective laser melting (SLM) to produce each layer, curing of liquid materials can be used in other methods, e.g., stereolithography (SLA) [17], [20], [21], [22]. A classification of AM methods in terms of raw material is shown in Figure 2.1.

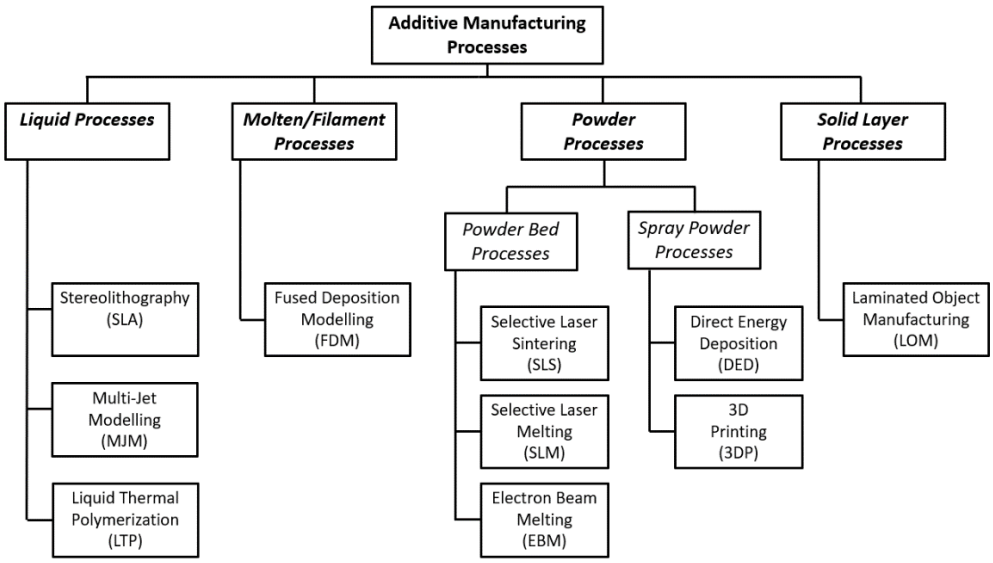

Figure 2.1. Additive manufacturing process types in terms of raw materials [23]

The additive manufacturing processes can also be divided into five groups in terms of operating principle which are summarized in Figure 2.2 [22].

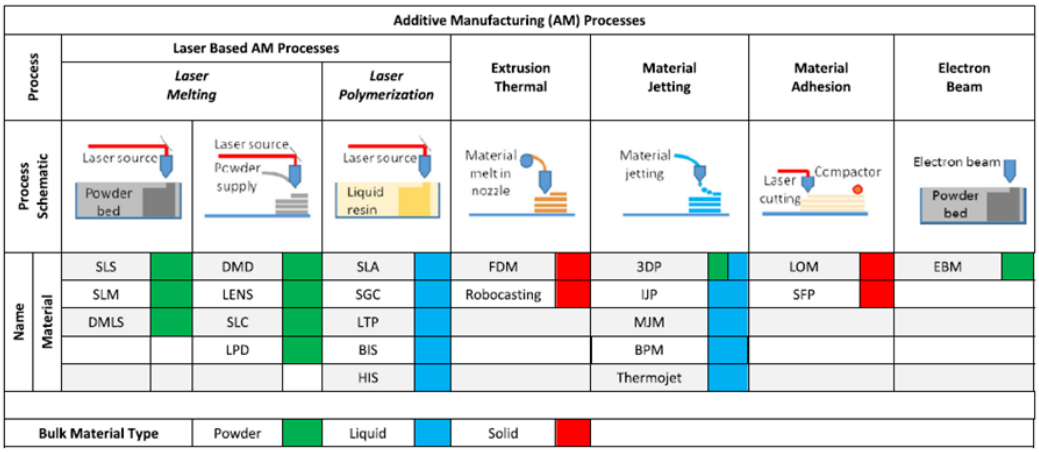

Figure 2.2. Additive manufacturing process categorization [22]

Laser-based additive manufacturing processes are divided into two groups depending on phase change mechanisms: laser melting and laser polymerization In this method, a low to the medium voltage laser beam is used to melt, solidify, or cure raw materials. The principle of laser polymerization depends on the phase change principle. The liquid photosensitive resin is cured with a laser beam source by applying UV radiation. Stereolithography (SLA), solid ground curing (SGC), liquid

thermal polymerization (LTP), beam interference solidification (BIS) and Holographic interference solidification (HIS) are the subgroups of laser polymerization processes [24], [25]. On the other hand, in the laser melting processes, raw materials in the powder form are supplied directly to the processing head, and these fine powders are selectively melted with the laser beam. Then, melted materials cool down and solidify in the form of the final shape. Selective laser sintering and selective laser melting are the most well-known types of this group. They are very similar to each other, and the only difference between them is the full melting of the powder in selective laser melting (SLM) and Direct Metal Laser Solidification (DMLS) and partial melting in SLS [19]. Laser engineered net shaping (LENS), Direct metal deposition (DMD), Laser powder deposition (LPD) and Selective laser cladding (SLC) are the other types of laser-based processes.

In the thermal extrusion processes, generally, wire-shaped plastics are used. During manufacturing, raw materials are melted or softened in the heated extrusion nozzle. After being melted, the material passes through an extrusion nozzle that deposits the material, which then cools off in order to solidify and form the final part geometry. Fused Deposition Modelling (FDM) and Robocasting are the examples of this process [26].

In the material jetting process, thin nozzles are used to spray the molten materials or a binder. This adhesive liquid binder allows the powders to bind layer by layer to form a solid object. On the other hand, if the binder is not used, liquid raw material droplets are used to build the solid object layer by layer through the inkjet head. These jetted droplets are then cured by passing a UV light through each layer. The operating principle of this process is very similar to laser melting processes. Instead of phase transformation, the binder holds the powder particles together [27]–[30].

Adhesive based processes such as laminated object manufacturing (LOM) and solid foil polymerization (SFP) include a laser cutter and a bonding tool. Sheet layers of parts are obtained by cutting the thin films of raw materials into the desired shape with a laser cutter, and then these layers are fused by using heat and pressure.

Although this process is the fastest AM process, due to its drawbacks related to mechanical properties, dimensional accuracy and surface quality, it has limited use [29], [31], [32].

The electron beam melting process(EBM) is very similar to the SLM method. The only difference is that an electron gun is used for melting or sintering of raw material powders instead of a laser beam. Since the building rate in EBM is higher than that in SLM, this process is more powerful in the production of metallic parts. Due to the oxidation problems, the process takes place under vacuum by applying 30 – 60 kV [21], [33], [34].

2.1.4 Selective Laser Melting

2.1.4.1 Background

The history of the Selective Laser Melting (SLM) dates back to the 1990s. This method has been developed in collaboration F & S Stereolithographietechnik GmbH and the Fraunhofer ILT. The aim of the process is the production of engineering components from the powders by using a high-intensity laser beam to melt selective regions of powder. Then, the melted regions are fused layer by layer, and the final shape is obtained. The patent for this technology was first applied in 1997 to the German Patent and Trade Mark Office and published in 1998 [35].

The process sequences given in Part 1.1 is also valid for selective laser melting. Firstly, it is necessary to create a model of the part to be built by using Computed Aided Design (CAD) software. Since algorithmics of CAD software differs from each other, STereoLithography (STL) format is adapted to the AM industry in order to establish consistency. So that secondly, CAD files are converted to the STL format which represents the 3D geometries in triangular representation. Surfaces of the part are divided into slices, and the whole part is produced by scanning of laser in each layer. The next step is the production of the part. In this step, metal powders are layered finely on a substrate plate of the SLM machine, and after that, selected areas are melted and fused according to STL data by using a high-intensity laser beam.

Once the first layer is completed, the powder is supplied as a second layer, and at that time, the laser starts to scan in this layer, and this process continues in this way until the entire part is created. Layer thicknesses usually range from 20 to 100 micrometers. While choosing the layer thickness, two parameters are essential; good powder flowability and fine resolution. There should be a balance between them. If powders have large sizes, resolution and dimensional tolerances become poor. On the other hand, if particle size becomes smaller, the agglomeration problem can be seen due to the van der Waals forces which result in poor powder flowability and hence reduced powder deposition. After all steps are finished, unmelted metal powders are removed from the chamber, and the final part is removed from the plate. Removal can be done manually or by using EDM. The production sequences of SLM are shown in Figure 2.3. Note that oxidation can be a problem in selective laser melting since specimens heated at high temperatures are cooled with the cooling rates up to 10^8 K/s. For this reason, nitrogen or argon gases are used as inert gases in the building chamber to prevent oxidation. [16], [36].

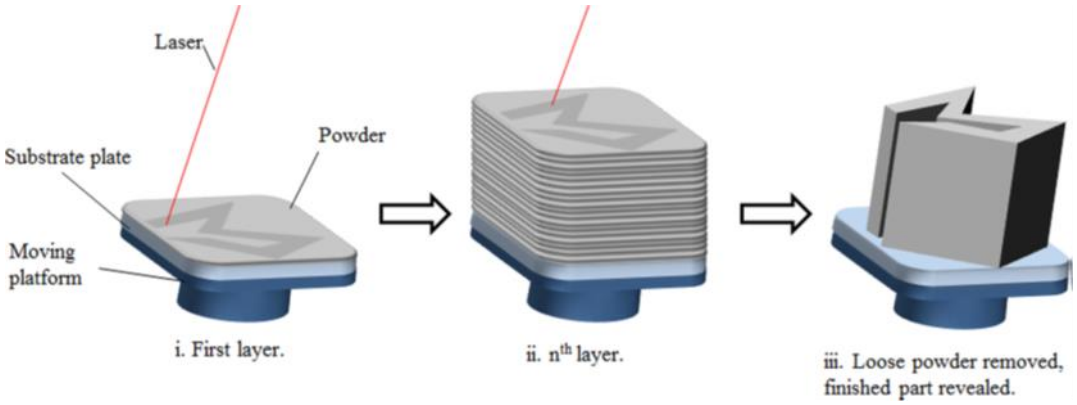

Figure 2.3. Schematic view of Selective Laser Melting [37]

2.1.4.2 Effect of Process Parameters

The adjustment of process parameters is very critical in SLM to obtain high-density components without any defect. These parameters are laser power, scanning speed, hatch spacing and layer thickness, and they affect the melting depth.

2.1.4.2.1 Laser Power and Scan Speed

One of the critical parameters for SLM is laser power. However, the properties of produced parts are not directly related to laser power. In this case, the energy density (E_s) term must be considered since the depth of melting is strongly related to E_s. It depends on not only the laser power (P) but also spot diameter (d) and scan speed (v). This relationship is given in Equation 2.1.

$$E_s = \frac{P}{vd} \qquad \textit{Equation 2.1}$$

Depth of melting increases with increasing energy density, but in some cases, different properties might be obtained at the same energy densities which have different laser power, scan speed and spot size. In this condition, the effect of laser power is much stronger than other parameters and also the effect of the spot size is a negligible amount. A decrease in laser beam diameter decreases the melting depth slightly [19], [38].

As the energy density of laser increases, the relative density of AM parts also increases. In this case, relative density is strongly affected by scan speed rather than laser power. This can be explained by the reduction of the width of the laser melt lines with decreasing scan speed [19], [38].

2.1.4.2.2 Scan Pitch

Metallic bonding between tracks and porosity is affected by the scan pitch. To ensure good bonding and minimum porosity, it must be smaller than the width of the track which depends on not only the laser beam size but also the laser density energy. While track width is wider than laser beam size at high laser energy density, it becomes smaller than that at low energy density. To ensure good bonding and minimum porosity, a 30 % overlap is recommended [39], [40].

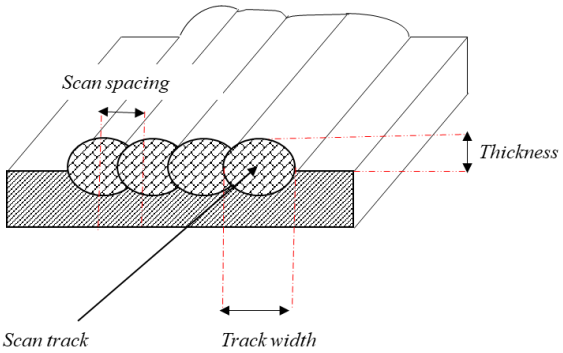

Figure 2.4. The geometry of the scanned track

2.1.4.2.3 Layer Thickness

Melted layer thickness during manufacturing must be adjusted to obtain excellent surface properties and bonding. Also, production is strongly depended on the layer thickness. An increase in laser energy density, in other words, decreasing scan speed or increasing laser power, increases the laser melted layer thickness.

During SLM, it is essential to re-melt the previous layer. If proper re-melting does not happen, metallic bonding between layers is not completely achieved, and the formation of voids is seen. This situation is illustrated in Figure 2.5. In this figure, the layer thickness is the same, but in Figure 2.5 (a), the previously deposited layer is not melted, and the formation of voids is seen. However, in the second scanning path, overlapping between formed and deposited layers are provided by re-melting of the previously formed layer, and good bonding is obtained.

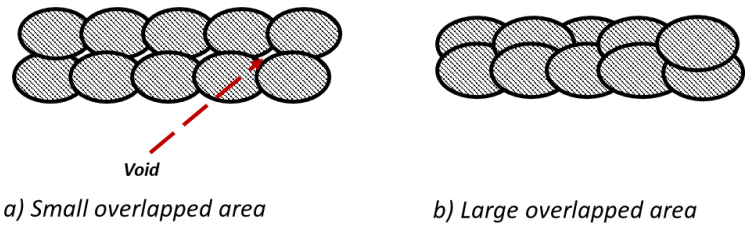

Figure 2.5. Types of scanned layers: (a) poor bonding between the two adjacent layers and (b) good bonding between the two adjacent layers

To conclude, optimization of process parameters is very critical to build a fully dense part with desired property and surface quality. If energy density becomes insufficient, a lack of wetting between the deposited layer and the molten pool is

seen, and this is called as balling [39]. However, high laser and low scanning speed may result in extensive material evaporation and the keyhole effect [41]. Besides, poor scan spacing causes the formation of porosity due to the incomplete fusion of melt lines [42].

2.1.4.3 Materials in SLM

According to the research of C. Y. Yap et al. [37] which is based on research publications on SLM, LaserCusing, and DMLS indexed by Web of Science and ScienceDirect from 1999 to 2014, it is seen that SLM research focuses mostly on iron, titanium, nickel and their alloys (Figure 2.6). The popularity of these metals is caused by their widespread applications in aerospace and medicine industries and also their cost. Besides, aluminum, copper, magnesium, and tungsten are other metals tested for selective laser melting. While steel and titanium alloys correspond with 58 % of all publications about selective laser melting, ceramics and composite materials account for about 15 %.

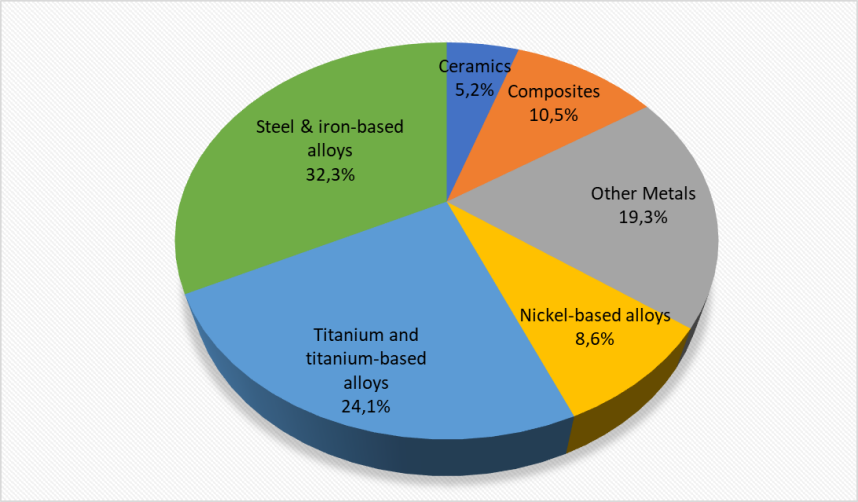

Figure 2.6. Research publications on SLM of various materials [37]

SLM process has been successfully applied for several metals and their alloys in the literature, Fe-based alloys, 316L [43]–[46] and PH 17-4 [47]–[49], Ti-based alloys, CP-Ti [50]–[52], Ti-6Al-4V [51], [53]–[55] and Ti-13Nb-13Zr [51], [56], and Al-based alloys, Al-12Si [57]–[59] and AlSi10Mg [60]–[62].

2.2 Maraging Steel

2.2.1 General

Maraging steels are one special kind of Iron – Nickel steel alloy used mainly in aerospace and aircraft applications due to their high specific strengths. Other characteristic properties of them are their ultrahigh strength with high fracture toughness, good weldability and excellent dimensional stability at high temperatures [63]. Due to their characteristic properties such as their extremely low carbon content and/or high nickel content, maraging steels are alternative for medium to high carbon steels. Quench cracking, which is a risk for medium and high carbon steels is not critical for maraging steels because of their low carbon content. Moreover, corrosion resistance of maraging steels is higher than that of medium and high carbon steels since carbide formation is not seen [64].

History of the maraging steels dates back to the 1950s. Clarence Bieber found 20 % and 25% Ni maraging steels while working on iron-nickel magnetic alloys [65]. These steels included Aluminum, Titanium and Niobium, and they provided precipitation hardening of martensitic microstructure and both steels in the study of Bieber have 55 to 56 HRC hardness [66]. However, in the study of Hall, it is mentioned that brittleness of these alloys is a problem at extremely high strength levels so that their usage was restricted [67]. Raymond F. Decker, the first person who used maraging term, comes from the aging of the martensite phase which has an acicular structure in the microstructure and his coworkers Eash and Goldman found that addition of cobalt and molybdenum leads to hardening of martensite to significant levels [68].

Maraging steels are further hardened via precipitation of intermetallic compounds during aging [69]. 18% Ni maraging steels have commonly used ones since when Ni content exceeds 18%, retention of austenite in as quench condition is observed [70]. They are usually described with some numbers such as 200, 250, 300, 350 that designate the approximate yield stress in ksi in the aged condition. The well-known maraging steel types and their mechanical properties in the aged conditions are listed

in ***Table 2.1***. In the late 1970s, due to a decrease in the availability of cobalt and an increase in the cost of cobalt, maraging steels have been developed with low cobalt content, but properties of these steels are not as good as cobalt-containing ones. [71], [72].

Table 2.1 Achievable maximum mechanical properties of maraging steels after optimum heat treatments [73]

Grade	Yield Strength (MPa)	Tensile Strength (MPa)	Elongation (%)	Fracture Toughness (MPa√m)
18Ni200	1400	1500	10	155 – 240
18Ni250	1700	1800	8	120
18Ni300	2000	2050	7	80
18Ni350	2400	2450	6	35 – 50
18Ni (Cast)	1650	1750	8	105
Cobalt-free 18Ni250	1825	1895	11.5	127
Low-cobalt 18Ni250	1780	1835	11	149

The maraging steels contain maximum 0.03 % C, 17 - 19 % Ni, 8 – 12 % Co, 3 – 5 % Mo, 0.2 - 1.8 % Ti and 0.1 – 0.15 % Al. Typical nominal compositions are given in ***Table 2.2***. The most distinctive feature of them is their extremely low carbon content. Thus, instead of carbide precipitation such as TiC which affects mechanical properties adversely, precipitation of intermetallic compounds such as Ni_3Mo, Ni_3Ti, Ni_3Al and Fe_2Mo are observed. This improves strength, toughness, hardenability and formability. Moreover, cobalt plays an important role in maraging steels. The uniform distribution of precipitates in the martensitic matrix is provided by cobalt. Also, cobalt speeds up the precipitation process so that the aging time needed to reach the desired hardness value is shortened. By the addition of cobalt, molybdenum solubility reduces so that the amount of Mo-rich precipitates increases in the

existence of cobalt during aging [73]. Besides, due to the low carbon content of maraging steels, instead of ordinary martensite (BCT) which is obtained by quenching in medium to high carbon steels, maraging steels have a lath-like BCC martensitic structure. This structure is tougher and softer than the ordinary ones and also heavily dislocated which means Fe-Ni BCC martensite has a high dislocation density (high energy) and these dislocations create favorable site for precipitation.

There have been many debates about martensitic transformation in maraging steels and its effect on strengthening with aging. It is generally agreed that about half of the strength of the maraging steels is derived from the Fe-Ni BCC martensite formed upon cooling from annealing temperature. After aging of this structure, strength of the maraging steels doubled because of the precipitation of Ni_3Mo that is associated with the martensite sub-boundaries and the precipitation of the small isolated Ni_3Ti intermetallic compounds.

Table 2.2 Nominal compositions (wt %) of commercial maraging steels [63]

Grade	**Ni (wt %)**	**Mo (wt %)**	**Co (wt %)**	**Ti (wt %)**	**Al (wt %)**
18Ni200	18	3.3	8.5	0.2	0.1
18Ni250	18	5.0	8.5	0.4	0.1
18Ni300	18	5.0	9.0	0.7	0.1
18Ni350	18	4.2	12.5	1.6	0.1
18Ni (Cast)	17	4.6	10.0	0.3	0.1
Cobalt-free 18Ni200	18.5	3.0	-	0.7	0.1
Cobalt-free 18Ni250	18.5	3.0	-	1.4	0.1
Low-cobalt 18Ni250	18.5	2.6	2.0	1.2	0.1
Cobalt-free MS300	18.5	4.0	-	1.85	0.1

2.2.2 Physical Metallurgy of Maraging Steels

Strength and toughness of maraging steels are higher than those of other steel types, as can be seen in Figure 2.7. Due to the age hardening of low carbon, the martensitic structure is extremely ductile. There are two important achievements provided by aging.

i. Formation of uniformly distributed fine intermetallics precipitates which strengthen the martensitic matrix
ii. Reduction or elimination of the reversion of metastable martensite to austenite

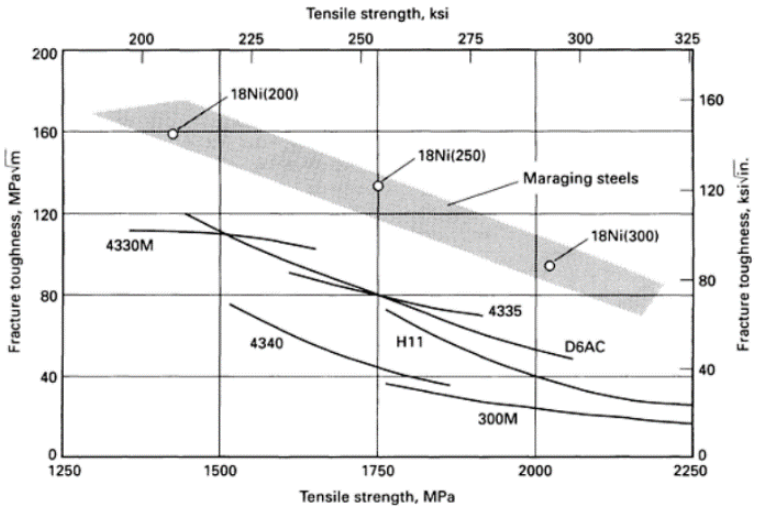

Figure 2.7. Strength/toughness combination of MS300 steels compared to conventional high-strength carbon steels [67]

There exists a great interest in the industry to the materials strengthened by intermetallic precipitates due to their specific features. Specifically, they differ from carbides in the following ways [74]:

1. Intermetallics distribute into the matrix more uniformly in comparison to carbides since no eutectic transformation is needed to form precipitates; they form during primary crystallization. Thus, their effects on strength and ductility are less detrimental.

2. Intermetallics precipitate from the supersaturated solution during aging. The following main features are observed between the precipitation of intermetallics and the precipitation of carbides;

(i) There exists a significant dispersion of formed intermetallic precipitates having less than 5 to 20 nm average size with the 100 nm average distance.

(ii) Relatively uniformly distributed precipitates are obtained in the carbon-free or low-carbon matrix, especially when Ni is present in the solution. So, weaker embrittlement effect is seen the precipitation hardening in comparison with carbide strengthening. However, an increase in the volume fraction of intermetallics causes more embrittlement.

(iii) Precipitated intermetallics strengthen the martensitic matrix more than the carbides due to their homogeneous dispersion with higher volume fractions. While 20 – 40 HRC hardness increment can be achieved by precipitation hardening, it is 3 – 10 HRC with carbide strengthening.

3. The precipitation hardening temperatures for obtaining the maximum hardness depends on the type of precipitated intermetallic compounds. For martensitic steels, $(Fe,Ni,Co)_7(Mo,W)_6$ and $(Fe,Cr)_3(Ti,Al)$ intermetallic compounds precipitate around at 500 – 550 °C and $(Fe,Co)_7(W,Mo)_6$ precipitate around at 580 – 650 °C. On the other hand, in austenitic alloys, precipitation of these compounds takes place at higher temperatures (750 – 800 °C and higher). For that reason, carbon-free martensitic steels can acquire higher hardness up to 68–69 HRC and improved thermal stability depending on the type of intermetallics. However, austenitic steels have still better thermal stability, but lower hardness.

4. During precipitation, the hardness of nickel-containing steels increases intensively at the first 10 –15 minutes, while 30 – 40 minutes is required for carbide strengthening.

5. Precipitate coarsening and therefore, hardness reduction occurs at higher aging temperatures in comparison to carbides.

2.2.2.1 Phases in Maraging Steels

Maraging steels usually consist of the following microstructural constituents;

i. BCC lath-like martensite (α-phase) with very low amount of C
ii. Retained and reverted austenite (γ-phase)
iii. Nanosized intermetallic precipitates (Ni_3Ti and Ni_3Mo)
iv. Laves phase (Fe_2Mo)

Maraging steels receive their excellent mechanical properties after suitable heat treatments. Firstly, they are solutionized at around 1000 °C and then cooled to room temperature in air. When quenching after solution treatment, transformation of austenite to Fe-Ni BCC martensite which is a soft and heavily dislocated takes place. It has a lath type and forms a packet consisting of many small sized laths arranged parallel to each other. Each prior austenite grain includes several lath packets. Moreover, retained austenite can be present in the structure after quenching depending upon the nickel content. Besides this retained austenite, reverted austenite can also be found. Reverted austenite formation depends on not only the chemical composition of steels, but also the aging time and temperature. It emerges from martensite during aging at temperatures below the global $\alpha \rightarrow \gamma$ transformation temperature. This is the temperature where the entire material transforms, which is significantly higher than the local temperature because of Ni-enrichment [74].

2.2.2.2 Precipitation in Maraging Steels

The hardening mechanism of maraging steels is based on the precipitation of the intermetallics during aging. Types of intermetallics formed during aging change with aging temperature and time since they are not stable and the composition of intermetallic changes due to diffusion of elements. Also, longer aging times result in the dissolution of intermetallics and formation of the equilibrium composition of martensite and austenite [75]. The main alloying element in maraging steel alloys is nickel and strengthening enhanced due to intermetallics formed by Ni with molybdenum, titanium and aluminum. Ultrafine needle-shaped $Ni_3(Mo,Ti)$ are the

main intermetallics that strengthen maraging steel, and they have high resistance to coarsening. The other precipitate, a spherically shaped Fe_2Mo, also strengthens the matrix, but it is formed in the overaged conditions. Also, the solubility of molybdenum reduces with the addition of Co and fraction of Mo-rich intermetallics increases [76]. The typical phases and intermetallic compounds observed in maraging steels are listed in Table 2.3.

Table 2.3 Phases found in maraging steels [77]

Phase	Stoichiometry	Crystal Structure	Lattice parameters
Austenite	γ-Fe	FCC	a = 3.5852 Å
Martensite	α-Fe	BCC	a = 2.8812 Å
Ni_3(Ti, Mo)	A_3B	Hexagonal	a = 5.101 Å c = 8.307 Å
Ni_3Mo	A_3B	Orthorhombic	a = 5.064 Å b = 4.224 Å c = 4.448 Å
X	A_3B	Hexagonal	a = 2.55 Å c = 8.30 Å
ω	A_2B	Hexagonal	a = 3.9 – 4.05 Å c = 2.39 – 2.48 Å
μ	A_7B_6	Rhombohedral	a = 4.751 Å α = 30.38 °
S	A_8B	Hexagonal	a = 7.04 Å c = 2.48 Å
Fe_2Mo (Laves phase)	A_2B	Hexagonal	a = 4.745 Å c = 7.754 Å

At different aging temperatures and times, various phases and intermetallics may form. At low aging temperatures (between 400 °C to 450 °C), coherent phases like X, S and μ were formed in the martensitic matrix [78]–[80]. When the aging temperature is higher than 450 °C, hardening is provided due to the precipitation of Ni_3(Ti, Mo) and Fe_2Mo intermetallics [75], [81]. Moreover, aging between 500 °C and A_s temperature results in over-aging and austenite formation by a diffusion-controlled reaction [82], [83]. Laves phases formed at higher aging temperatures have also been observed. According to Li and Yin [84], the austenite formation occurs at the same moment and as a consequence of the partial dissolution of Ni_3(Ti,Mo) and precipitation of Fe_2Mo.

2.2.2.3 Austenite Reversion in Maraging Steels

Austenite reversion is essentially seen in all types of maraging steels; however, transformation temperature varies with the steel type since transformation temperature and austenite reversion rate are quite sensitive to the chemical composition. As opposite to precipitation strengthening, austenite reversion leads to loss of strength. Even, reduction in strength is associated with austenite reversion rather than precipitate coarsening. This reversion is caused by the nickel enrichment of the martensite matrix [85], [86].

During the aging of maraging steels, several types of precipitates are formed, and they provide the strengthening of the matrix. Ni_3Mo precipitate which has orthorhombic Cu_3Ti type structure and Ni_3Ti are the primary precipitates responsible for age hardening. With the formation of these precipitates, Ni amount in the matrix decreases. Their formation is initially favored over other types of precipitates such as Fe_2Mo due to their convenience between the bcc martensitic matrix, and they precipitate quickly during aging. However, as the aging time increases, Ni_3Mo precipitate starts to grow and also coherence strain between precipitate and matrix increases. When this strain arrives a critical level where Ni_3Mo precipitates have lost their stability. At this point, since Ni_3Mo precipitates are unstable, they start to dissolve and also Fe_2Mo precipitates formed at the same time. With the dissolution of Ni_3Mo, Ni enrichment in the matrix takes place, and also this enrichment is enhanced with the formation and growth of Fe_2Mo. Nickel is known as austenite stabilizer and Ni-enrichment in the matrix leads to a decrease in martensite start temperature (M_s) so that austenite remains in the microstructure. Austenite reversion can be defined as decomposition of Fe-Ni metastable martensitic matrix to the austenite by diffusion-controlled reaction at temperatures below austenization start temperature (A_s) [69], [87].

Formation of reverted austenite takes place with a diffusion mechanism followed by rapid shearing or with both actions of diffusion and shear mechanisms simultaneously. Reverted austenite firstly starts to form in a thin shell around the

retained austenite regions or at the martensite platelet boundaries. After the reaction has progressed enough, lamellar structure with elongated austenite ribbons along boundaries and also smaller austenite pools within the platelets appear [69], [88].

2.3 Additive Manufacturing of Maraging Steels

Additive manufacturing is focused on the production of complex-shaped engineering components with high quality in generally the biomedical and aerospace industry. Nowadays, instead of conventional methods, additive manufacturing of maraging steel components gain importance due to their superior mechanical properties. In addition to their superior mechanical properties, their excellent wettability and low reflectivity make them very suitable for additive manufacturing, especially for powder bed fusion techniques such as selective laser melting, which is also known as laser powder bed fusion (LPBF). In this section, additive manufacturing of MS300 maraging steels are summarized in terms of microstructure and mechanical properties for SLM.

2.3.1 Densification Phenomena

The densification level of additively manufactured material is very critical for the resultant mechanical properties of parts and their performances. The relative density of parts is strongly affected by process parameters such as laser power, scan speed, pitch diameter, and spot diameter. For this reason, process parameter optimization studies for additive manufacturing of MS300 maraging steels have conducted. Bai et al. [2] designed the orthogonal experiment to study the influence of process parameters by choosing laser power as 100 – 190 W, scanning speed as 300 – 600 mm/s and scanning space as 0.05 to 0.11 mm. They concluded that relative density firstly increases with the increasing laser power, scanning speed and scanning space at a certain level and then decreases since low energy density which is provided at lower laser power with higher scanning speed leads to insufficient melting of metal powder while high energy density obtained with high laser power and low scanning speed leads to voids formation due to spatter and vaporization. Also, relative density decreases with bigger scanning spaces because of insufficient melting of powders.

Huang et al. [89] conducted the orthogonal experiments to investigate the relationship between the SLM process parameters and the relative density. Their outcome is very similar to the results of Bai et al. They ranked the importance order of process parameters as laser power, scanning distance, scanning speed and powder thickness, respectively. The optimal process parameters were found as 260 W laser power, 700 mm/s scan speed, 0.11 mm scan pitch, and 0.02 mm powder thickness. When laser power increases up to 260 W, powders have higher fluidity due to abundant received energy so that internal pores close up, but when laser power exceeds 260 W, powders receive too much energy, and this causes vaporization and over burn of powders. Also, the effect of laser speed explained as at lower scanning speeds, the laser stays on powder longer times, and powders melt fully, so the amount of formed porosity becomes very small. If laser speed becomes very low, powders can be vaporized and cause the formation of pores. When scanning space increases, a sufficient amount overlap is not provided, and each layer becomes uneven, but flat layers are obtained at small scanning spaces because of the overlap of the melt channels. Mutua et al. [3] found the optimum process parameters as scan speed of 700 mm/s, laser power of 300W, overlap rate of 40%, and energy density of 71.43 J/mm^3. Also, Yao et al. [90] concluded that when the energy density was over 180 J/mm^2, the parts with 100 % relative density can be manufactured.

2.3.2 Microstructure of Additively Manufactured Maraging Steels

Maraging steel parts with nearly 99.9% relative density can be produced [1], [2], [12], [64], [89]–[96], [3], [97]–[106], [5], [107]–[111], [6]–[11]. Additively manufactured maraging steels have completely different microstructure than conventionally produced ones that have fully lath martensitic structure [72], [101]. Their microstructure consists of fine dendritic cellular solidification with the cell size of 0.2 to 0.6 μm for laser powder bed deposition and 5 μm for direct energy deposition and elongated acicular microstructure along building direction due to rapid solidification with higher cooling rate [1], [12], [22], [23], [49], [52], [79], [112]. The formation of this solidification microstructure is due to the martensitic

phase transformation. The as-built microstructure of additively manufactured MS300 maraging steel is shown in Figure 2.8.

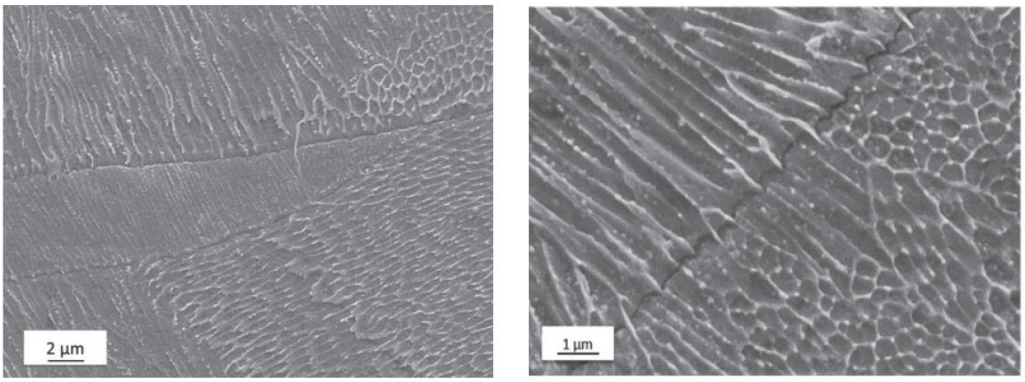

Figure 2.8. SEM micrographs of the as-built MS300 steel [7]

This microstructure looks rather different from wrought maraging steels. Individual solidification cells include the martensite lath blocks and retained austenite often confined along cell boundaries. The formation of retained austenite is a consequence of nickel enrichment during solidification due to micro segregation in the intercellular regions [101], [113]. This situation is explained more clearly in the study of Jägle et al. [101]. As can be seen in Figure 2.9 (a), retained austenite (red areas in Figure 2.9 (a)) is exactly located in the intercellular regions. Austenite could appear as small circles and long needle-like structures depending on the dendrite orientation. Figure 2.9 (b) shows that intercellular regions are enriched with nickel, titanium and molybdenum due to separation of solute elements in the liquid, so due to this enrichment, retained austenite is formed at that locations. Therefore, significant amount of austenite exists in the microstructure after additive manufacturing [6], [9], [12], [88], [101].

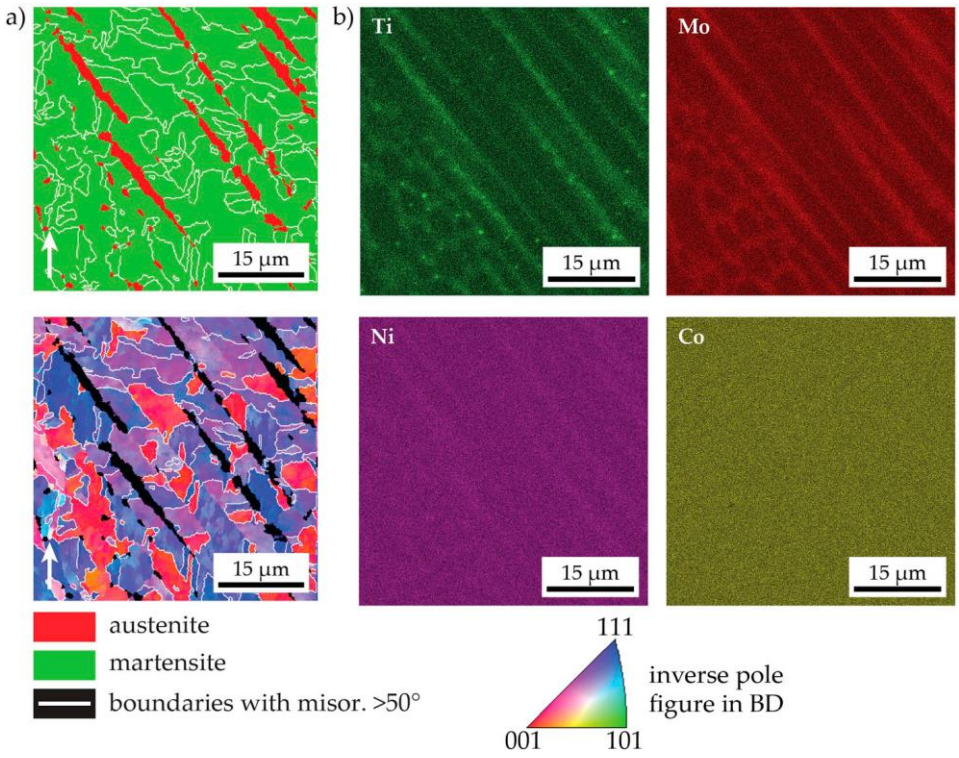

Figure 2.9. EBSD scan of the as-built 18Ni300 steel with EDS maps [102]

The study of Takata et al. [114] characterizes the microstructure and its associated crystallographic features of SLM fabricated maraging steels. They inferred the microstructural development during selective laser melting of maraging steels by considering the thermodynamic and crystallographic results, which is shown in Figure 2.10.

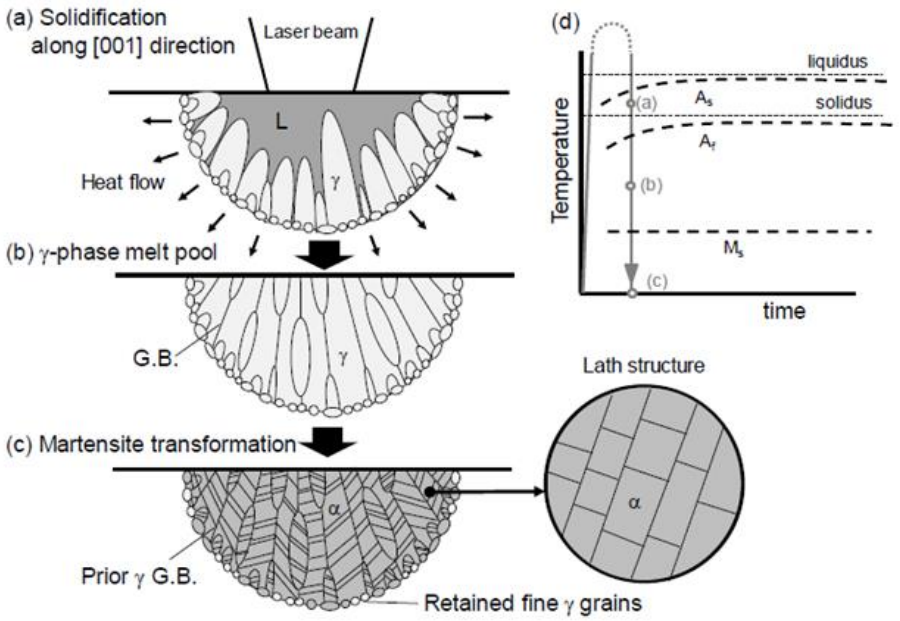

Figure 2.10. Schematics showing the formation of microstructure in the maraging steel during SLM [114]

During SLM, powder layers are locally heated up and melted with the laser irradiation, and melt pools are formed. Firstly, γ-phase which is the primary solid phase is observed to form at the interface between the solid and liquid phases, and during solidification, growth of austenite phase towards to the center of melt pools takes place as can be simulated in Figure 2.10 (a). Solidification of grains occurs in the <001> direction like other SLM produced FCC metals. This preferential solidification direction causes the formation of retained austenite with {001} texture. During the rapid cooling process, the melt pool can rapidly solidify to a number of {001} oriented grains, as can be seen in Figure 2.10 (b). Solidified melt pools are transformed into the lath martensite structure with a high density of dislocations at temperatures lower than M_s temperature with respect to the Kurdjumov–Sachs orientation relationship (Figure 2.10 (c)). This was determined as $(111)_\gamma // (011)_\alpha$ and $[-101]_\gamma // [-1-11]_\alpha$. Therefore, the reason of the formation of retained austenite at the melt pool boundaries instead of the inside of melt pools is observed due to the higher solidification rate in the liquid-solid interfaces of irradiated regions [114].

2.3.3 Heat Treatment of Additively Manufactured Maraging Steels

Maraging steels gain their superior combination of strength and toughness after aging heat treatment due to the hardening of martensitic structure with the precipitation of intermetallics. Generally, there is no precipitate in the microstructure in the as-built condition due to the high cooling rate which suppresses the precipitation [10], [88], [101], [106]. However, a small amount of precipitates can be seen in the DED produced materials because of the repeated reheating of the previous layer upon the deposition of the next layer, and this condition is called as intrinsic heat treatment.

Two types of heat treatment are usually applied to the maraging steels: aging and solution treatment. Aging treatment is applied at a temperature range 450 °C to 550 °C and the solution treatment temperature is between 800 °C to 900 °C for full austenization. After aging treatment, the dendritic martensitic structure is retained, and precipitation of intermetallic compounds takes place. This precipitation sequence upon aging is compared with conventional ones in the literature, and it is found that firstly, spherical Ni_3X where X could be Ti, Mo or Al precipitates (η-phase) is formed [2], [10], [88], [101], [106] followed by Fe_7Mo_6 (μ-phase) precipitates [88], [101], [106]. Also, austenite reversion and formation of reverted austenite can be seen due to aging at higher temperatures and longer times. Moreover, solution treatment is applied to the as-built maraging steel parts but dendritic structure completely disappear at that time and coarse fully martensitic microstructure is obtained and this leads to decrease in mechanical properties compared to the as-built condition [2], [6], [7], [9], [110].

2.3.4 Mechanical Properties of Additively Manufactured Maraging Steels

Maraging steels are high strength steels having an unusual combination of tensile strength and fracture toughness after aging treatment. Their strength in the wrought conditions is around 1000 MPa and increases up to 2000 MPa after aging treatment. However, the mechanical properties of additively manufactured MS300 steel are comparable to wrought maraging steels. They have a slightly higher yield and

ultimate tensile strength as compared to conventionally manufactured materials in the as-built conditions due to their fine microstructures [2], [9], [12], [110]. Again, their hardness (from 380 to 650 HV) and tensile strength (from 1200 to 2100 MPa) increases with aging treatment; however, ductility decreases as expected [2], [6], [7], [12]. Table 2.4 summarizes the mechanical properties of additively manufactured 18Ni300 maraging steel reported in the literature.

Upon aging treatment, austenite reversion at retained austenite cell boundaries can also take place [120,122,129,131]. However, this situation is not valid for conventionally produced materials, so their hardness in the aged conditions is higher than additively manufactured materials [130]. The toughness reduces significantly during aging, and also, there is a difference between AM produced and wrought materials. It is much lower for additively manufactured materials. To investigate the effect of solution treatment, some studies were also conducted. Casati et al. [6] argued that solution treatment is unnecessary for AM parts, and only direct aging is enough to obtain desired properties. However, Tan et al. [9] suggested the application of solution treatment to the as-built materials since fracture mechanisms are more favorable in the solution treated and aged materials than directly aged ones. Moreover, the effect of retained austenite and reverted austenite were also analyzed in the study of Casati et al. [6], and they found that they have a negligible amount of effect on the strengthening and fracture mechanisms. Austenite reversion plays a minor role in strengthening compared to the precipitation of intermetallics.

Finally, fatigue performance of additively manufactured maraging steels was investigated by Croccolo [115] and Becker [110]. Croccolo et al. concluded the fatigue properties to be isotropic with a fatigue limit of 600 MPa [115]. Becker et al. found that fatigue crack growth rates of peak aged material are isotropic and equal to that of conventionally-produced material [53]. Isotropy is due to the weak texture in the material as a consequence of the martensitic transformation. Despite virtually defect-free specimens, the ductility and fracture behavior is still strongly affected by the orientation, morphology, arrangement of defects in the material [6], [7].

Table 2.4 Summary of literature for mechanical properties of maraging steel; AB:As-built, ST:Solution Treated, and AT:Aging Treatment

Source	Condition	E(GPa)	YS (MPa)	UTS (MPa)	Elongation (%)	Hardness	Toughness (J)
[1], [9], [12], [110]	Wrought ST	180	760 – 895	830 – 1170	6 – 17	30 – 37	
	Wrought DA	183 – 191	1790 – 2070	1830 – 2100	5 – 11	54	
[2]	AB			1178	7.9	381 HV	24
	ST			1080	10.2	341 HV	24
	AT			2164	2.5	645 HV	5
[110]	AB	181	815 – 1080	1010 – 1205	8.3 – 12	420 HV	
	ST	161	800	950	13.5	320 HV	
	AT	220	1750	1850	5.1	600 HV	
[106]	AB					370 HV	
	AT					573 HV	
[116]	AB		1000	1200	8		
[7]	AB		900	1200	6		
	AT		1950	2000	1.5	630 HV	
[1]	AB			1085 – 1192	5 – 8	30 – 35 HRC	
[117]	AB	166	985	1152	7.6	34 HRC	
[6]	AB		915	1188	6.1	371 HV	
	AT		1917	2017	1.5	600 HV	
[12]	AB	163	1214	1290	13.3	40 HRC	42
	AT	189	1998	2217	1.6	58 HRC	5
[9]	AB		915	1165	12.4	35 – 36 HRC	
	ST		962	1025	14.4	28 – 29 HRC	
	AT		1967	2014	3.3	53 – 55 HRC	
	ST + AT		1882	1943	5.6	52 – 54 HRC	

CHAPTER 3

EXPERIMENTAL PROCEDURE

3.1 Material and Production of Specimens

The specimens produced from MS300 Maraging steel (European 1.2709 and German X3NiCoMoTi 18-9-5) were supplied from EOS GmbH, Germany. Totally, 27 rectangular specimens (10x10x8 mm) for microstructural analyses and 54 cylindrical specimens (8 mm ⌀ x 78 mm) for mechanical tests were produced via direct laser metal solidification (DMLS) which is also known as selective laser melting (SLM). The production layout of the specimens is shown in Figure 3.1. Stacking direction is from bottom to top of the table; i.e., the surface contacting the tray is the starting point, and the surface on which the specimen number is written is the finishing surface.

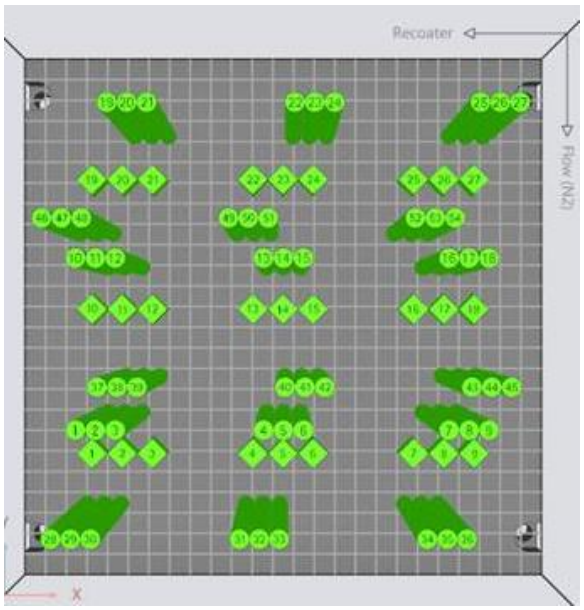

Figure 3.1. Orientation scheme of AM parts

The specimens were produced from the gas atomized powder of MS300 Maraging (Table 3.1 and Table 3.2) using a 59.5 J/mm^3 laser energy density. The production parameters and building direction were kept constant to minimize the effects of the parameters on the mechanical properties of the specimens. N_2(g) was used in order to prohibit the oxidation of alloying elements and also to ensure stable laser-material interaction without disturbance of process plume during production.

Table 3.1 Chemical composition of SLM manufactured specimens (wt %)

Ni	*Co*	*Mo*	*Ti*	*Al*	*Cr, Cu*	*C*	*Fe*
17-19%	8.5-9.5%	4.5-5.2%	0.6-0.8%	0.05-0.15%	<0.5%	<0.03%	Bal.

Table 3.2 Specification and size ranges of gas atomized maraging steel powder

Material	*Powder Size Range (*μm)	d_{50} (μm)
MS1	22 – 54	35

3.2 Measurement of Surface Roughness

The surface roughness (R_a) of the as-built specimen was measured by using the MarSurf PS10 roughness device in the horizontal and vertical cross-sections of the rectangular specimens by averaging five measurements on each surface.

3.3 DSC/TGA Analysis

Differential scanning calorimetry / thermogravimetric analysis was performed using TA Instruments SDT 650 Simultane DSC/TGA in an argon atmosphere with a heating rate of 20 °C/min between 200 °C to 1000 °C. Two specimen conditions, i.e., as-built and solution treated, were considered in the DSC/TGA analysis.

3.4 Heat Treatment

The specimens were subjected to solution treatment (ST) and aging treatment (AT). To obtain the desired microstructure and mechanical properties, a series of heat treatment processes were performed in the air atmosphere-controlled furnaces by changing temperature and time.

a) Solution treatments at three different temperatures (820 °C, 900 °C and 980 °C) for 1 hour were applied (the most suitable one was found as 900 °C). Then, the second heat treatment series was applied at 900 ° C for 15 minutes to 2 hours to find the optimum time. All solution treated specimens were cooled in air.

b) Aging was applied to both as-built and solution treated specimens. Firstly, to obtain optimum aging time, direct aging which refers to aging of as-built specimens was performed to the as-built specimens at 490 °C for times varying from 1 hour to 8 hours. All specimens were quenched in the air to room temperature. Aging at 490 °C for 6 hours was decided as the optimum process. Then, this aging procedure was applied to the solution treated specimens. All heat treatment processes are summarized in Table 3.3.

Table 3.3 Heat treatment procedures

Heat Treatment	*Temperature (°C)*	*Time (hr)*
Direct Aging *(Aging of as-built specimens)*	*490*	*1*
	490	*2*
	490	*4*
	490	*6*
	490	*8*
	420	*6*
	450	*6*
	490	*6*
	520	*6*
Solution Treatment	*820*	*1*
	900	*1*
	980	*1*
	900	*0.5*
	900	*2*
Solution Treatment & Aging	*820 / 490*	*1 / 6*
	980 / 490	*1 / 6*
	900 / 490	*1 / 6*
	900 / 490	*0.5 / 6*
	900 / 490	*2 / 6*
	900 / 450	*1 / 6*
	900 / 520	*1 / 6*
	900 / 590	*1 / 6*

3.5 X-Ray Diffraction

The existing phases in all specimens were determined by using the D8 Advanced Bruker X-Ray Diffractometer. Small pieces were prepared from the specimens after each heat treatment, and surfaces of each piece were ground to achieve smooth and contamination-free surfaces. The X-ray tube of the diffractometer has a Cu Kα (λ = 1.5406 Å) anode with Ni filters. The diffractometer operated at 40 kV and 30 mA, and data collected in the range between 30° and 90° at a scan rate of 2°/min.

Phase amount of all specimens were determined by one of the phase quantification methods, Rietveld method using Maud software to compare the change in austenite content with heat treatment procedures. Note that these results are not exact amount of austenite in the specimens. They are used only comparison since Co target must be used in the phase quantification of steels instead of Cu target.

3.6 Ultrasonic Wave Velocity Measurement

Longitudinal and transverse wave velocities along each direction were measured by using Olympus Epoch 600 to investigate anisotropic behavior of parts, and also to determine some mechanical properties non-destructively. The Time of Flight principle (ToF) was used to measure the distance between a sensor and a back-wall of the specimen. It is based on the time difference between the emissions of a signal which return to the sensor after being reflected by a back-wall. The sound velocities were calculated by dividing the covered distance to the ToF value. The time interval between the two echoes was measured in the microseconds scale. Honey was used as a couplant between the transducer and test piece surface to eliminate the acoustic impedance mismatch between air and solid. Smooth and flat surfaces were obtained by grinding. The thicknesses of specimens were measured with a micrometer with a ±0.001 mm error margin. During both longitudinal and transverse wave velocities measurements, Panametrics ultrasonic probes whose frequencies are 2.25 MHz were used. Time of flight values between four different echoes were measured, and the mean of these values was calculated.

3.7 Density Measurement

Densities of the as-built specimens were measured according to Archimedes' principle by using a laboratory balance density measurement kit. Firstly, the initial mass of specimens weighed in air, and then, they dipped into water to allow impregnation of open water pores. Then, the immersed mass of the specimen was measured. Density and relative density values were determined by using Equation

$$\text{Density of part} = \frac{\text{Initial mass}}{\text{Initial mass} - \text{Immersed mass}} * (\text{Density of liquid} - \text{Density of air}) + \text{Density of air}$$

Equation 3.1

$$\frac{\rho_{SLM}}{\rho_{standart}} = \frac{\rho_{water} * m_{SLM(air)}}{\rho_{standart} * (m_{SLM(air)} - m_{SLM(water)}}$$

Equation 3.2

3.8 Metallographic Examination

For metallographic examination, cubic shape specimens were cut into three pieces; each one belongs to one surface. Surface 1 is parallel to the building direction, and Surface 2 and Surface 3 are the perpendicular surfaces to building direction. Then, specimens were ground with SiC papers from 240 to 1200 grit size. Next, the surfaces were polished with diamond pastes whose diamond particle sizes are 3 and 1 μm, respectively.

Finally, polished specimens were etched with the Modified Dry's Reagent and 3% Nital and then rinsed with running water and ethanol. Subsequently, specimens were dried by air blowing.

Microstructural examinations were carried out with Huvitz HDS-5800 and FEI Nova NanoSEM 430.

3.9 Mechanical Tests

Micro- and macro-hardness measurements were conducted to both as-built and heat-treated specimens. All specimens were ground and polished to obtain flat surfaces. Hardness measurements were taken in Shimadzu HMV-2T hardness device with a diamond pyramid indenter by applying 19.612 N load for 10 seconds. On each specimen, at least six measurements were taken at specified intervals.

Tensile test specimens (Figure 3.2.) were prepared from cylindrical parts according to ASTM E8/E8M. Gauge length was chosen as 30 mm and BESMAK Testing Machine equipped with the Epsilon extensometer device with a constant loading rate of 0.48 mm/min was used.

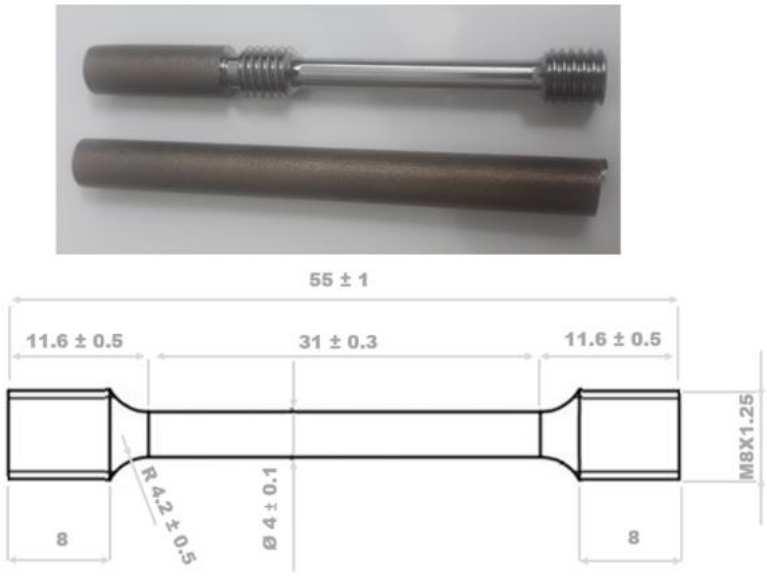

Figure 3.2. Tensile test specimen and dimensions

Besides, fracture surfaces of specimens were investigated by using FEI Nova NanoSEM 430.

CHAPTER 4

RESULTS AND DISCUSSION

In this part, the experimental findings related to structural analyses, microstructural evaluations, and mechanical property examinations are given in detail. Firstly, the as-built specimens were evaluated in terms of surface morphologies and part densities, microstructural and thermodynamic characteristics. Then, the effects of six different heat treatments on microstructure and mechanical properties of the specimens were discussed. Finally, microstructure and mechanical properties of the specimens were compared and correlated with the results of ultrasonic wave velocity measurements.

4.1 Characterization of as-built specimens

4.1.1 Relative Density and Surface Roughness

One of the critical points of selective laser melting is the fabrication of parts with high relative density. The average density and relative densities of the manufactured parts were found as 8.01 g/cm^3 and 99.2 %. They were calculated by the Archimedes principle, and these values compromise with the given data in the EOS Material data sheet [118].

Surface roughness gives information about the preparation level of the parts. While surface roughness values in the horizontal direction measured as 4.34 μm, it was 5.35 μm in the vertical direction. This shows that roughness varies according to building direction, and this is caused due to the short scan length, which leads to a high amount of heat flow in previously solidified layers [107]. This directional dependence has also been reported by Tan et al. [8], [9] and Bhardway et al. [107]. Tan et al. found that surface roughness values 4.16 μm in the horizontal direction and 4.79 μm in the vertical direction [8], [9].

Process parameters of selective laser melting strongly affect the surface roughness and relative density of parts. Re-melting of previously solidified layers results in a

change in surface roughness and pore formation. Souza et al. [103] concluded that increasing laser scan speed causes the narrowing of the scan track, and at higher speed, these tracks turn into discontinuity, which results in higher roughness. Also, they found that the effect of scan speed on roughness is higher than that of layer thickness.

4.1.2 Microstructural Characterization

Optical micrographs in the vertical (a, c) and horizontal (b, d) directions are shown in Figure 4.1. The motion track of the laser beam and laser scan angle is clearly seen in Figure 4.1 (a). The microstructure of top view consists of ellipsoidal structures, and their width is between 90 and 110 μm which is equal to the laser spot size (100 μm). In contrast to the top view, scan tracks of flaky half elliptical melt pools oriented parallel to building direction are observed on the lateral cross-section, and these scan tracks overlapped each other as can be seen in Figure 4.1 (b). The reason of the formation of semi-elliptical melt pools is due to the growth of scan tracks proportional to the thermal gradient, which is very high during selective laser melting. Moreover, there exist dark regions between melt pools, and this is the evidence of segregation of alloying elements in as-produced specimens. Also, the shape of the melt pools gives information about processes. The width of the semi ellipsoidal melt pools is between 90 – 110 μm, which is equal to laser beam diameter, and the height of semi-ellipsoids is approximately 40 – 50 μm, which is nearly same as the layer thickness.

The complicated thermal processes of selective laser melting lead to the formation of fine-grained cellular solidification structure and epitaxial growth across different track boundaries. This fine-grained martensitic structure is clearly seen in Figure 4.1 (c) and (d). The reason of this microstructural change can be explained by the high cooling rate (about 10^6 to 10^8 K/s) of the SLM process. At high cooling rates, solute atoms aggregate at the phase boundaries because of the insufficient time to form secondary dendrite arm and produce microscopic segregation. So, instead of lath martensitic structure, cellular morphology is formed [119].

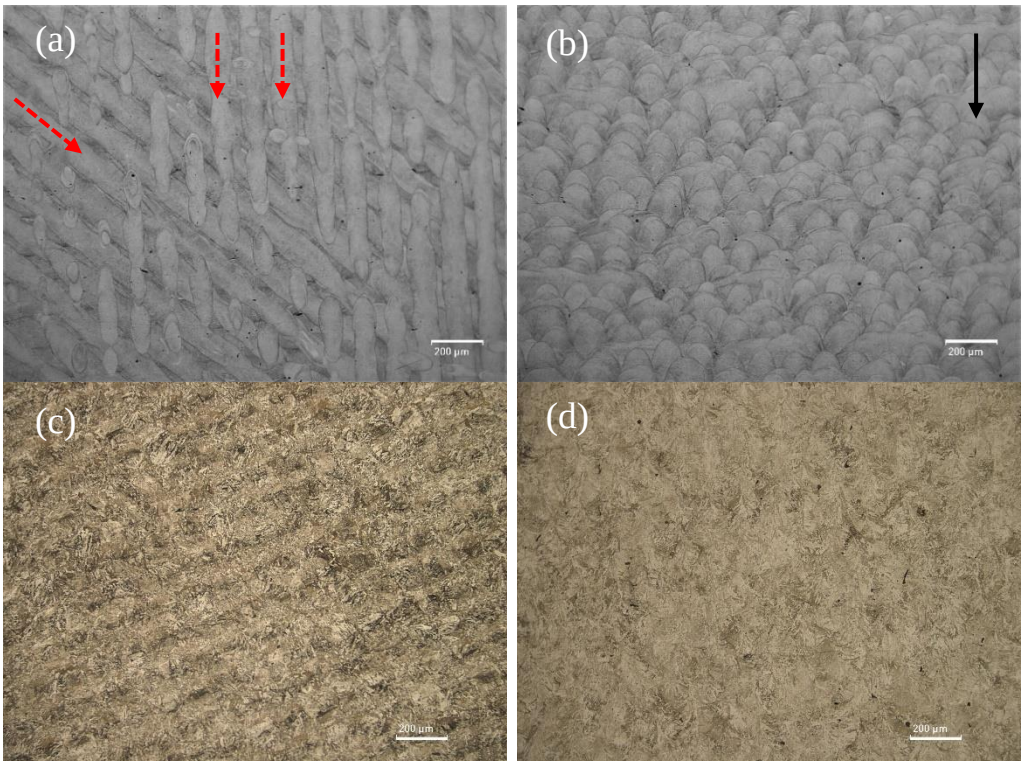

Figure 4.1. Optical micrographs of the as-built MS300 steel (a, c) top view (b, d) lateral view. Red dotted arrows show the laser scanning direction while the dark solid arrow indicates the building direction

Figure 4.1 shows that there is a difference between micrographs taken from the same locations depending upon the etchant type. Micrographs in the upper side were etched with Nital and the others etching with Modified Dry's Reagent. Nital etchant predominantly shows the details of the cellular microstructure and the motion of laser tracks; however, any signs of the typical martensitic structure were not revealed since Nital attacks alloy-rich segregations and clearly highlight the solidification substructure [2]. In contrast, martensite packets are more clearly seen in Figure 4.1 (c) and (d) since Modified Dry's reagent highlights the martensite packets more than laser tracks so, the selection of an appropriate etchant is essential to reveal desired microstructural features. Kučerová et al. are also highlight the effect of etchant on the microstructure of MS300 steels by using 3 % Nital, Adler's reagent, Fry's reagent, and dilute aqua regia [112].

The melt boundaries can be clearly seen (red cycle) in the SEM images of the as-built specimen (Figure 4.2). There are two different cellular morphologies on two sides of the melt boundary substantially columnar dendrites (blue circle) and fine equiaxed cellular structures (yellow circle). This type of structure is formed due to the rapid solidification of the SLM process, which prevents the formation of the lath martensite [12].

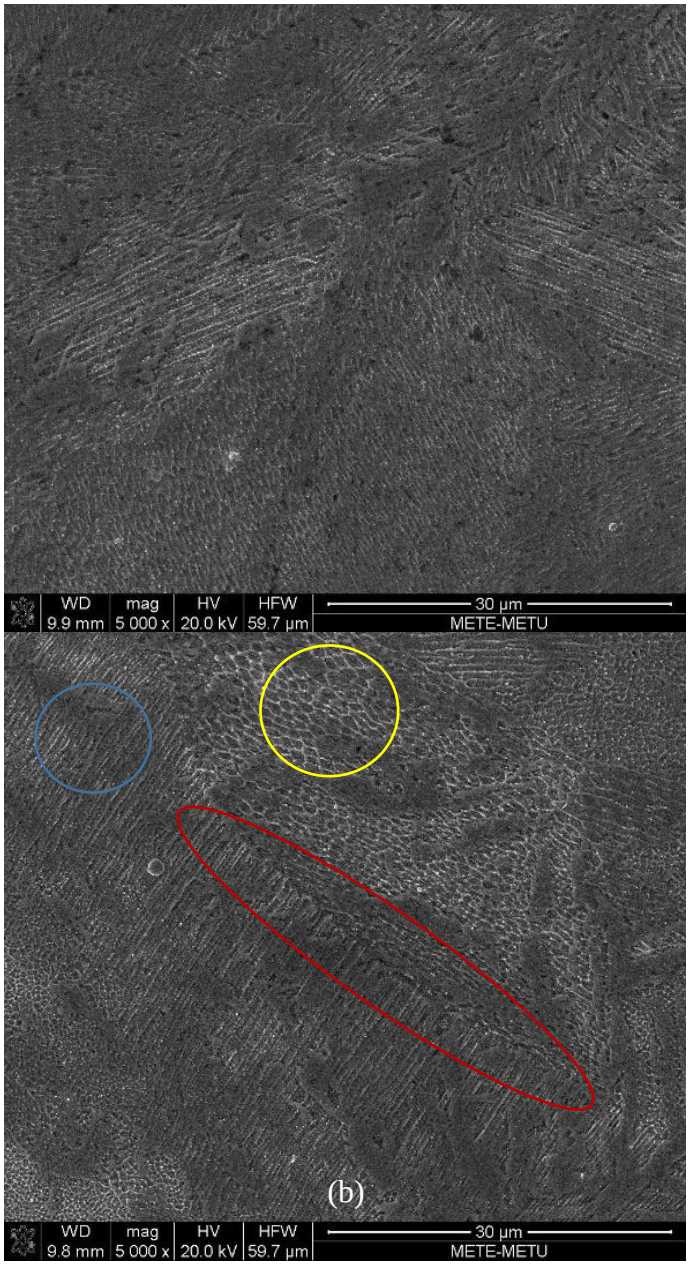

Figure 4.2. SEM images of MS 300 steel; (a) top view, (b) lateral view

4.1.3 Mechanical Characterization

Although maraging steels achieve their superior mechanical properties after aging treatment, it is important to compare mechanical properties of additively manufactured MS300 specimens with those at wrought condition since the microstructure of additively manufactured parts is very different than as-cast ones. The representative stress versus strain graph for the as-built MS300 maraging steel is given in Figure 4.3, and mechanical properties are listed in Table 4.1. The as-built specimen has 1112 MPa yield strength and 1203 MPa tensile strength. These results are very similar to those reported in the literature [7], [11], [12], [64], [110].

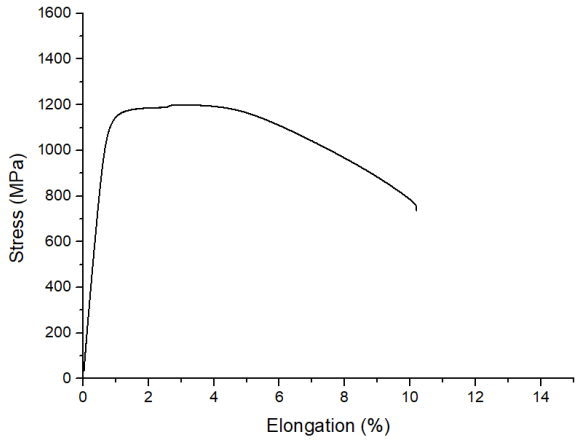

Figure 4.3. Representative stress vs. strain diagram for the MS300 specimen (as-built)

Mechanical properties for wrought maraging steel 300 are also summarized in Table 4.1 for comparison. Hardness and strength of SLM produced maraging steel 300 specimen are higher than those of the as-cast one. This difference can be explained due to microstructural changes. High cooling rates (10^6 – 10^8 K/min) and re-melting of the previous layer during manufacturing causes a formation of fine microstructure with tiny grains, and also micro segregation is obvious during SLM. Moreover, the ductility of SLM produced maraging steel is higher than the wrought specimen. The reason of this difference is natural aging, as explained by Shin et al.[120]. Furthermore, microstructural change is observed with changing building direction, and this causes a mechanical anisotropy. However, the hardness of SLMed MS300 specimens remains nearly the same regardless of direction, at around 380 HV. This

shows that microstructural anisotropy does not remarkably affect hardness values. This argument compromises with the results of Dohyung Kim et al. [100].

Table 4.1 Mechanical properties of SLM produced and wrought MS300 steel

Specimen Condition	Hardness Test						Tensile Test			
	Microhardness (HV2)			*Macro hardness (HV10)*			*E (GPa)*	*$R_{p0.2}$ (MPa)*	*R_m (MPa)*	*ε (%)*
	Face 1	*Face 2*	*Face 3*	*Face 1*	*Face 2*	*Face 3*				
As-built	380 ± 7	375 ± 8	376 ± 7	381 ± 2	376 ± 2	378 ± 3	173 ± 1	1112 ± 6	1203 ± 5	12.4 ± 1
Wrought[12]	332 – 342 HV (35 – 36 HRC)						180	760 – 895	1000 – 1170	6 – 15

4.1.4 Thermodynamic Characteristics

Phase transformations occurred in the as-built MS300 specimens were investigated via DSC analysis, which shows exothermic and endothermic behavior of materials during heating. DSC curve consists of two exothermic and three endothermic peaks (Figure 4.4).

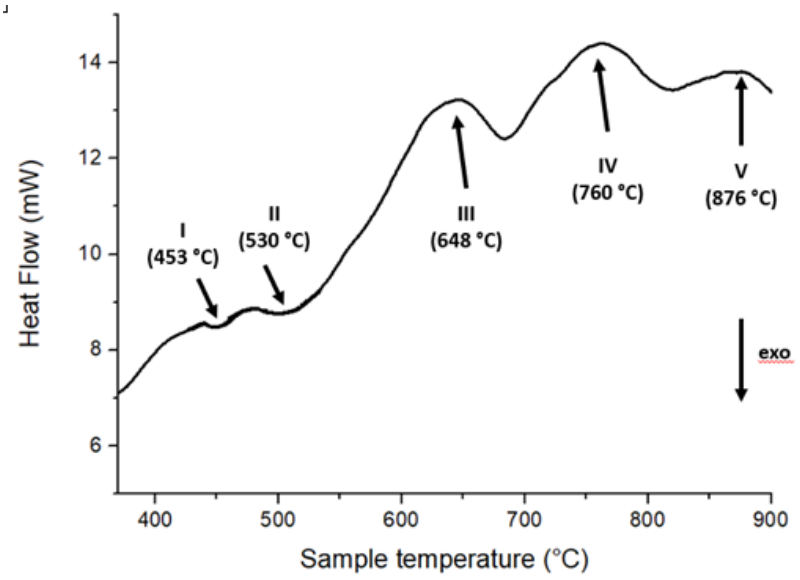

Figure 4.4. DSC curve for the as-built MS300 specimen

The first exothermic peak at 453 °C is attributed to carbide formation, coherent intermetallics precipitation, and martensite recovery [121], and the next exothermic peak corresponds to grain growth of retained austenite or formation of reverted austenite [121]–[123]. Also, over aging is observed in this temperature range. Tewari et al. [77] found that with the increasing temperature and holding time, ε, ω, Fe_2Mo and Ni_3(Ti, Mo) precipitates appeared in sequence from 400 °C to 550 °C. The endothermic peaks belong to solution treatment processes at higher temperatures. The third peak (648 °C) is related to the transformation of martensite to austenite and formation of reverted austenite, and the last peak is considered as recrystallization and decomposition of precipitates [121], [123], [124]. Finally, an extra peak that occurs at nearly 900 °C (peak # V) may be related to impurities like oxides [11].

Therefore, the aging range is found as 450 °C to 550 °C and solutionizing temperature range is 600 °C to 800 °C. Aging treatment temperature range was determined as 450 °C to 590 °C, and the solution treatment temperature range chosen as 820 °C to 980 °C in this study. The reason of choosing a solutionizing temperature higher than temperature range found from the DSC curve is the micro segregation observed in the selective laser melted parts that can be annihilated by diffusion of elements at high temperatures [11].

4.2 Optimization of Heat Treatment

4.2.1 Structural Analysis

XRD patterns of heat-treated specimens are shown in Figure 4.5 (a) to (f). These peaks belong to BCC and FCC crystal structures. As can be mentioned before, a soft lath-like (BCC) martensite (α-phase) is formed in maraging steels due to their low carbon content. The as-built specimen consists of martensite (α-phase, BCC) and a small amount of austenite (γ-phase, FCC) phases. (200)γ of the austenite (γ) phase gives a small peak at nearly $2\theta = 51°$. The formation of a small amount austenite phase is due to the non-uniform distribution of alloying elements at cell boundaries. Retained austenite formation is promoted during cooling due to the non-homogenous distribution of alloying elements, in agreement with some studies [3], [6], [11], [12].

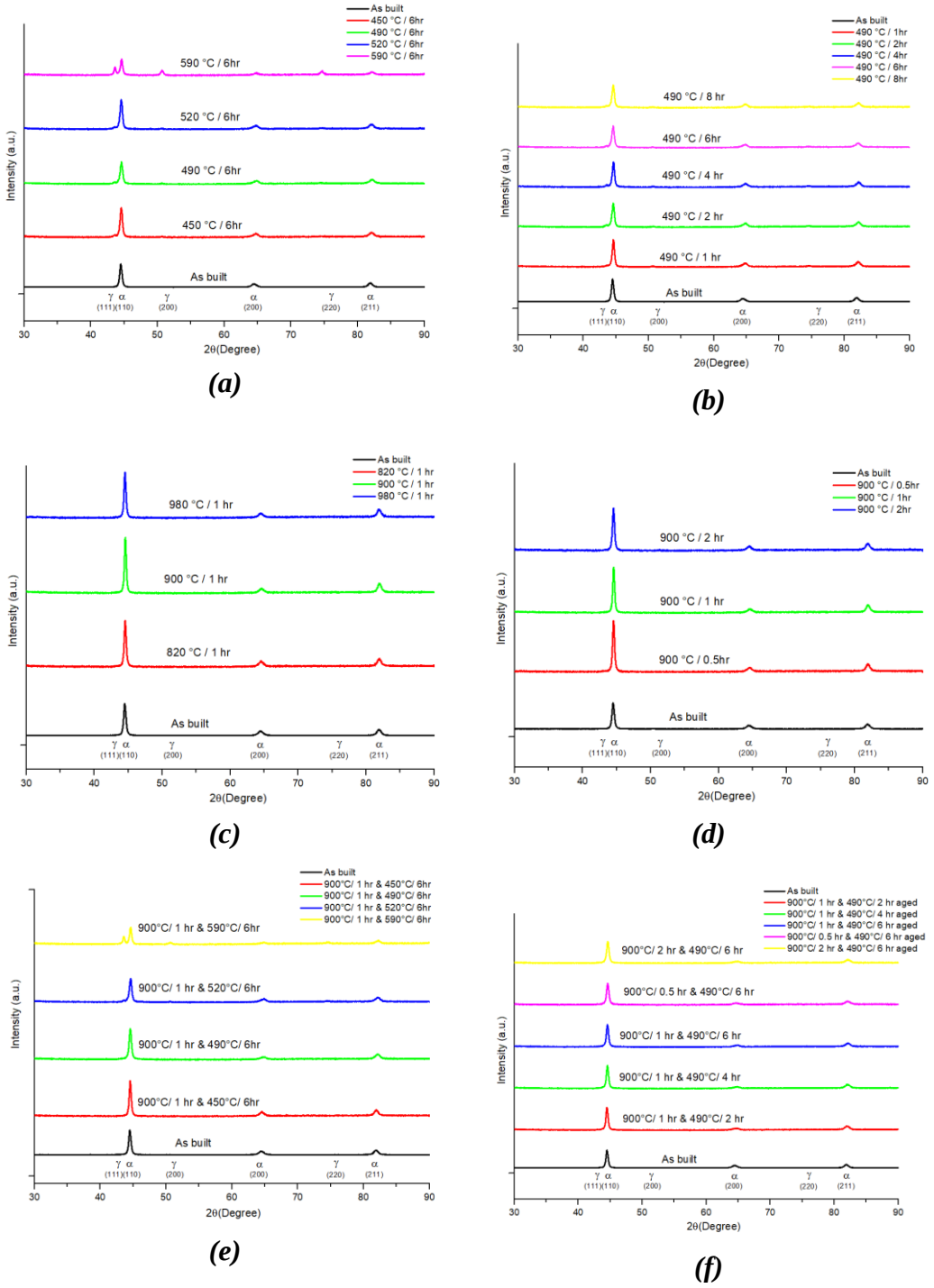

Figure 4.5.XRD patterns of heat-treated MS300 specimens: (a) Aging at different temperatures; (b) Aging at different holding time; (c) Solution treatment at different temperatures; (d) Solution treatment at different holding time; (e) Solution treatment and aging at different temperatures; (f) Solution treatment and aging at different holding time

Figure 4.5 (a) and (b) shows the XRD patterns of the specimens aged at different temperatures and times. The most obvious change is seen after aging 590 °C for 6 hours. In this condition, the intensity of (200)γ peak increases, and (111)γ and (220)γ peaks appear. This shows that phase transformation from martensite (BCC) to austenite (FCC) occurs during aging at temperatures higher than 520 °C. Also, it is evident that austenite growth happens in the (111) and (220) directions rather than (200) direction. There is no distinct feature seen with increasing holding time. Only the intensity of (200)γ peak increases which indicates that the austenite phase promotes in the (200) direction with longer aging time.

Furthermore, when solution treatment is applied to the as-built specimen, the (200)γ peak completely disappears, the intensity of (200)α decreases and the intensity of (211)α increases with the increasing temperature and time, as shown in Figure 4.5 (c) and (d). This indicates that during solution treatment, the austenite phase in the as-built specimens is wholly transformed into martensite with preferential growth direction of (211). Due to the micro segregation of alloying elements at cellular boundaries, retained austenite exists at melt pool boundaries in the as-built specimens [101]. However, these elements dissolve in the austenite matrix homogeneously after solution treatment, so austenite completely transforms to the martensite in subsequent cooling.

Finally, the aging behavior of the solution treated specimens was investigated. Corresponding XRD patterns are shown in Figure 4.5 (e) and (f). Until 520 °C, they are very similar to solution treated ones; all peaks belong to α-phase, and there is no evidence for γ-phase. This shows that during the aging of solution treated specimens till 490 °C, the transformation from martensite to austenite is not seen due to the homogenous distribution of alloying elements. However, peaks belong to austenite phase start to seen in the solution treated specimens after aging at temperatures higher than 520 °C as in as-built conditions due to austenite reversion.

The peaks corresponding to intermetallic precipitates such as Ni_3Al, Ni_3Ti, Ni_3Fe, or Ni_3Mo are not seen clearly in the aged specimens. They are located at the range of 20° to 40°, but the characterization of these peaks is very difficult from the XRD pattern due to their extremely small intensities [100].

Moreover, the phase contents of the as-built and heat-treated specimens were calculated from the XRD patterns to analyze the change in the austenite content and summarized in Table 4.2. Note that this analysis was made for only comparison. To find the exact amount of austenite in the matrix, Co target must be used instead of Cu target. The as-built specimen contains 97.22 % α and 2.78 % γ phases. The amount of austenite decreases with solution treatment: it decreases 0.32 % after holding at 900 °C for 30 minutes and completely disappear after 1 hour. Although austenite fraction increases with aging in the as-built specimens, no austenite is observed in the solution treated ones. The reason for this difference can be explained by the segregation that occurred during selective laser melting, and this nonhomogeneous structure disappears after solution treatment. % Austenite vs. aging temperature and % austenite vs. aging time graphs (Figure 4.6) shows the effect of aging on the austenite content of the as-built specimens more clearly.

Figure 4.6 (a) shows a variation of the austenite content as a function of the aging temperature. Initially, 2.78 % γ exists in the as-built specimen, and after aging 6 hr, the austenite content increases to 7.49 %. The austenite content increases gradually with the increasing aging temperature indicating that austenite transformation is promoted by aging temperature. Austenite fraction increases sharply to 44.31 % at 590 °C due to the rapid growth of the austenite phase at high temperatures. Figure 4.6 (b) shows the variation of austenite fraction at 490 °C as a function of time. It can be seen that γ content increases with increasing holding time. 8.53 % γ is obtained after 8 hr, and this shows that austenite formation and growth rate is relatively stable for changes in the aging time compared to the aging temperature.

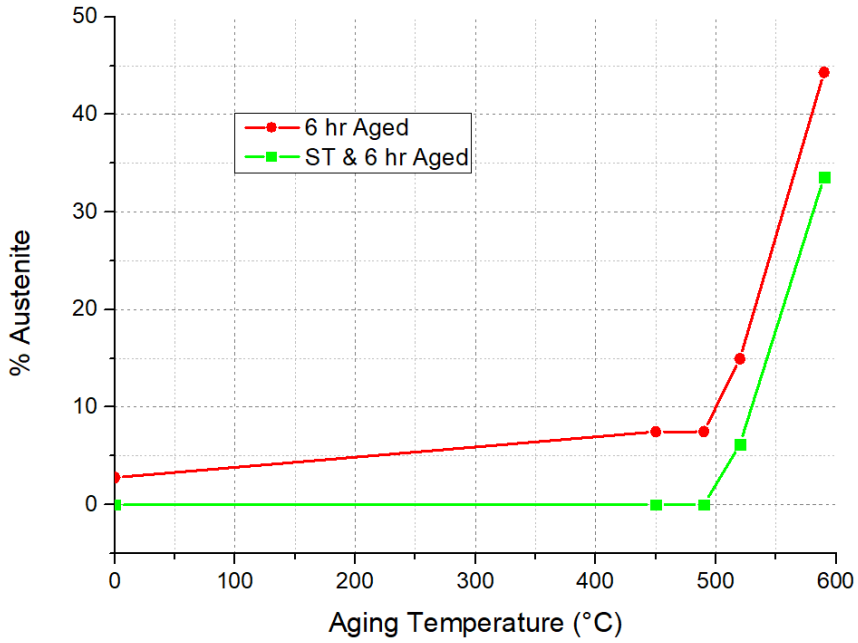

(a)

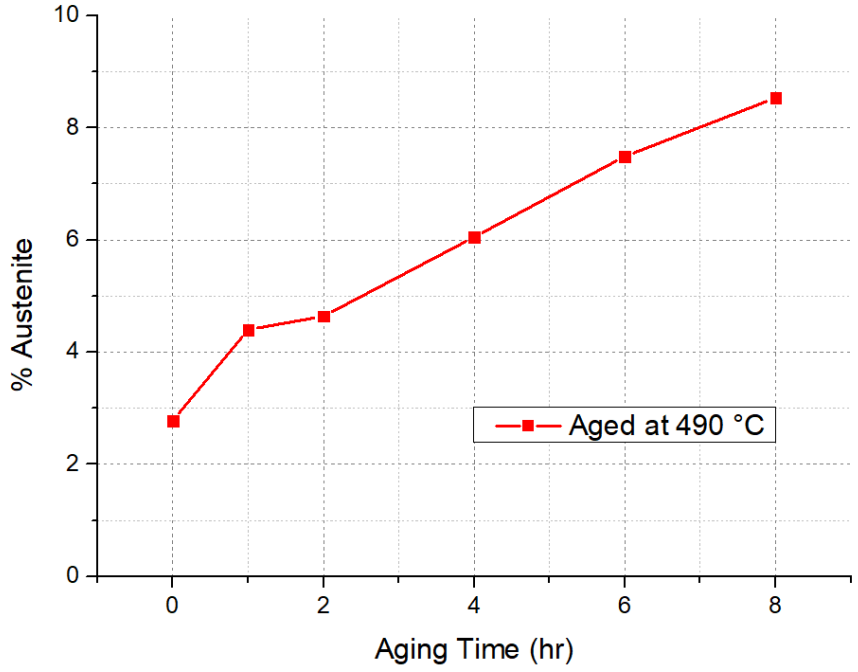

(b)

Figure 4.6. Austenite content of the aged specimens: (a) as a function of temperature for 6 hr aging; (b) as a function of time at 490 °C

Table 4.2 The % volume of martensite (α) and austenite (γ) in the as-built and heat-treated MS300 specimens

Variable	*Temperature / Time*	*α-phase (vol %)*	*γ-phase (vol %)*
	As-built	97.22	2.78
Aging Temperature	450 °C / 6 hr	92.53	7.45
	490 °C / 6 hr	92.51	7.49
	520 °C / 6 hr	85.05	14.95
	590 °C / 6 hr	55.69	44.31
Aging Time	490 °C / 1 hr	95.60	4.40
	490 °C / 2 hr	95.36	4.64
	490 °C / 4 hr	94.95	5.05
	490 °C / 6 hr	92.51	7.49
	490 °C / 8 hr	91.47	8.53
Solution Treatment Temperature	820 °C / 1 hr	100	0
	900 °C / 1 hr	100	0
	980 °C / 1 hr	100	0
Solution Treatment Time	900 °C / 0.5 hr	99.68	0.32
	900 °C / 1 hr	100	0
	900 °C / 2 hr	100	0
Solution Treatment / Aging	900 °C / 0.5 hr & 490 °C / 6 hr	100	0
	900 °C / 2 hr & 490 °C / 6 hr	100	0
	900 °C / 1 hr & 490 °C / 2 hr	100	0
	900 °C / 1 hr & 490 °C / 4 hr	100	0
	900 °C / 1 hr & 490 °C / 6 hr	100	0
	900 °C / 1 hr & 450 °C / 6 hr	100	0
	900 °C / 1 hr & 520 °C / 6 hr	93.82	6.18
	900 °C / 1 hr & 590 °C / 6 hr	66.41	33.59

4.2.2 Microstructural Evaluation

The microstructure of the solution treated specimen is presented in Figure 4.7. Solidification traces and scan tracks in the as-built specimen are completely disappeared after solution treatment. This leads to the elimination of microstructural anisotropy of the top and lateral surfaces of the as-built specimen. The structure of the top surface (Figure 4.7 (a)) is very similar to that of the lateral view (Figure 4.7 (b)). Due to the grain growth of austenite during solution treatment, instead of cellular structure, both of them have a coarse lath martensitic structure. This structure is characterized as massive martensite blocks or packets, consisting of fine bundles of parallel and heavily dislocated laths [6].

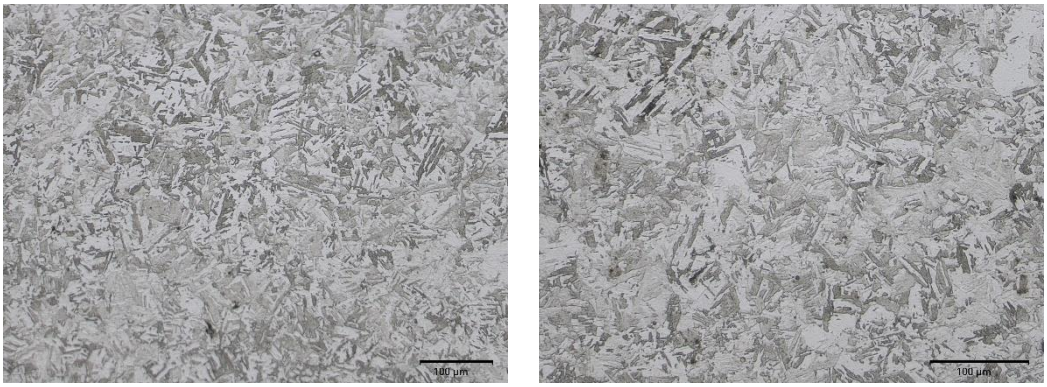

(a) **(b)**

Figure 4.7. Representative micrographs of the solution treated specimens; (a) top view, (b) lateral view

Figure 4.8 shows the microstructure of aged specimens at 490°C for holding time from 1 hr to 8 hr. These results are distinct from solution treated ones. The cellular microstructure of the as-built specimen does not completely disappear, but it starts to become blurred with increasing time, as can be seen clearly in Figure 4.8. Aging causes nucleation and growth of austenite at cell boundaries where it is already present, even though in a lower amount due to the nickel enrichment at cell boundaries that reduce the austenite transformation temperature [125] and the presence of austenite at cell boundaries which promotes the heterogenous nucleation [88].

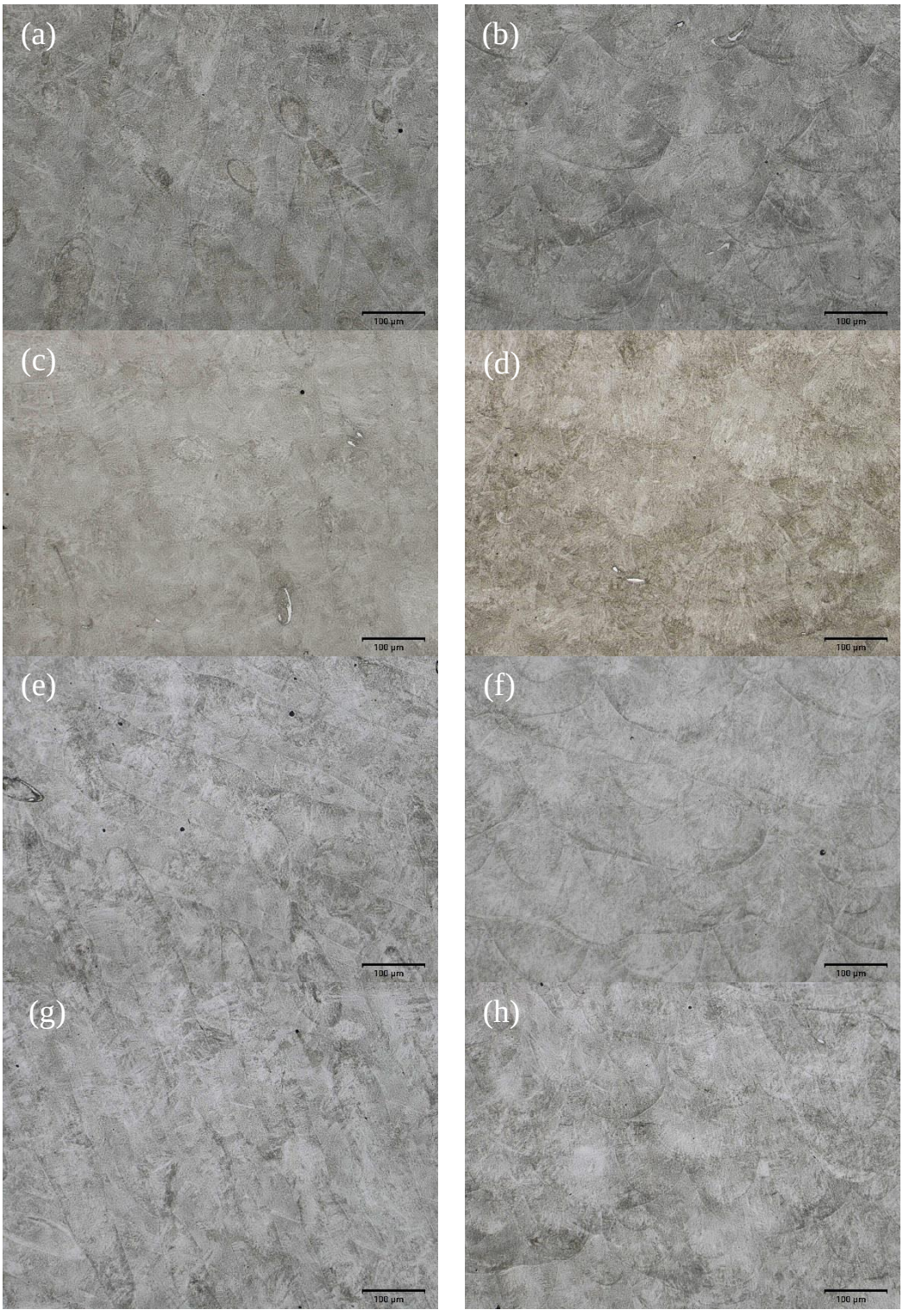

Figure 4.8. Representative micrographs of the aged specimens; (a,c,e,g) top view, (b,d,f,h) lateral view; Aging at 490 ℃ for (a,b) 1 hr; (c,d) 4 hr; (e,f) 6 hr; (g,h) 8 hr

Figure 4.9 displays the microstructure of specimens that are firstly solution treated at 900 °C for 1 hour and then aged at 490 °C for 4 hr (Figure 4.9 (a) and (b)) and 6 hr (Figure 4.9 (c) and (d)). Micrographs on the left side belong to the top view, and the ones on the right side are lateral surfaces. These structures are entirely different than the direct aged ones. There is no sign of cellular structure, and massive martensitic blocks are clearly seen. Also, the anisotropic appearance of SLM is eliminated, and the nearly same structure is obtained in both top and lateral surfaces.

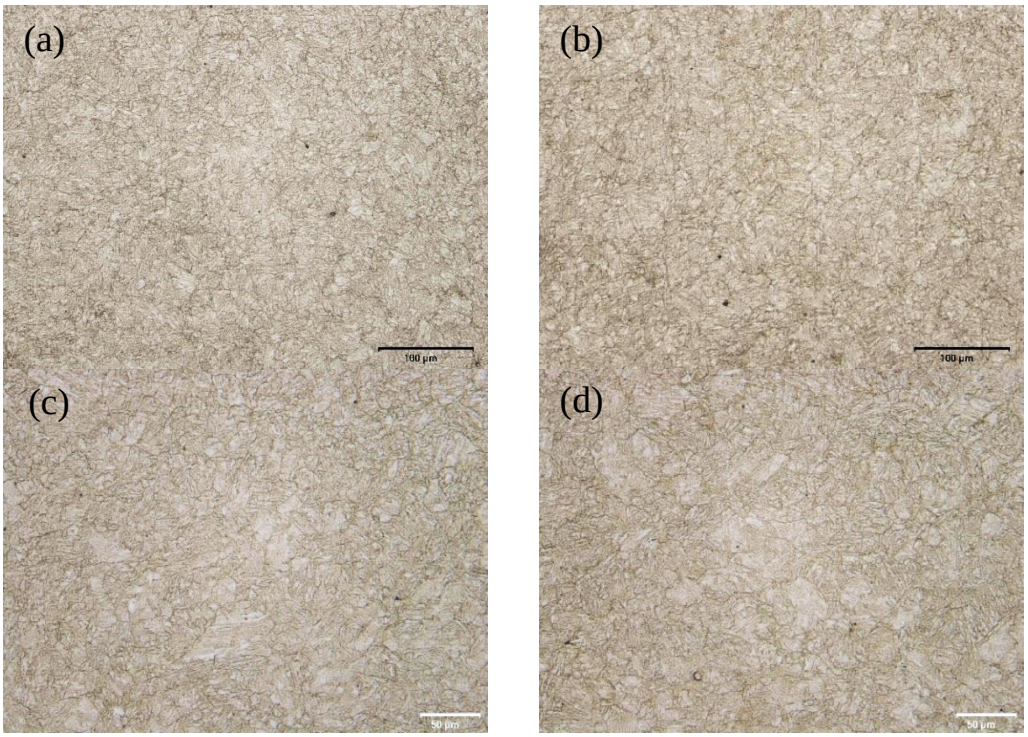

Figure 4.9. Representative micrographs of the specimens that were solution treated & aged at 490 °C (a,b) for 4 hr, (c,d) for 6 hr; (a,c) top view, (b,d) lateral view

Figure 4.10 presents the microstructures of specimens that were aged at different aging temperatures. Although cellular structure does not completely disappear by aging at low temperatures, the disparate microstructure is observed at high aging temperatures. As can be seen in Figure 4.10 (c), aging at 590 °C causes the overaging, and instead of fully martensitic structure, a martensitic – austenitic structure appears due to the further austenite reversion. γ-Fe is extensively present at cell boundaries of aged specimens; however, it also appears within the cells in the overaged specimens. An extreme case is depicted in Figure 4.10 (c). Austenite reversion

occurs to such an extent that the previous microstructure is barely visible. These results are consistent with the literature, i.e., it has been demonstrated that γ-Fe starts to grow at lath martensite and, as aging proceeds, it nucleates within the martensite laths [75], [125].

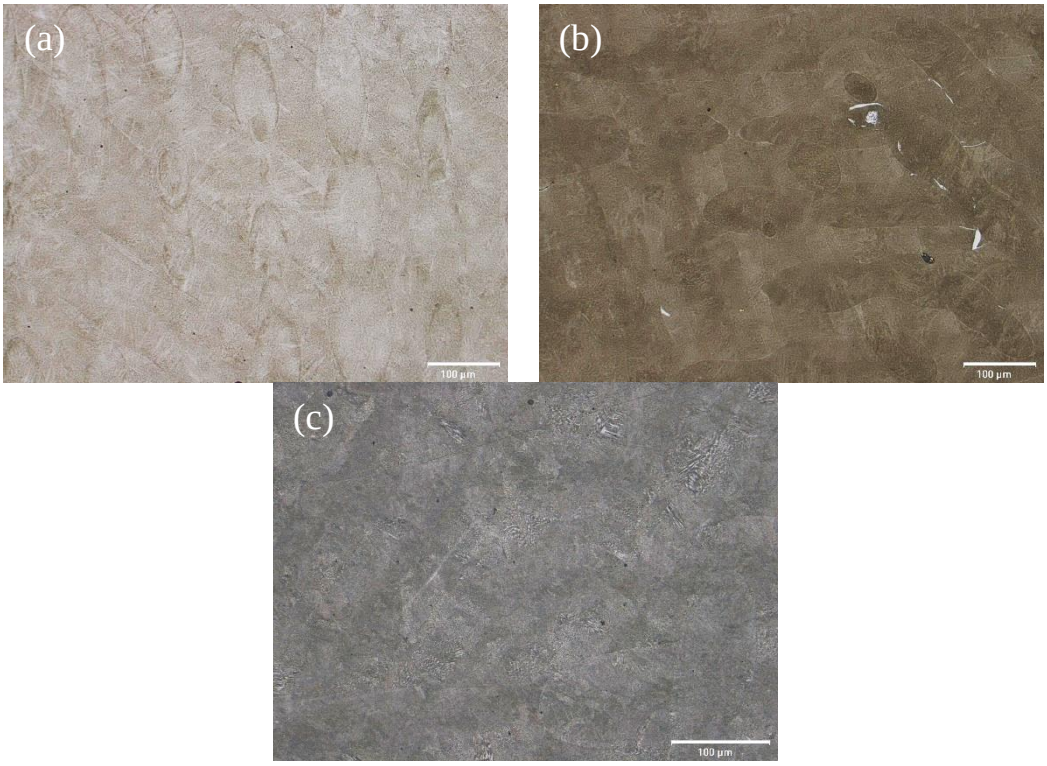

Figure 4.10. Representative micrographs of the aged specimens (top surface); (a) Aged at 450 ℃ for 6 hr, (b) Aged at 520 ℃ for 6 hr, (c) Aged at 590 ℃ for 6 hr

The SEM micrographs of the specimens under different heat treatment conditions are presented in Figure 4.11. After solution treatment, the boundaries, strips and cells disappear gradually. The microstructure shows intertwined large slats (white arrows in Figure 4.11 (a)). This is because that the high temperature during solution treatment causes the growth of austenite grain, which leads to bigger martensite laths. Figure 4.11 (b) presents a micrograph of solution treated & aged specimen. It can be seen that the martensite laths become longer and wider. However, the boundary is still faintly visible. Figure 4.11 (c) and (d) present the microstructure of directly aged specimens. The results are distinct from those obtained by solution treated ones. The strips (blue arrow), melt boundary (red circle) and cellular structures (orange

circle) do not completely disappear but become blurred with the temperature and holding time rising.

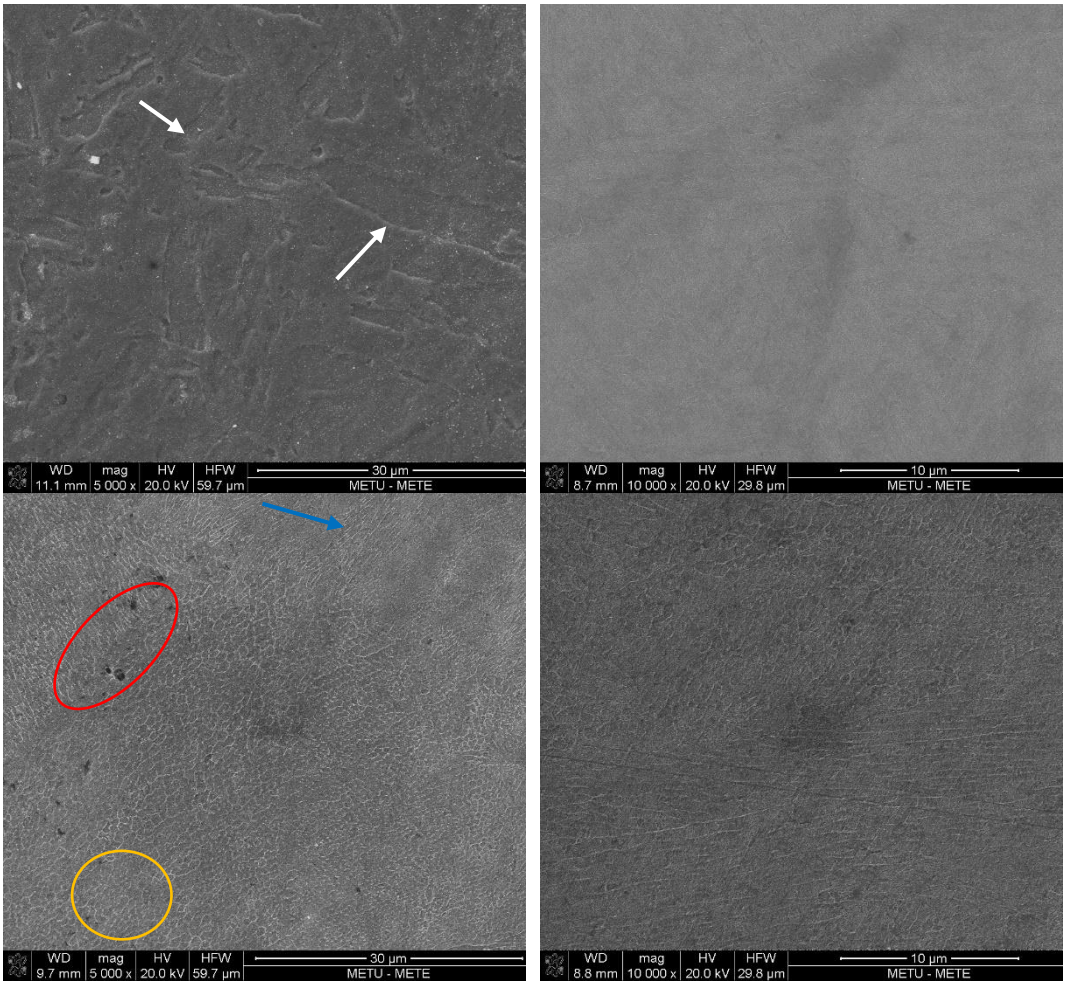

Figure 4.11. SEM images of heat-treated specimens; (a) Solution treated at 900 ℃ for 1 hr, (b) Solution treated and aged at 490 ℃ for 6 hr, (c) Aged at 490 ℃ for 4 hr, and (d) Aged at 490 ℃ for 6 hr

4.2.3 Mechanical Test Results

4.2.3.1 Tensile Test Results

Figure 4.12 shows the stress vs. strain graphs of the specimens after different heat treatments in order to emphasize the differences in the room temperature tensile behavior of MS300 maraging steels.

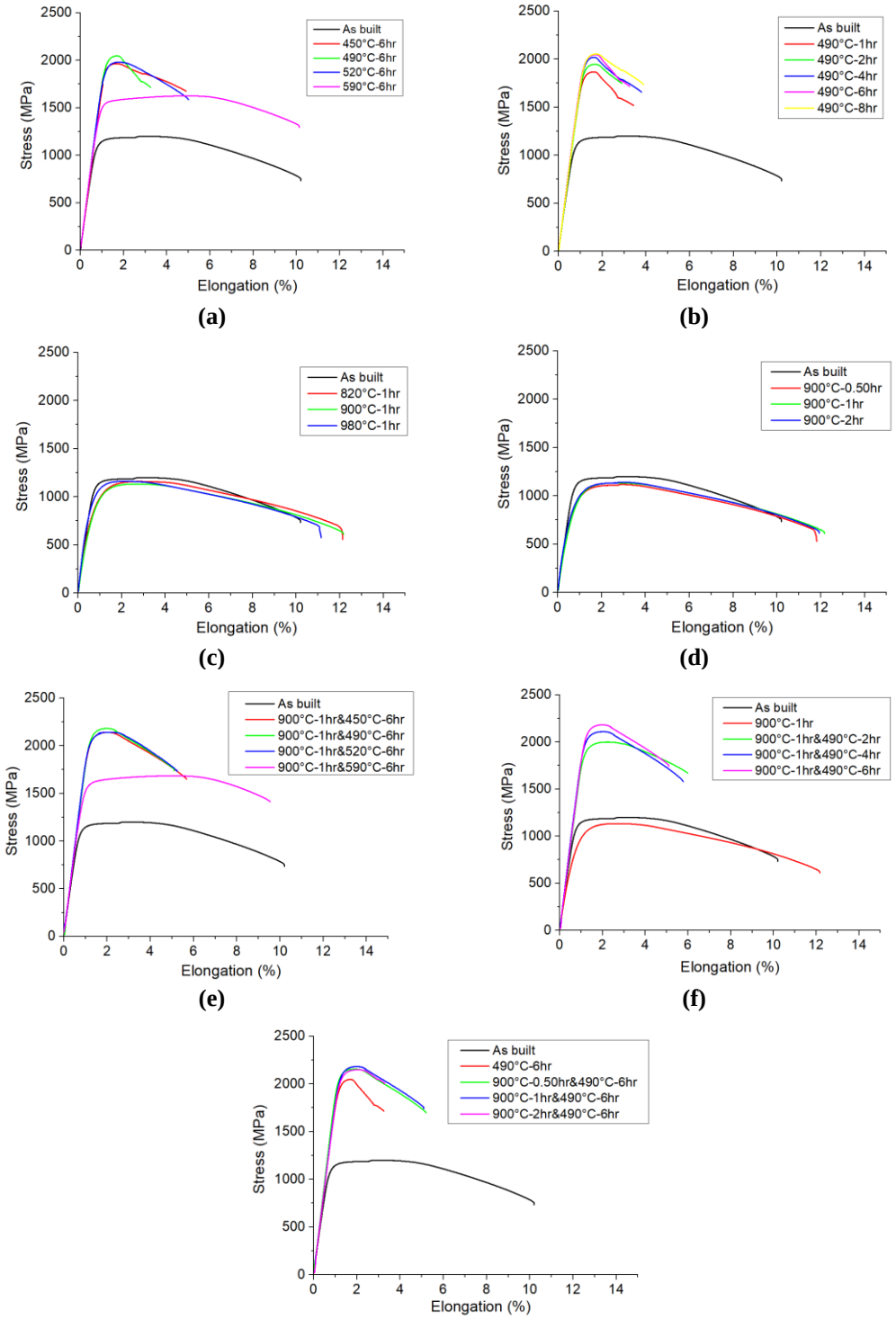

Figure 4.12. Stress vs. strain graphs of the heat-treated specimens; (a) Aging at different temperatures; (b) Aging at different times; (c) Solution treatment at different temperatures; (d) Solution treatment at a different time; (e) Solution treatment and aging at a various temperatures; (f) Solution treatment and aging at a different times; (g) Solution treatment at a different time and aging at 490 °C

For the aged specimens, as can be seen in Figure 4.12 (a) and (b), the tensile strength appears to increase with the increasing aging temperature and time. Strength increases up to 2050 MPa after aging 490 °C due to precipitation of intermetallics, as in agreement with the study of Tan et al. [9], [10]. However, tensile strength starts to decrease at a higher aging temperature. As compared to the holding time, the aging temperature shows a significant influence. This is caused by the comprehensive effect of austenite and precipitated particles. Although tensile strength is enhanced with the precipitation of intermetallic compounds, the increase of austenite content reduces the tensile strength. Moreover, the tensile strength will decrease if the size of particles becomes larger, and the big particles also cause the elongation reduction. This situation is more clearly seen in the specimen aged at 590 °C. Although tensile strength increases from 1203 to 2041 MPa after 6 hours aging at 490 °C, it reduces to 1276 MPa at 590 °C. This reduction is caused mainly due to an increase in austenite content after aging at this temperature. As can be mentioned in Section 4.2.1 (Figure 4.6), austenite phase amount reaches 4.31 % after 6-hour aging at 590 °C, and this sharp increase is responsible for the reduction of the tensile strength.

Comparing with the as-built specimen, the tensile strengths decrease slightly under ST (Fig. 4.12 (c) & (d)). Initially, the as-built specimens have fine-grained martensite due to the rapid solidification of melt pool at high cooling rates. Moreover, the as-built specimens have larger residual stresses, so that movement of dislocations is prevented, and crack formation and propagation hindered [126]. As such, the tensile strength of MS300 steels is improved. However, solution treatment causes a change in microstructure. Fine-grained dendritic structure transforms into lath martensite after solution treatment, and more martensitic transformation occurs at higher temperatures and holding times. Although martensitic structure improves the mechanical properties, a reduction is observed in this case due to the elimination of fine structure and residual stresses after solution treatment. Thus, it can be concluded that the improvement of mechanical properties from martensite transformation is lower than the deduction due to the disappearance of the fine grains and residual stresses so that tensile strength decrease eventually, as can be seen in Table 4.3.

However, the tensile strengths increase sharply after the aging of solution treated specimens, as shown in Figure 4.12 (e) to Figure 4.12 (g). Again, tensile strength increases due to the precipitation intermetallic compounds such as Ni_3Mo, Ni_3Ti, Ni_3Al, and Fe_2Mo. However, tensile strength of firstly solution treated and then 490 °C aged specimens have slightly higher tensile strength than directly aged specimens. The reason for this improvement could be the elimination of the austenite phase after solution treatment. The tensile strength is enhanced by the elimination of existing austenite phase with solution treatment and also by preventing the formation and growth of new austenite phase during aging at a suitable temperature. In this way, the tensile strength of MS300 steels reaches up to approximately 2200 MPa. These results show that heat treatment affects the tensile property of MS300 steel differently. There is a difference between the mechanical properties of the specimens that were directly aged and aged after solution treatment, so that solution treatment is needed to be reached the highest tensile strength. The optimum aging treatment was found as 490 °C for 6 hours.

Besides, there exists a remarkable change in ductility after aging treatment. Reduction of ductility is caused due to the strengthening of the matrix by intermetallic compounds, and this is one of the features of aged maraging steels. Directly aged specimens have nearly the same elongation that shows that the effect of austenite is a negligible amount. Moreover, it is found that the fracture elongation of SLM produced maraging steels is quite lower than that of conventionally manufactured both in the as-built and aged conditions. This could be explained by the presence of typical SLM defects, such as porosity and melting faults in the brittle matrix. These porosities and unmolten particles are seen in the fracture surfaces, and their contribution to failure is higher than the effect of austenite. To conclude, the effect of aging treatment on mechanical properties is critical. Both hardening and softening mechanisms could be considered together since the combination of the intermetallic precipitation adjusts the final mechanical properties, the austenite reversion, coarsening and embrittlement of phases and intermetallics.

Table 4.3 Tensile test results of the as-built and heat-treated specimens with standard deviations

	YS (MPa)	*UTS (MPa)*	*Elongation (%)*	*E (GPa)*
As-built	1112 ± 6	1203 ± 5	11.42 ± 1.7	173 ± 1
450 °C / 6 hr	1938 ± 23	1964 ± 28	4.31 ± 0.8	174 ± 2
490 °C / 6 hr	2014 ± 28	2041 ± 33	3.27 ± 0.2	182 ± 1
520 °C / 6 hr	1919 ± 21	1980 ± 19	4.47 ± 0.8	181 ± 1
590 °C / 6 hr	1087 ± 18	1276 ± 16	14.27 ± 1.9	175 ± 4
490 °C / 1 hr	1819 ± 12	1855 ± 17	5.25 ± 0.3	173 ± 1
490 °C / 2 hr	1904 ± 6	1949 ± 4	4.36 ± 0.4	174 ± 3
490 °C / 4 hr	1963 ± 16	2012 ± 11	4.15 ± 0.5	175 ± 1
490 °C / 8 hr	2001 ± 11	2052 ± 1	3.89 ± 0	180 ± 3
820 °C / 1 hr	933 ± 15	1170 ± 20	12.63 ± 0.2	166 ± 4
900 °C / 1 hr	921 ± 10	1124 ± 12	12.59 ± 0.3	164 ± 1
980 °C / 1 hr	987 ± 8	1169 ± 10	13.42 ± 1.5	170 ± 1
900 °C / 0.5 hr	908 ± 5	1116 ± 16	9.88 ± 0.4	167 ± 2
900 °C / 2 hr	916 ± 4	1130 ± 17	10.84 ± 2.2	166 ± 2
900° C / 0.5 hr & 490 °C / 6 hr	2100 ± 9	2155 ± 8	4.89 ± 0	184 ± 3
900°C / 1 hr & 490 °C / 6 hr	2115 ± 15	2181 ± 12	4.02 ± 1.6	185 ± 2
900°C / 2 hr & 490 °C / 6 hr	2081 ± 7	2148 ± 7	3.76 ± 0.1	179 ± 1
900°C / 1 hr & 490 °C / 2 hr	1915 ± 9	1999 ± 10	6.52 ± 1	175 ± 1
900°C / 1 hr & 490 °C / 4 hr	2026 ± 12	2109 ± 11	6.12 ± 0.1	180 ± 2
900°C / 1 hr & 450 °C / 6 hr	2070 ± 11	2140 ± 8	5.68 ± 0.4	182 ± 1
900°C / 1 hr & 520 °C / 6 hr	2059 ± 13	2141 ± 15	5.25 ± 0.2	184 ± 2
900°C / 1 hr & 590 °C / 6 hr	1556 ± 17	1685 ± 14	10.13 ± 0.8	177 ±2

Elastic properties of MS300 specimens are also critical for two principal reasons which are relation with interatomic forces and essential for design parameters. Due to the direct connection between elastic constants and interatomic forces, Young's modulus of materials is connected with various solid-state phenomena. Lattice specific heats, strengths and phase stabilities are some examples of this phenomena. Moreover, elastic constants are used to determine deflection under static and/or thermal stresses so that they must be known. As shown in Table 4.3, the Young's moduli of the MS300 specimens in as-built conditions is nearly 173 GPa which is about 20 % lower than those of unalloyed iron (215 GPa). Generally, Pure metals have higher elastic properties than their alloys. Nickel, Molybdenum and Cobalt are the main alloying elements in MS 300 steels and while Co raises the elastic stiffness of iron, Ni and Mo cause a reduction. Among them, nickel is the one that most affects the elastic properties. Co and Mo have very little effect on Young's modulus, the shear modulus, and Poisson's ratio, that is, on elastic constants that are determined either entirely or largely by the resistance of a material to shear deformations. After heat treatment, a slight change in the elastic modulus of the specimens occurs. The reason of this change can be explained that alloying elements like Ni, Mo and Co are distributed uniformly in the matrix in annealed conditions while Ni_3Mo precipitates are formed during aging processes, so that changes in elastic properties are seen [127].

Fractographs of the specimens are presented in Figure 4.13. Although they have similar fracture nucleation sites such as voids, splats, unmelted powder particles and cavities, all aged specimens reveal quasi cleavage decohesion fracture mechanisms whereas dimple-like ductile fracture surfaces are observed in the as-built and solution treated specimens. These fractographic images are somewhat similar to those given in previous studies [6], [10]–[12], [92], [100]. The non-heat treated and solution treated specimens (Figure 4.13 (a) and (b)) have a typical ductile trans-granular fracture with the formation of dimples [128]. These dimples indicate good plasticity corresponding to the high elongation. Meanwhile, the co-existing deep holes have resulted from the SLM process caused by molten liquid shrinkage or vaporization. When cavities originated by incomplete melting between adjacent layers arise at the unmelted powder particles or precipitates under plastic deformation, they lead to larger stresses so that more microcavities come into existence. Eventually, conjoin of microcavities together, and fast growth of crack cause the fracture. On the other hand, cleavage features are seen in the aged specimens which have brittle fracture mechanisms. Lath martensite packets and boundaries appear in these surfaces, and crack growth direction is parallel to the slats. There is no sign of any plastic deformation, and shallow dimples exist so that both inter- and trans-granular fractures appear, as shown in Figure 4.13 (c) to (e). Specimens that were aged after solution treating have a different surface morphology when compared to directly aged ones. Flat fracture surfaces and cleavage features were obvious in this specimen. Furthermore, dimple features were also observed, as shown in Figure 4.13 (c) and (d).

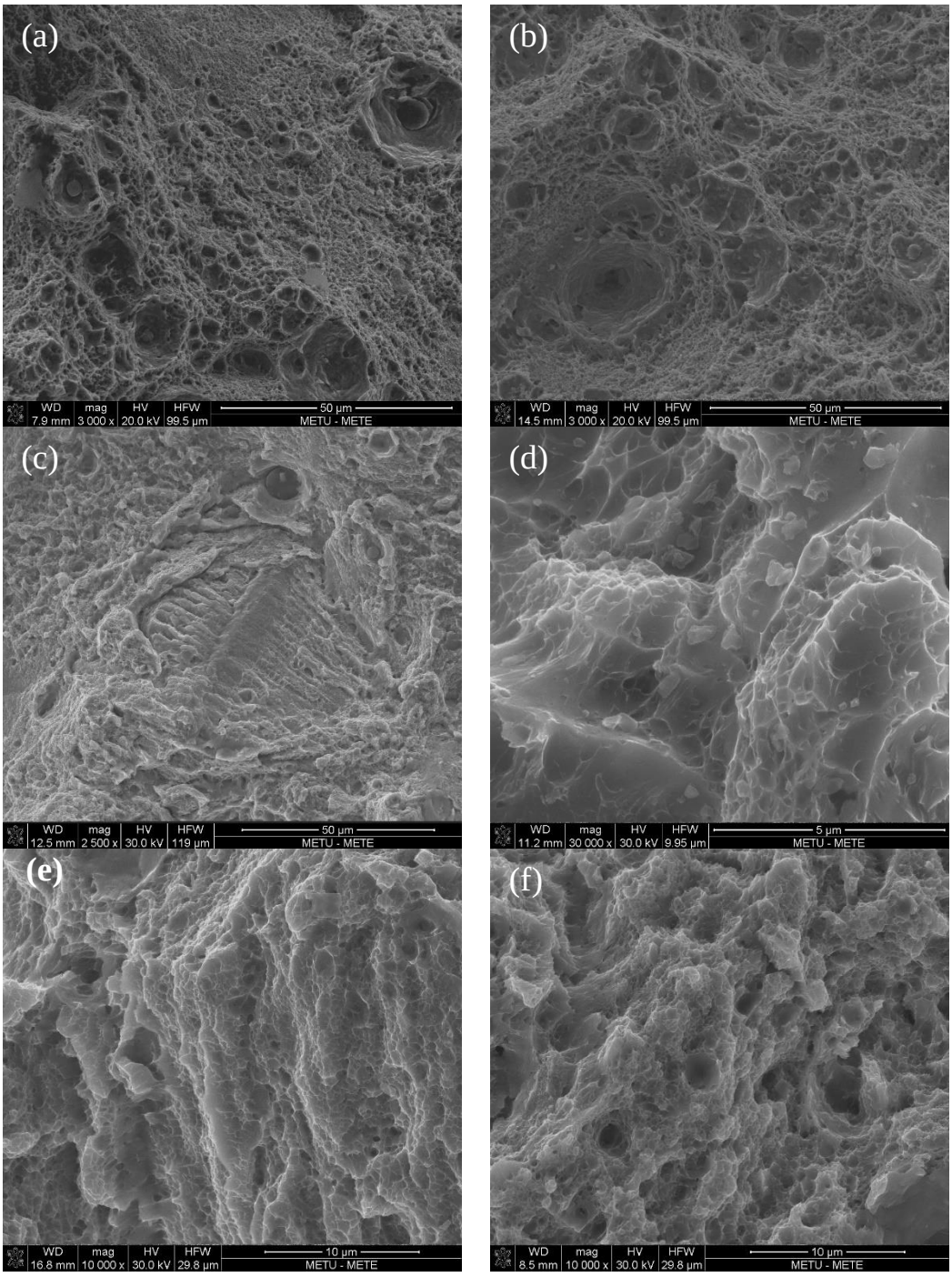

Figure 4.13. Fractographs of tensile test specimens; (a) as-built, (b) solution treated at 900 °C, (c) aged at 490 °C for 6 hr, (d) solution treated at 900 °C & aged at 490°C for 6 hr, (e) aged at 450 °C for 6 hr, (f) aged at 590 °C for 6 hr

4.2.3.2 Hardness Measurement Results

The comparative hardness values of the as-built and heat-treated specimens are given in Figure 4.14. In theory, solution treatment improves the hardness, but this is not valid for SLM produced MS300 steel due to microstructural difference between additive and conventional manufacturing. The high cooling rate of SLM results in fine cellular structure with intercellular spacing less than 1 μm and higher residual stresses so that hardness is improved [129]. However, after solution treatment, disappearing of cellular structure, grain growth, elimination of micro segregation and releasing of residual stresses lead to easily spreading of dislocations and reduction of hardness [130]. As can be seen in Figure 4.14 (a), hardness drops from 370 HV to 320 HV when as-built specimens were subjected to the solution treatment. As mentioned before, solidification traces and scan tracks in the as-built specimen were completely disappeared and also segregation of alloying elements at melting boundaries was eliminated after solution treatment. For that reasons, solution treatment caused a 50 HV reduction in hardness.

Significant improvement in hardness is observed after aging treatment. 610 HV was obtained after 6 hr aging at 490 °C due to precipitation hardening which is the primary strengthening mechanism of maraging steels. During aging treatment, elements like Ni, Mo, and Ti dissolved in the low C martensitic matrix form intermetallic precipitates such as Ni_3Mo, Fe_2Mo, and Ni_3Ti. These second phase precipitates strengthen the matrix by hindering the dislocation movement [5], [123].

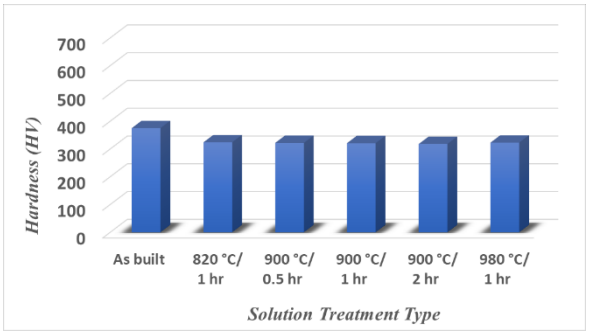

(a)

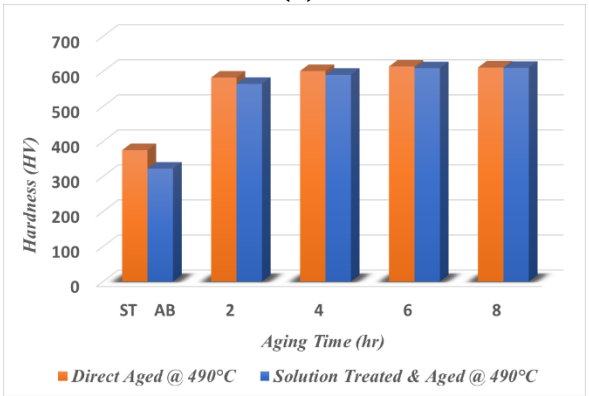

(b)

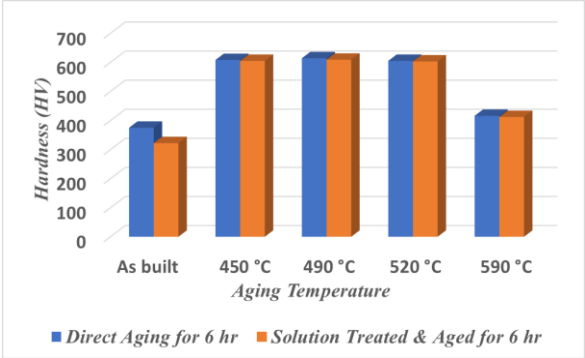

(c)

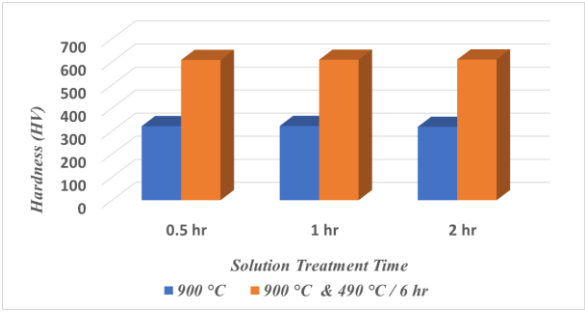

(d)

Figure 4.14. The hardness of MS300 steel at different heat treatments; (a) Solution treated at different temperatures b) Aging at different times c) Aging at different temperatures d) Solution treated at different times

Aging treatment increases the hardness due to the precipitation hardening. To investigate the effect of aging temperature and holding time on the hardness of MS300 maraging steel, Figure 4.15 is constructed. Peak hardness is achieved at 490 °C because of the precipitation of the main intermetallic compounds of $Ni_3(Ti, Mo)$. Under aging conditions is satisfied at lower aging temperature (400 °C), and μ, S and X intermetallic compounds which are softer than Ni3Ti are precipitated in this region, and at higher aging temperatures (590°C), hardness is reduced due to the decomposition of intermetallics and formation of reverted austenite [77], [83], [131]. Figure 4.15 (b) shows the effect of holding time on the hardness of the MS300 maraging steels. The hardness rapidly increased to 520 HV after only 30 minutes. Hardness reaches its peak level (610 HV) after 6-hour aging at 490 °C, and then, starts to decrease slightly with time. The reason of this behavior is insufficient strengthening due to the less precipitation at the short aging times and more austenite transformation at longer holding times.

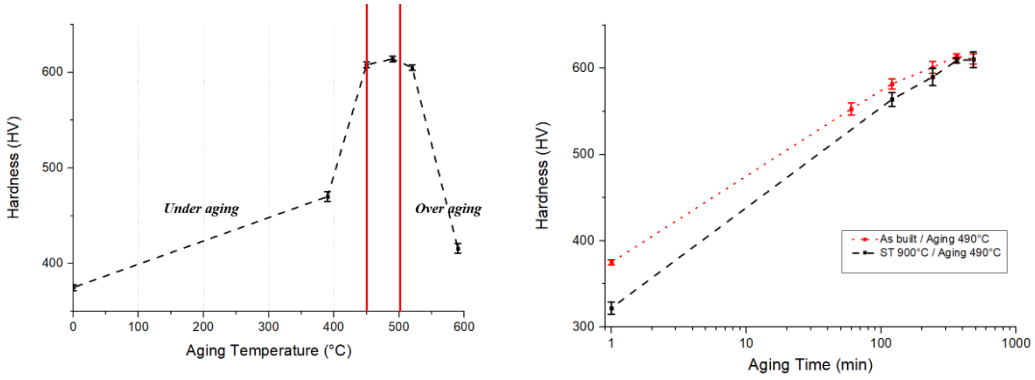

(a) **(b)**

Figure 4.15. Variation of hardness as a function of (a) aging temperature for 6 hr (b) aging time at 490°C

Finally, the difference in hardness between solution treated & aged and directly aged specimens are compared. As can be seen in Figure 4.14 (b) to (c) and Figure 4.15 (b), the gap between the hardness difference of the as-built and solution treated specimens gradually decreases as aging proceeds. After 2 hour aging, hardness values converge and remain similar rest of the process. As mentioned before, the reason for the highest hardness in the as-built specimen when compared to solution treated ones could be the fine cellular structure of the as-built specimen that leads to Hall-Petch strengthening or formation of precipitates or dislocations during SLM due to its high cooling rate [88]. So, it can be concluded that the effect of these factors is eliminated at longer aging times, and precipitation of Ni_3(Ti, Mo) intermetallic compounds become more dominant on strengthening mechanisms.

Moreover, when anisotropic behavior of specimens is considered, the situation valid for the as-built specimen (as mentioned in Section 4.1.3) is valid for heat-treated specimens. Both of the as-built and heat-treated specimens show no apparent anisotropic behavior under the same condition of heat treatment. Aged at 490 °C for 6-hour specimen has a 614 HV, 610 HV and 609 HV from Surface 1 to Surface 3, respectively and specimen which is firstly solution treated at 900 °C and then aged at 490 °C for 6 hr has a hardness value of 609 HV, 604 HV and 608 HV in each surface. So, this shows that heat-treated specimens also have a no anisotropic behavior like the as-built specimens and even a peak hardness value, which is approximately 610 HV could be obtained at aging 490 °C for 6 hours almost regardless of solution treatment condition. All hardness measurement results are listed in Appendix A. Results about the anisotropic behavior, and the effect of solution treatment on peak hardness is in agreement with other studies [5], [6], [9], [92].

4.3 Determination of Mechanical Properties with Ultrasonic Wave Velocity Measurement

Ultrasonic wave velocity depends on several material properties such as density (ρ), young modulus (E) and Poisson's ratio (v). If there exists change in any or combination of them, this change redounds up the sound of speed (V), as indicated in Equation 4.1.

$$V = \sqrt{\frac{E(1-v)}{\rho(1+v)(1-2v)}} \qquad \textit{Equation 4.1}$$

Both longitudinal and shear wave velocities were measured by using the appropriate transducers. In the pulse-echo technique, wave velocities are calculated by dividing the total trip distance to the Time of Flight (ToF). Wave velocity will indicate the material properties along the path of propagation. Still, it will not reveal if spatial heterogeneity of properties is present.

$$V = \frac{2L}{ToF} \qquad \textit{Equation 4.2}$$

After both longitudinal (V_L) and transverse (V_T) wave velocities are calculated, their units converted to centimeters per second, and then, they are inserted into Equation 4.3 – 4.5 in order to calculate the Poisson's ratio, Young's Modulus and Shear Modulus.

$$Poisson's\ Ratio\ (v) = \frac{1-2(V_T/V_L)^2}{2-2(V_T/V_L)^2} \qquad \textit{Equation 4.3}$$

$$Young\ Modulus\ (E) = \frac{{V_L}^2\rho(1+v)(1-2v)}{1-v} \qquad \textit{Equation 4.4}$$

$$Shear\ Modulus\ (G) = {V_T}^2\rho \qquad \textit{Equation 4.5}$$

Table 4.4 includes both transverse and longitudinal wave velocities and ultrasonically calculated elastic properties. Wave velocities were obtained by averaging at least three measurements.

Table 4.4 Longitudinal and transverse wave velocities and calculated elastic properties of the specimens

	V_T (m/s)	V_L (m/s)	ν	G (GPa)	$E_{ultrasonic}$ (GPa)	$E_{mechanical}$ (GPa)	ΔE (GPa)
As-built	2886	5546	0.31	65 ± 0	171±0.2	173 ± 1	2
450 °C / 6 hr	2920	5618	0.32	67 ± 0	175±0	174 ± 2	1
490 °C / 6 hr	2987	5714	0.31	70 ± 0	183±0	182 ± 1	1
520 °C / 6 hr	3019	5578	0.29	71 ± 1	184±0.9	181 ± 1	3
590 °C / 6 hr	2966	5349	0.28	69 ± 0	175±0.5	175 ± 2	0
490 °C / 1 hr	2916	5693	0.32	66 ± 0	175±0.7	173 ± 1	2
490 °C / 2 hr	2926	5721	0.32	67 ± 0	177±0.7	174 ± 3	3
490 °C / 4 hr	2942	5732	0.32	68 ± 2	178±2.3	175 ± 1	3
490 °C / 8 hr	2937	5682	0.32	67 ± 0	177±0.3	180 ± 3	3
820 °C / 1 hr	2826	5552	0.33	62 ± 1	165±0.7	166 ± 1	1
900 °C / 1 hr	2826	5528	0.32	62 ± 0	165±0	164 ± 1	1
980 °C / 1 hr	2836	5526	0.32	64 ± 0	168±0.7	170 ± 1	2
900°C/ 1hr & 490°C/ 2 hr	2930	5807	0.33	67 ± 0	177±0.2	175 ± 1	2
900°C/ 1hr & 490°C/ 4 hr	2968	5811	0.32	69 ± 0	182±0.1	180 ± 2	2
900°C/ 1hr & 490°C/ 6 hr	3012	5854	0.32	71 ± 0	187±0.5	185 ± 2	2
900°C/ 1hr & 450°C/ 6 hr	2996	5580	0.30	70 ± 0	182±0.1	182 ± 1	0
900°C/ 1hr & 520°C/ 6 hr	3040	5599	0.29	72 ± 1	186±2.3	184 ± 2	2
900°C/ 1hr & 590°C/ 6 hr	2954	5309	0.32	68 ± 1	174±0.4	177 ±2	3

Elastic modulus values determined via ultrasonic measurements are almost identical to those obtained from the tensile tests. Consequently, these results show that ultrasonic wave velocity measurement could be used to determine the elastic properties of additively manufactured MS300 specimens nondestructively. Furthermore, it might be possible to use ultrasonic parameters for the assessment of several mechanical properties such as hardness, yield strength, and fracture toughness.

The variation of hardness and longitudinal wave velocity with aging time is shown in Figure 4.16. The wave velocities and hardness have a similar trend. Initially, both of them increase with aging time, after reaching a maximum at intermediate durations, they exhibit a decrease at longer aging times. The initial increase is caused by precipitation of Ni_3Ti intermetallics. Upon precipitation of Ni_3Ti intermetallics, solute elements, such as Ni and Ti, are depleted from the matrix. Hence, an increase in the Young's modulus and the ultrasonic velocity is expected. The continuous increase in hardness and sound velocity with increasing aging duration are attributed to precipitation of fine Fe_2Mo precipitates from the solid solution. Finally, the decrease in these properties upon aging for longer time is attributed to the formation of reverted austenite which lowers hardness and sound velocity. Austenite is the softest phase of steel, and it has the lowest elastic modulus. Thus, a decrease in hardness and longitudinal wave velocity is observed after longer aging time. This is attributed to the fact that the precipitation of Fe_2Mo, which tends to increase the hardness and sound velocity, continues to take place in parallel with the phenomenon of reversion to austenite. Hence, reduction in the hardness and longitudinal wave velocity due to the formation of reverted austenite can occur, only if strengthening due to Fe_2Mo precipitation has a negligible effect.

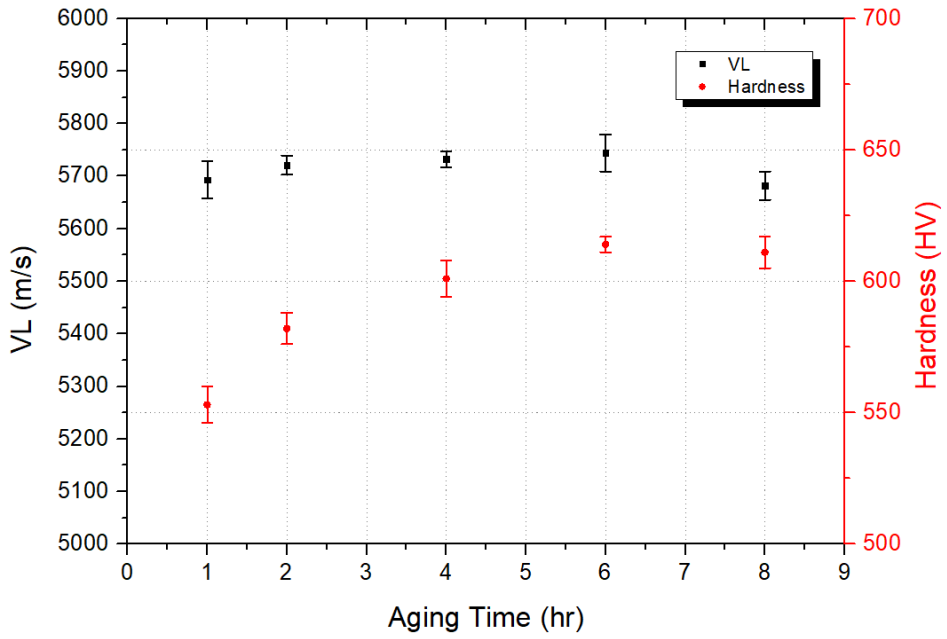

Figure 4.16. Variation of V_L and hardness with aging time at 490 °C

Figure 4.17 shows the variation of longitudinal wave velocity and hardness with the aging temperature. Sound velocity increases with increasing aging temperature up to 490 °C; however, further increase in temperature reduces the sound velocity. The similar trend exists for variation of hardness with aging temperature. The variations in sound velocities of MS250 and MS300 steels with aging were investigated by Yeheskel [132] and Behjati et al. [133], respectively. They reported that as aging temperature increases, longitudinal wave velocity decreases severely due to the formation of reverted austenite. This behavior is attributed to the increase in Ni concentration in the matrix which reduces the elastic modulus.

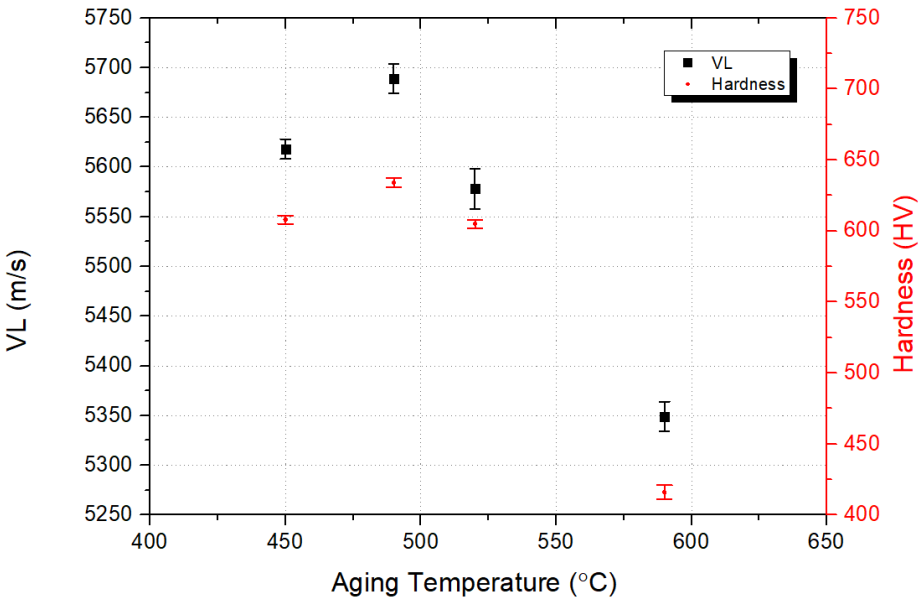

Figure 4.17. Variation of V_L and hardness with aging temperature for the constant aging time of 6 hr

CHAPTER 5

CONCLUSION

In this thesis, the effects of process parameters of solutionizing and aging heat treatments on microstructure and mechanical properties of the additively manufactured 18Ni300 (MS300) maraging steel specimens have been investigated. The specimens were produced via direct metal laser solidification (DMLS) method. Microstructures of the as-built and heat-treated specimens were characterized via optical and scanning electron microscopy and X-ray diffraction. Hardness measurements and tensile tests were performed for mechanical characterization. Both longitudinal and transverse ultrasonic wave velocities of all specimens were measured to establish correlations between hardness, elastic properties and sound velocity.

The following conclusions can be drawn from the results of this particular study;

- Specimens having nearly 99.2 % average relative density can be produced with a laser energy density of 59.5 J/mm^3. The average surface roughness values of the specimens are 4.34 μm and 5.35 μm in the horizontal and vertical surfaces, respectively. The reason of this difference is the process parameters of the SLM. Short scan length causes a high heat flow on the solidified layers in the building direction, and thus, surface roughness increases.

- As-built specimens have different microstructural features in comparison to as-cast and wrought ones. Typical signs of SLM (motion track of laser beam and laser scan angle) are seen in the as-built specimens. All as-built specimens consist of sub-micron dendritic cellular structures in the horizontal cross-section and elongated acicular structures in the vertical cross-section.

They have a bcc-type martensitic structure due to the very low C-content. Also, some amount of austenite exists at the cell boundaries due to the non-homogenous distribution of alloying elements at the boundaries.

- Phase transformation temperatures of the as-built specimens, which indicate the temperature ranges of aging treatment and solution treatment, were found as 453 °C, 530 °C, 648 °C and 760 °C from the DSC curves. Since the main strengthening mechanism for the as-built specimens is related to the precipitation of Ni_3Ti and Ni_3Mo that is occurred within the range of 450 °C to 530 °C, the aging treatment was applied at 450 °C to 590 °C. Also, although 760 °C would be sufficient, the solution treatment was applied between 820 °C to 980 °C due to the elimination of microsegregation in the as-built specimens.
- Solution treatment has a significant effect on microstructure. After solution treatment,
    a) all melt pools and laser tracks are completely disappeared,
    b) a coarse lath type martensitic structure is obtained instead of cellular morphology, and
    c) due to the elimination of the heterogeneous distribution of the alloying elements, retained austenite existing in the as-built specimens completely transforms into the martensite, and 100 % martensitic structure forms.
- The effect of aging treatment on microstructure varies with aging time and temperature. With the increasing time and temperature, melting pools gradually starts to be blurred, but never completely disappear. However, at higher aging temperatures (such as 590 °C), over-aging takes place and a disparate structure forms. Instead of lath martensite, an austenitic and martensitic structure appears due to the austenite reversion.

- Due to the microstructural changes (disappearance of cellular structure) and precipitation of intermetallics such as Ni_3Mo, Fe_2Mo and Ni_3Ti, significant changes in the mechanical properties occur after heat treatments. Solution treatment of the as-built specimens causes reductions in the values of hardness and tensile strength due to the transformation of fine-grained martensitic structure to the lath type martensite, and also, relief of residual stresses. The hardness drops from 370 HV to 320 HV, and the tensile strength drops from 1203 to 1124 MPa. Besides, anisotropies in the top and lateral surfaces of the as-built specimens disappear after solution treatment, and homogeneous properties are obtained. On the other hand, aging treatment strengthen the matrix due to precipitation hardening and in optimum conditions which is found as 6 hr aging at 490 °C, 610 HV hardness and 2181 MPa tensile strength are obtained.
- The fracture surfaces of the as-built and solution treated specimens contain dimples indicating the ductile fracture behavior. However, aged specimens show brittle fracture behavior that is characterized by the presence of river pattern-like steps, lath packets, cracks, and shallow and deformed dimples.
- Non-destructive determination of the mechanical properties of the additively manufactured and heat-treated 18Ni300 maraging steels via ultrasonic wave speed measurement seems to be very promising for industrial applications. For determination of the elastic modulus almost identical results are obtained from the tensile tests and sound velocity measurements. Besides, variations in hardness can be monitored via sound velocity measurements. The hardness increased due to precipitation hardening causes the increase of sound velocity. It can be attributed to the increased volume fraction of incoherent precipitates, which contributes to the increase in the elastic modulus value of the age-hardened specimens.

5.1 Recommendation for Further Studies

The following issues are recommended as future studies:

- Determine the amount, shape and size of the intermetallic precipitates formed after aging treatment by TEM investigations; and elaborate the effect of these factors on the mechanical properties.
- EBSD analysis to determine the crystallographic orientation and texture, and EBSD phase mapping to further reveal the phase composition after heat treatments.
- Fatigue test to predict the expected lifetime of additively manufactured and heat-treated specimens.
- Investigation of mechanical properties of real engineering components produced by SLM via ultrasonic wave velocity measurements.
- Investigation of aging behavior via other non-destructive methods such as measuring electrical and magnetic properties.

REFERENCES

[1] G. Casalino, S. L. Campanelli, N. Contuzzi, and A. D. Ludovico, "Experimental investigation and statistical optimisation of the selective laser melting process of a maraging steel," Opt. Laser Technol., vol. 65, pp. 151–158, 2015.

[2] Y. Bai, Y. Yang, D. Wang, and M. Zhang, "Influence mechanism of parameters process and mechanical properties evolution mechanism of maraging steel 300 by selective laser melting," Mater. Sci. Eng. A, vol. 703, pp. 116–123, Aug. 2017.

[3] J. Mutua, S. Nakata, T. Onda, and Z.-C. Chen, "Optimization of selective laser melting parameters and influence of post heat treatment on microstructure and mechanical properties of maraging steel," Mater. Des., vol. 139, pp. 486–497, 2018.

[4] J. Suryawanshi, K. G. Prashanth, and U. Ramamurty, "Tensile, fracture, and fatigue crack growth properties of a 3D printed maraging steel through selective laser melting," J. Alloys Compd., vol. 725, pp. 355–364, 2017.

[5] S. Yin, C. Chen, X. Yan, X. Feng, R. Jenkins, P. O'Reilly, M. Liu, H. Li, R. Lupoi,, "The influence of aging temperature and aging time on the mechanical and tribological properties of selective laser melted maraging 18Ni-300 steel," Addit. Manuf., vol. 22, pp. 592–600, 2018.

[6] R. Casati, J. Lemke, A. Tuissi, and M. Vedani, "Aging Behaviour and Mechanical Performance of 18-Ni 300 Steel Processed by Selective Laser Melting," Metals 2016, vol. 6, no. 9, p. 218, Sep. 2016.

[7] R. Casati, J. Lemke, and M. Vedani, "Microstructural and Mechanical Properties of As Built, Solution Treated and Aged 18 Ni (300 grade) Maraging Steel Produced by Selective Laser Melting," Metall. Ital., vol. 109, no. 1, 2017.

[8] C. Tan, K. Zhou, X. Tong, Y. Huang, J. Li, W. Ma, F. Li, T. Kuang, "Microstructure and Mechanical Properties of 18Ni-300 Maraging Steel Fabricated by Selective Laser Melting BT - 2016 6th International Conference on Advanced Design and Manufacturing Engineering (ICADME 2016)," pp. 404–410,2017.

[9] C. Tan, K. Zhou, W. Ma, P. Zhang, M. Liu, and T. Kuang, "Microstructural evolution, nanoprecipitation behavior and mechanical properties of selective laser melted high-performance grade 300 maraging steel," Mater. Des., vol. 134, pp. 23–34, 2017.

[10] C. Tan, K. Zhou, M. Kuang, W. Ma, and T. Kuang, “Microstructural characterization and properties of selective laser melted maraging steel with different build directions,” Sci. Technol. Adv. Mater., vol. 19, no. 1, pp. 746–758, Dec. 2018.

[11] Y. Bai, D. Wang, Y. Yang, and H. Wang, “Effect of heat treatment on the microstructure and mechanical properties of maraging steel by selective laser melting,” Mater. Sci. Eng. A, vol. 760, pp. 105–117, 2019.

[12] K. Kempen, E. Yasa, L. Thijs, J.-P. Kruth, and J. Van Humbeeck, “Microstructure and mechanical properties of Selective Laser Melted 18Ni-300 steel,” Phys. Procedia, vol. 12, pp. 255–263, 2011.

[13] ASTM 52921, “Standard Terminology for Additive Manufacturing — Coordinate Systems and Test Methodologies,” *ASTM Int.*, vol. I, pp. 1–13, 2013.

[14] E. Sachs, M. Cima, and J. Cornie, “Three-Dimensional Printing: Rapid Tooling and Prototypes Directly from a CAD Model,” *CIRP Ann. - Manuf. Technol.*, vol. 39, pp. 201–204, 1990.

[15] P. F. Jacobs, “*Stereolithography and other RP & M technologies : from rapid prototyping to rapid tooling*, ” Dearborn, Mich.; New York: Society of Manufacturing Engineers in cooperation with the Rapid Prototyping Association of SME ; ASME Press, vol. 4, no. 2, 1996.

[16] D. Gu, “*Laser additive manufacturing of high-performance materials*, ” Springer, pp. 15–71, 2015.

[17] I. Gibson, D. Rosen, and B. Stucker, “*Additive manufacturing technologies: 3D printing, rapid prototyping, and direct digital manufacturing, second edition*, ” Springer, pp. 1–71, 2015.

[18] M. LaMonica, “*Additive manufacturing*, ” vol. 116, no. 3, pp.58–59, 2013.

[19] L. Lü, J. Y. H. Fuh, and Y. S. Wong, “*Laser-Induced Materials and Processes for Rapid Prototyping*, ” Springer, 2001.

[20] N. Guo and M. C. Leu, “Additive manufacturing: Technology, applications and research needs,” *Frontiers of Mechanical Engineering*, vol. 8, no. 3, p. 215–243, 2013.

[21] K. V. Wong and A. Hernandez, “A Review of Additive Manufacturing,” *ISRN Mech. Eng.*, vol. 2012, pp. 1–10, 2012.

[22] H. Bikas, P. Stavropoulos, and G. Chryssolouris, “Additive manufacturing methods and modeling approaches: A critical review,” *Int. J. Adv. Manuf. Technol.*, vol. 83, no. 1–4, pp. 389–405, 2016.

[23] M. Yakout, M. A. Elbestawi, and S. C. Veldhuis, “A review of metal additive manufacturing technologies,” *Solid State Phenom.*, vol. 278, pp. 1–14, 2018.

[24] K. Salonitis, G. Tsoukantas, P. Stavropoulos, and A. Stournaras, “A critical review of stereolithography process modeling,” in *Virtual Modelling and Rapid Manufacturing - Advanced Research in Virtual and Rapid Prototyping*, 2003.

[25] N. B. Dahotre and S. P. Harimkar, “*Laser fabrication and machining of materials*,” Springer, pp. 353–411, 2008.

[26] J. P. Kruth, “Material Incress Manufacturing by Rapid Prototyping Techniques,” *CIRP Ann. - Manuf. Technol.*, vol. 40, no. 2, pp. 603–614, 1991.

[27] S. F. S. Shirazi, S. Gharehkhani, M. Mehrali, H. Yarmand, H. S. C. Metselaar, N. A. Kadri, and N. A. A. Osman, “A review on powder-based additive manufacturing for tissue engineering: Selective laser sintering and inkjet 3D printing,” *Science and Technology of Advanced Materials*, vol. 16, no. 3, 2015.

[28] W. Gao, Y. Zhang, D. Ramanujan, K. Ramani, Y. Chen, C. B. Williams, C. C. L. Wang, Y. C. Shin, S. Zhang, and P. D. Zavattieri, “The status, challenges, and future of additive manufacturing in engineering,” *CAD Comput. Aided Des.*, vol. 69, pp. 65–89, 2015.

[29] A. Woesz, “Rapid Prototyping to Produce Porous Scaffolds With Controlled Architecture for Possible use in Bone Tissue Engineering,” in *Virtual Prototyping & Bio Manufacturing in Medical Applications*, B. Bidanda and P. Bártolo, Eds. Boston, MA: Springer US, pp. 171–206, 2008.

[30] D. Günther, B. Heymel, J. F. Günther, and I. Ederer, “Continuous 3D-printing for additive manufacturing,” *Rapid Prototyp. J.*, vol. 20, no. 4, pp. 320–327, 2014.

[31] E. C. Santos, M. Shiomi, K. Osakada, and T. Laoui, “Rapid manufacturing of metal components by laser forming,” *Int. J. Mach. Tools Manuf.*, vol. 46, no. 12–13, pp. 1459–1468, 2006.

[32] B. C. Gross, J. L. Erkal, S. Y. Lockwood, C. Chen, and D. M. Spence, “Evaluation of 3D printing and its potential impact on biotechnology and the chemical sciences,” *Anal. Chem.*, vol. 86, no. 7, pp. 3240–3253, 2014.

[33] P. Vora, F. Derguti, K. Mumtaz, I. Todd, and N. Hopkinson, “Investigating a semi-solid processing technique using metal powder bed Additive Manufacturing processes,” in *24th International SFF Symposium - An Additive Manufacturing Conference, SFF 2013*, pp. 454–462, 2013.

[34] L. E. Murr, E. Martinez, K. N. Amato, S. M. Gaytan, J. Hernandez, D. A. Ramirez, P. W. Shindo, F. Medina, and R. B. Wicker, “Fabrication of metal and alloy components by additive manufacturing: Examples of 3D materials science,” *Journal of Materials Research and Technology*, vol.1, no. 1, pp. 42–54, 2012.

[35] W. Meiners, K. Wissenbach, and A. Gasser, “Shaped body especially prototype or replacement part production,” *Pat.*, vol. 19, 1998.

[36] C. K. Chua and K. F. Leong, “*3D Printing and Additive Manufacturing: Principles and Applications*,” World Scientific Publishing Company, 2014.

[37] C. Y. Yap, C. K. Chua, Z. L. Dong, Z. H. Liu, D. Q. Zhang, L. E. Loh, and S. L. Sing, “Review of selective laser melting: Materials and applications,” *Appl. Phys. Rev.*, vol. 2, no. 4, p.41101, 2015.

[38] H. M. Zaw, J. Y. H. Fuh, A. Y. C. Nee, and L. Lu, “Formation of a new EDM electrode material using sintering techniques,” *J. Mater. Process. Technol.*, vol. 89–90, pp. 182–186, 1999.

[39] R. Li, J. Liu, Y. Shi, L. Wang, and W. Jiang, “Balling behavior of stainless steel and nickel powder during selective laser melting process,” *Int. J. Adv. Manuf. Technol.*, vol. 59, no. 9, pp. 1025–1035, 2012.

[40] N. P. K. J. P. S. van Griethuysen, R. Glardon, and N. P. Karapatis, “Direct rapid tooling: a review of current research,” *Rapid Prototyp.*, vol. 4, no. 2, pp. 77–89, 1998.

[41] P. Krakhmalev and I. Yadroitsev, “Microstructure and properties of intermetallic composite coatings fabricated by selective laser melting of Ti–SiC powder mixtures,” *Intermetallics*, vol. 46, pp. 147–155, 2014.

[42] S. Das, “Physical aspects of process control in selective laser sintering of metals,” *Adv. Eng. Mater.*, vol. 5, no. 10, pp. 701–711, 2003.

[43] X. Wang, J. A. Muñiz-Lerma, M. A. Shandiz, O. Sanchez-Mata, and M. Brochu, “Crystallographic-orientation-dependent tensile behaviours of stainless steel 316L fabricated by laser powder bed fusion,” *Mater. Sci. Eng. A*, vol. 766, p. 138-395, 2019.

[44] Z. Sun, X. Tan, S. B. Tor, and C. K. Chua, “Simultaneously enhanced strength and ductility for 3D-printed stainless steel 316L by selective laser melting,” *NPG Asia Mater.*, vol. 10, no. 4, pp. 127–136, 2018.

[45] M. Shamsujjoha, S. R. Agnew, J. M. Fitz-Gerald, W. R. Moore, and T. A. Newman, “High strength and ductility of additively manufactured 316L stainless steel explained,” *Metall. Mater. Trans. A*, vol. 49, no. 7, pp. 3011–3027, 2018.

[46] S. Bahl, S. Mishra, K. U. Yazar, I. R. Kola, K. Chatterjee, and S. Suwas, “Non-equilibrium microstructure, crystallographic texture and morphological texture synergistically result in unusual mechanical properties of 3D printed 316L stainless steel,” *Addit. Manuf.*, vol. 28, pp. 65–77, 2019.

[47] H. K. Rafi, D. Pal, N. Patil, T. L. Starr, and B. E. Stucker, “Microstructure and mechanical behavior of 17-4 precipitation hardenable steel processed by selective laser melting,” *J. Mater. Eng. Perform.*, vol. 23, no. 12, pp. 4421–4428, 2014.

[48] L. Facchini, N. Vicente Jr, I. Lonardelli, E. Magalini, P. Robotti, and A. Molinari, “Metastable austenite in 17–4 precipitation-hardening stainless steel produced by selective laser melting,” *Adv. Eng. Mater.*, vol. 12, no. 3, pp. 184–188, 2010.

[49] A. Kudzala, B. McWilliams, C. Hofmeister, F. Kellogg, J. Yu, J. Taggart-Scarff, and J. Liang, “Effect of scan pattern on the microstructure and mechanical properties of powder bed fusion additive manufactured 17-4 stainless steel,” *Mater. Des.*, vol. 133, pp. 205–215, 2017.

[50] X. P. Li, J. Van Humbeeck, and J.-P. Kruth, “Selective laser melting of weak-textured commercially pure titanium with high strength and ductility: A study from laser power perspective,” *Mater. Des.*, vol. 116, pp. 352–358, 2017.

[51] L. Zhou, T. Yuan, J. Tang, J. He, and R. Li, “Mechanical and corrosion behavior of titanium alloys additively manufactured by selective laser melting–A comparison between nearly β titanium, α titanium and α+ β titanium,” *Opt. Laser Technol.*, vol. 119, p. 105625, 2019.

[52] B. Wysocki, P. Maj, A. Krawczyńska, K. Rożniatowski, J. Zdunek, K. J. Kurzydłowski, and W. Święszkowski, “Microstructure and mechanical properties investigation of CP titanium processed by selective laser melting (SLM),” *J. Mater. Process. Technol.*, vol. 241, pp. 13–23, 2017.

[53] R. Sabban, S. Bahl, K. Chatterjee, and S. Suwas, “Globularization using heat treatment in additively manufactured Ti-6Al-4V for high strength and toughness,” *Acta Mater.*, vol. 162, pp. 239–254, 2019.

[54] C. Madikizela, L. A. Cornish, L. H. Chown, and H. Möller, “Microstructure and mechanical properties of selective laser melted Ti-3Al-8V-6Cr-4Zr-4Mo compared to Ti-6Al-4V,” *Mater. Sci. Eng. A*, vol. 747, pp. 225–231, 2019.

[55] J. Yang, H. Yu, Z. Wang, and X. Zeng, “Effect of crystallographic orientation on mechanical anisotropy of selective laser melted Ti-6Al-4V alloy,” *Mater. Charact.*, vol. 127, pp. 137–145, 2017.

[56] L. Zhou, T. Yuan, J. Tang, L. Li, F. Mei, and R. Li, “Texture evolution, phase transformation and mechanical properties of selective laser melted Ti-13Nb-13Zr,” *Mater. Charact.*, vol. 145, pp. 185–195, 2018.

[57] K. G. Prashanth and J. Eckert, “Formation of metastable cellular microstructures in selective laser melted alloys,” *J. Alloys Compd.*, vol. 707, pp. 27–34, 2017.

[58] J. Suryawanshi, K. G. Prashanth, S. Scudino, J. Eckert, O. Prakash, and U. Ramamurty, “Simultaneous enhancements of strength and toughness in an Al-12Si alloy synthesized using selective laser melting,” *Acta Mater.*, vol. 115, pp. 285–294, 2016.

[59] X. P. Li, X. J. Wang, M. Saunders, A. Suvorova, L. C. Zhang, Y. J. Liu, M. H. Fang, Z. H. Huang, and T. B. Sercombe, “A selective laser melting and solution heat treatment refined Al–12Si alloy with a controllable ultrafine eutectic microstructure and 25% tensile ductility,” *Acta Mater.*, vol. 95, pp. 74–82, 2015.

[60] M. Liu, N. Takata, A. Suzuki, and M. Kobashi, “Microstructural characterization of cellular AlSi10Mg alloy fabricated by selective laser melting,” *Mater. Des.*, vol. 157, pp. 478–491, 2018.

[61] L. Thijs, K. Kempen, J.-P. Kruth, and J. Van Humbeeck, “Fine-structured aluminium products with controllable texture by selective laser melting of pre-alloyed AlSi10Mg powder,” *Acta Mater.*, vol. 61, no. 5, pp. 1809–1819, 2013.

[62] L. Zhou, A. Mehta, E. Schulz, B. McWilliams, K. Cho, and Y. Sohn, “Microstructure, precipitates and hardness of selectively laser melted AlSi10Mg alloy before and after heat treatment,” *Mater. Charact.*, vol. 143, pp. 5–17, 2018.

[63] ASM International, “Classification and Designation of Carbon and Low-Alloy Steels,” *ASM Handbook, Vol. 1 Prop. Sel. Irons, Steels, High-Performance Alloy.*, vol. 1, no. C, pp. 140–149, 1990.

[64] E. Yasa, K. Kempen, J. P. Kruth, L. Thijs, and H. J. Van, “Microstructure and mechanical properties of maraging steel 300 after selective laser melting,” in *21st Annual International Solid Freeform Fabrication Symposium - An Additive Manufacturing Conference, SFF 2010*, pp. 383–396, 2010.

[65] J. R. Mihalisin and C. G. Bieber, “Progress toward attaining theoretical strength with iron-nickel maraging steels,” *JOM 18*, pp. 1033–1036, 1966.

[66] C. G. Bieber, “20 and 25% Nickel Maraging Steels,” in *Seminar on Maraging Steels*, p. 10, 1962.

[67] A. M. Hall, “*Cobalt,* ” vol.24, pp.138–144, 1964.

[68] A. J. Decker, R. F., Eash, J. T., & Goldman, “18% Nickel maraging steel.,” *Trans. ASM*, vol. 55, pp. 58–76, 1962.

[69] A. Magnee, J. M. Drapier, D. Coutsouradis, L. Habrakan, and J. Dumont, “Cobalt-containing high-strength steels,” *Brussels: Centre d'Information du Cobalt*, 1974.

[70] V. 4 ASM International Handbook, “ASM Handbook: Heat Treating,” *Technology*, 2001.

[71] R. K. Wilson, T. M. S. F. M. Committee, M. Minerals, and M. S. Meeting, “*Maraging Steels: Recent Developments and Applications : Proceedings of a Symposium*, ” TMS, 1988.

[72] W. Sha and Z. Guo, “*Maraging steels: Modelling of microstructure, properties and applications*, ” Woodhead Publishing, 2009.

[73] C. Carson, “Heat Treating of Maraging Steels, *Heat Treating of Irons and Steels*, ” vol. 4D, ASM Handbook, Edited By Jon L. Dossett, George E. Totten, ASM International, pp. 468–480, 2014.

[74] W. Sha, “Steels: From materials science to structural engineering,” *Steels From Mater. Sci. to Struct. Eng.*, vol. 9781447148, pp. 141–161, 2013.

[75] U. K. Viswanathan, G. K. Dey, and M. K. Asundi, “Precipitation hardening in 350 grade maraging steel,” *Metall. Trans. A*, vol. 24, no. 11, pp. 2429–2442, 1993.

[76] E. I. Galindo-Nava, W. M. Rainforth, and P. E. J. Rivera-Díaz-del-Castillo, “Predicting microstructure and strength of maraging steels: Elemental optimisation,” *Acta Mater.*, vol. 117, pp. 270–285, 2016.

[77] R. Tewari, S. Mazumder, I. S. Batra, G. K. Dey, and S. Banerjee, “Precipitation in 18 wt% Ni maraging steel of grade 350,” *Acta Mater.*, vol. 48, no. 5, pp. 1187–1200, 2000.

[78] W. Sha, A. Cerezo, and G. D. W. Smith, “Phase chemistry and precipitation reactions in maraging steels: Part I. Introduction and study of Co-containing C-300 steel,” *Metall. Trans. A*, vol. 24, no. 6, pp. 1221–1232, 1993.

[79] J. B. Lecomte, C. Servant, and G. Cizeron, “A comparison of the structural evolution occurring during anisothermal or isothermal treatments in the case of nickel and manganese type maraging alloys,” *J. Mater. Sci.*, vol. 20, no. 9, pp. 3339–3352, 1985.

[80] C. Servant and N. Bouzid, “Influence of the increasing content of Mo on the precipitation phenomena occurring during tempering in the maraging alloy Fe-12Mn-9Co-5Mo,” *Acta Metall.*, vol. 36, no. 10, pp. 2771–2778, 1988.

[81] V. K. Vasudevan, S. J. Kim, and C. M. Wayman, “Precipitation reactions and strengthening behavior in 18 Wt Pct nickel maraging steels,” *Metall. Trans. A, Phys. Metall. Mater. Sci.*, vol. 21 A, no. 10, pp. 2655–2668, 1990.

[82] D. T. Peters, “A study on austenite reversion during aging of maraging steels,” *Trans. ASM*, vol. 61, p. 116, 1968.

[83] J. M. Pardal, S. S. M. Tavares, V. F. Terra, M. R. Da Silva, and D. R. Dos Santos, “Modeling of precipitation hardening during the aging and overaging of 18Ni-Co-Mo-Ti maraging 300 steel,” *J. Alloys Compd.*, vol. 393, no. 1–2, pp. 109–113, 2005.

[84] X. Li and Z. Yin, “Reverted austenite during aging in 18Ni(350) maraging steel,” *Mater. Lett.*, vol. 24, no. 4, pp. 239–242, 1995.

[85] R. Schnitzer, R. Radis, M. Nöhrer, M. Schober, R. Hochfellner, S. Zinner, E. Povoden-Karadeniz, E. Kozeschnik, and H. Leitner, “Reverted austenite in PH 13-8 Mo maraging steels,” *Mater. Chem. Phys.*, vol. 122, no. 1, pp. 138–145, 2010.

[86] H. Leitner, M. Schober, R. Schnitzer, and S. Zinner, “Strengthening behavior of Fe-Cr-Ni-Al-(Ti) maraging steels,” *Mater. Sci. Eng. A*, vol. 528, no. 15, pp. 5264–5270, 2011.

[87] K. Rohrbach, M. Schmidt, “Maraging Steels, Properties and Selection: Irons, Steels, and High-Performance Alloys, ” vol. 1, ASM Handbook, By ASM Handbook Committee, ASM International, p 793–800, 1990.

[88] E. A. Jägle, P.-P. Choi, J. Van Humbeeck, and D. Raabe, “Precipitation and austenite reversion behavior of a maraging steel produced by selective laser melting,” *J. Mater. Res.*, vol. 29, no. 17, pp. 2072–2079, Sep. 2014.

[89] W. Huang, W. Zhang, and X. Chen, “Effect of SLM Process Parameters on Relative Density of Maraging Steel (18Ni-300) Formed Parts,” *IOP Conf. Ser. Mater. Sci. Eng.*, vol. 774, no. 012027, pp. 1–8, 2020.

[90] Y. Yao, Y. Huang, B. Chen, C. Tan, Y. Su, and J. Feng, “Influence of processing parameters and heat treatment on the mechanical properties of 18Ni300 manufactured by laser based directed energy deposition,” *Opt. Laser Technol.*, vol. 105, pp. 171–179, 2018.

[91] A. Suzuki, R. Nishida, N. Takata, M. Kobashi, and M. Kato, “Design of laser parameters for selectively laser melted maraging steel based on deposited energy density,” *Addit. Manuf.*, vol. 28, pp. 160–168, 2019.

[92] J. Song, Q. Tang, Q. Feng, S. Ma, R. Setchi, Y. Liu, Q. Han, X. Fan, and M. Zhang, “Effect of heat treatment on microstructure and mechanical behaviours of 18Ni-300 maraging steel manufactured by selective laser melting,” *Opt. Laser Technol.*, vol. 120, no. 105725, pp. 1–11, 2019.

[93] T. Simson, J. Koch, J. Rosenthal, M. Kepka, M. Zetek, I. Zetková, G. Wolf, P. Tomčík, and J. Kulhánek, “Mechanical properties of 18Ni-300 maraging steel manufactured by LPBF,” *Procedia Struct. Integr.*, vol. 17, pp. 843–849, 2019.

[94] M. Simonelli, Y. Tse, and C. Tuck, “Microstructure and Mechanical Properties of Ti-6A1-4V Fabricated by Selective Laser Melting,” TMS Annu. Meet., vol. 1, pp. 863–870, May 2012.

[95] L. M. S. Santos, L. P. Borrego, J. A. M. Ferreira, J. de Jesus, J. D. Costa, and C. Capela, “Effect of heat treatment on the fatigue crack growth behaviour in additive manufactured AISI 18Ni300 steel,” *Theor. Appl. Fract. Mech.*, vol. 102, pp. 10–15, 2019.

[96] B. Mooney, K. I. Kourousis, R. Raghavendra, and D. Agius, “Process phenomena influencing the tensile and anisotropic characteristics of additively manufactured maraging steel,” *Mater. Sci. Eng. A*, vol. 745, pp. 115–125, Feb. 2019.

[97] B. Mooney, K. I. Kourousis, and R. Raghavendra, “Plastic anisotropy of additively manufactured maraging steel: Influence of the build orientation and heat treatments,” *Addit. Manuf.*, vol. 25, pp. 19–31, 2019.

[98] G. Meneghetti, D. Rigon, D. Cozzi, W. Waldhauser, and M. Dabalà, “Influence of build orientation on static and axial fatigue properties of maraging steel specimens produced by additive manufacturing,” *Procedia Struct. Integr.*, vol. 7, pp. 149–157, 2017.

[99] F. Liu, X. Lin, J. Shi, Y. Zhang, P. Bian, X. Li, and Y. Hu, “Effect of microstructure on the Charpy impact properties of directed energy deposition 300M steel,” *Addit. Manuf.*, vol. 29, p. 100795, 2019.

[100] D. Kim, T. Kim, K. Ha, J. Oak, J. B. Jeon,Y. Park, and W. Lee, “Effect of heat treatment condition on microstructural and mechanical anisotropies of selective laser melted maraging 18Ni-300 steel,” *Metals*, vol. 10, no. 3, pp. 1–15, 2020.

[101] E. A. Jägle, Z. Sheng, P. Kürnsteiner, S. Ocylok, A. Weisheit, and D. Raabe, “Comparison of maraging steel micro- and nanostructure produced conventionally and by laser additive manufacturing,” *Materials.*, vol. 10, no. 1, pp. 1–15, 2017.

[102] A. G. Dos Reis, D. A. P. Reis, A. J. Abdalla, and J. Otubo, “High-temperature creep resistance and effects on the austenite reversion and precipitation of 18 Ni (300) maraging steel,” *Mater. Charact.*, vol. 107, pp. 350–357, 2015.

[103] A. F. de Souza, K. S. Al-Rubaie, S. Marques, B. Zluhan, and E. C. Santos, “Effect of laser speed, layer thickness, and part position on the mechanical properties of maraging 300 parts manufactured by selective laser melting,” *Mater. Sci. Eng. A*, vol. 767, p. 138425, 2019.

[104] C. Chen, X. Yan, Y. Xie, R. Huang, M. Kuang, W. Ma, R. Zhao, J. Wang, M. Liu, Z. Ren, and H. Liao, "Microstructure evolution and mechanical properties of maraging steel 300 fabricated by cold spraying," *Mater. Sci. Eng. A*, vol. 743, pp. 482–493, 2019.

[105] S. L. Campanelli, N. Contuzzi, P. Posa, and A. Angelastro, "Study of the aging treatment on selective laser melted maraging 300 steel," *Mater. Res. Express*, vol. 6, no. 6, 2019.

[106] S. Bodziak, K. S. Al-Rubaie, L. Di. Valentina, F. H. Lafratta, E. C. Santos, A. M. Zanatta, and Y. Chen, "Precipitation in 300 grade maraging steel built by selective laser melting: Aging at 510 °C for 2 h," *Mater. Charact.*, vol. 151, pp. 73–83, 2019.

[107] T. Bhardwaj and M. Shukla, "Direct Metal Laser Sintering of Maraging Steel: Effect of Building Orientation on Surface Roughness and Microhardness," *Mater. Today Proc.*, vol. 5, no. 9, pp. 20485–20491, 2018.

[108] T. Bhardwaj and M. Shukla, "Effect of laser scanning strategies on texture, physical and mechanical properties of laser sintered maraging steel," *Mater. Sci. Eng. A*, vol. 734, pp. 102–109, 2018.

[109] T. Bhardwaj and M. Shukla, "Effect of scan direction on tensile properties and fractography of laser additive manufactured maraging steel," *Mater. Today Proc.*, vol. 18, pp. 3842–3848, 2019.

[110] T. H. Becker and Di. DImitrov, "The achievable mechanical properties of SLM produced Maraging Steel 300 components," *Rapid Prototyp. J.*, vol. 22, no. 3, pp. 487–494, 2016.

[111] T. Y. Ansell, J. P. Ricks, C. Park, C. S. Tipper, and C. C. Luhrs, "Mechanical properties of 3D-printed maraging steel induced by environmental exposure," *Metals.*, vol. 10, no. 2, pp. 1–11, 2020.

[112] L. Kučerová, I. Zetková, A. Jandová, and M. Bystrianský, "Microstructural characterisation and in-situ straining of additive-manufactured X3NiCoMoTi 18-9-5 maraging steel," *Mater. Sci. Eng. A*, vol. 750, pp. 70–80, 2019.

[113] P. Kürnsteiner, M. B. Wilms, A. Weisheit, P. Barriobero-Vila, E. A. Jägle, and D. Raabe, "Massive nanoprecipitation in an Fe-19Ni-xAl maraging steel triggered by the intrinsic heat treatment during laser metal deposition," *Acta Mater.*, vol. 129, pp. 52–60, 2017.

[114] N. Takata, R. Nishida, A. Suzuki, M. Kobashi, and M. Kato, "Crystallographic features of microstructure in maraging steel fabricated by selective laser melting," *Metals (Basel).*, vol. 8, no. 6, pp. 1–10, 2018.

[115] D. Croccolo, M. De Agostinis, S. Fini, G. Olmi, A. Vranic, and S. Ciric-Kostic, “Influence of the build orientation on the fatigue strength of EOS maraging steel produced by additive metal machine,” *Fatigue Fract. Eng. Mater. Struct.*, vol. 39, no. 5, pp. 637–647, 2016.

[116] T. Burkert and A. Fischer, “The Effects of Heat Balance on the Coid Formation within Marage 300 Processed by Selective Laser Melting,” *Solid Free. Fabr. Symp.*, pp.745–757, 2015.

[117] C. Casavola, S. L. Campanelli, and C. Pappalettere, “Preliminary investigation on distribution of residual stress generated by the selective laser melting process,” *J. Strain Anal. Eng. Des.*, vol. 44, no. 1, pp. 93–104, Dec. 2008.

[118] “Material data sheet EOS MaragingSteel MS1,” vol. 49, no. 0, pp. 1–6, 1954.

[119] D. Wang, C. Song, Y. Yang, and Y. Bai, “Investigation of crystal growth mechanism during selective laser melting and mechanical property characterization of 316L stainless steel parts,” *Mater. Des.*, vol. 100, pp. 291–299, 2016.

[120] J.-H. Shin, J. Jeong, and J.-W. Lee, “Microstructural evolution and the variation of tensile behavior after aging heat treatment of precipitation hardened martensitic steel,” *Mater. Charact.*, vol. 99, pp. 230–237, 2015.

[121] A. Goldberg and D. G. O’connor, “Influence of Heating Rate on Transformations in an 18 per cent Nickel Maraging Steel,” *Nature*, vol. 213, no. 5072, pp. 170–171, 1967.

[122] E. V. Pereloma, A. Shekhter, M. K. Miller, and S. P. Ringer, “Ageing behaviour of an Fe–20Ni–1.8Mn–1.6Ti–0.59Al (wt%) maraging alloy: clustering, precipitation and hardening,” *Acta Mater.*, vol. 52, no. 19, pp. 5589–5602, Nov. 2004.

[123] Z. Guo, W. Sha, and D. Li, “Quantification of phase transformation kinetics of 18 wt.% Ni C250 maraging steel,” *Mater. Sci. Eng. A*, vol. 373, no. 1–2, pp. 10–20, May 2004.

[124] C. Menapace, I. Lonardelli, and A. Molinari, “Phase transformation in a nanostructured M300 maraging steel obtained by SPS of mechanically alloyed powders,” *J. Therm. Anal. Calorim.*, pp.815–821, 2010.

[125] S. Yang, Y. Peng, X. M. Zhang, and Z. L. Tian, “Phase Transformation and Its Effect on Mechanical Properties of C300 Weld Metal after Aging Treatment at Different Temperatures,” *J. Iron Steel Res. Int.*, vol. 22, no. 6, pp. 527–533, 2015.

[126] S. L. Campanelli, N. Contuzzi, and A. D. Ludovico, “Manufacturing of 18 Ni Marage 300 steel samples by selective laser melting,” in *Advanced Materials Research*, vol. 83–86, Trans Tech Publications, Ltd., pp. 850–857. 2010.

[127] H. M. Ledbetter and D. T. Read, “Low-temperature elastic properties of a 300-grade maraging steel,” *Metall. Trans. A*, vol. 8, no. 11, pp. 1805–1808, 1977.

[128] W. Kurz and D. J. Fisher, “Fundamentals of solidification,” *Trans Tech Publications*, pp. 133–156, 1998.

[129] D. M. and C. D. M. S. K. K. Matthew. Lindop, “An Investigation into Fully Melting a Maraging Steel Using Direct Metal Laser Sintering (Dmls),” in *Steel research int. Special Editions Metal forming Conference*, vol. 79, no. 2, pp. 847–852, 2008.

[130] P. V. Ramana and G. M. Reddy, “Influence of surface remelting on distribution of residual stresses in medium alloy-medium carbon steel gas tungsten arc weldment,” *Proc. Inst. Mech. Eng. Part B J. Eng. Manuf.*, vol. 224, no. 5, pp. 739–744, 2010.

[131] J. M. Pardal, S. S. M. Tavares, M. P. Cindra Fonseca, M. R. da Silva, J. M. Neto, and H. F. G. Abreu, “Influence of temperature and aging time on hardness and magnetic properties of the maraging steel grade 300,” *J. Mater. Sci.*, vol. 42, no. 7, pp. 2276–2281, Apr. 2007.

[132] O. Yeheskel, “Ultrasonic characterization of aging behavior in M250 grade maraging steel,” *Metall. Mater. Trans. A Phys. Metall. Mater. Sci.*, vol. 40, no. 3, pp. 684–690, 2009.

[133] P. Behjati, A. Najafizadeh, H. Dastjerdi, M. Araghchi, and R. Mahdavi, “Influence of Aging Temperature on Mechanical Properties and Sound Velocity in Maraging Steel M350,” *Int. J. ISSI*, vol. 7, pp. 17–20, Jan. 2010.

APPENDICES

A. Hardness Measurement Results

Table A.1 Hardness values of heat-treated specimens

	HT 1			HT 2		Hardness (HV)					
	Temperature	Time		Temperature	Time	Yüzey 1		Yüzey 2		Yüzey 3	
						Macro	Micro	Macro	Micro	Macro	Micro
As Built	-			-		378±8	370±3	376±3	377±9	378±4	376±7
1st Group (Aging Temperature)	450 °C	6 hr		-		-	608±3	-	-	-	-
	490 °C	6 hr				601	614±3	601	610±4	603	609±2
	520 °C	6 hr				-	605±3	-	-	-	-
	590 °C	6 hr				-	416±5	-	-	-	-
2nd Group (Aging Time)	490 °C	1 hr		-		548±7	553±7	552±9	560±7	546±7	561±6
	490 °C	2 hr				581	582±6	582	580±6	576	578±4
	490 °C	4 hr				598	601±7	596	603±4	595	597±5
	490 °C	6 hr				601	614±3	601	610±4	603	609±2
	490 °C	8 hr				597	611±6	604	611±3	600	607±5
3rd Group (Solution Treatment Time)	900 °C	0.5 hr		-		-	321±6	-	-	-	-
	900 °C	1 hr				-	322±7	-	-	-	-
	900 °C	2 hr				-	318±3	-	-	-	-
4th Group (Solution Treatment Time & Aged)	900 °C	0.5 hr	&	490 °C	6 hr	-	608±3	-	-	-	-
	900 °C	1 hr		490 °C	6 hr	-	609±3		604±4		608±3
	900 °C	2 hr		490 °C	6 hr	-	610±3	-	-	-	-
5th Group (Solution Treatment & Aging Time)	900 °C	1 hr		-		-	322±7	-	-	-	-
	900 °C	1 hr	&	490 °C	2 hr	-	564±8		557±3		562±3
	900 °C	1 hr		490 °C	4 hr	-	590±10		591±12		596±7
	900 °C	1 hr		490 °C	6 hr	-	609±3	0	604±4	0	608±3
6th Group (Solution Treatment Temperature)	820 °C	1 hr		-		-	324±3	-	-	-	-
	900 °C	1 hr				-	322±7	-	-	-	-
	980 °C	1 hr				-	323±4	-	-	-	-
7th Group (Solution Treatment & Aging Temperature)	900 °C	1 hr	&	450 °C	6 hr	-	605±4	-	-	-	-
	900 °C	1 hr		490 °C	6 hr	-	609±3	0	604±4	0	608±3
	900 °C	1 hr		520 °C	6 hr	-	603±1	-	-	-	-
	900 °C	1 hr		590 °C	6 hr	-	412±6	-	-	-	-

B. Correlations between sound wave velocity and mechanical properties

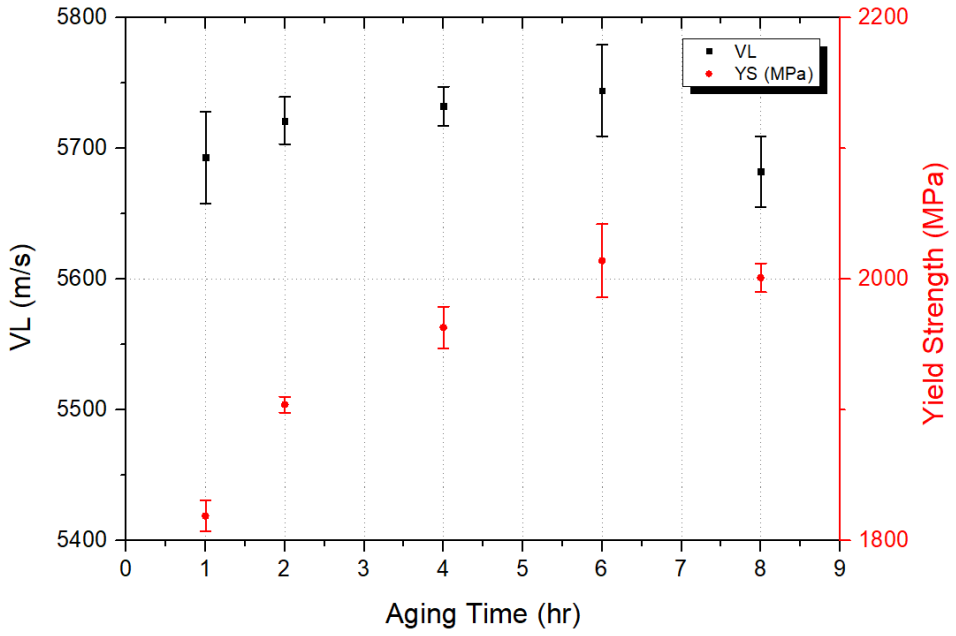

Figure B.1. Variation of longitudinal wave velocity and yield strength with aging time at 490 °C

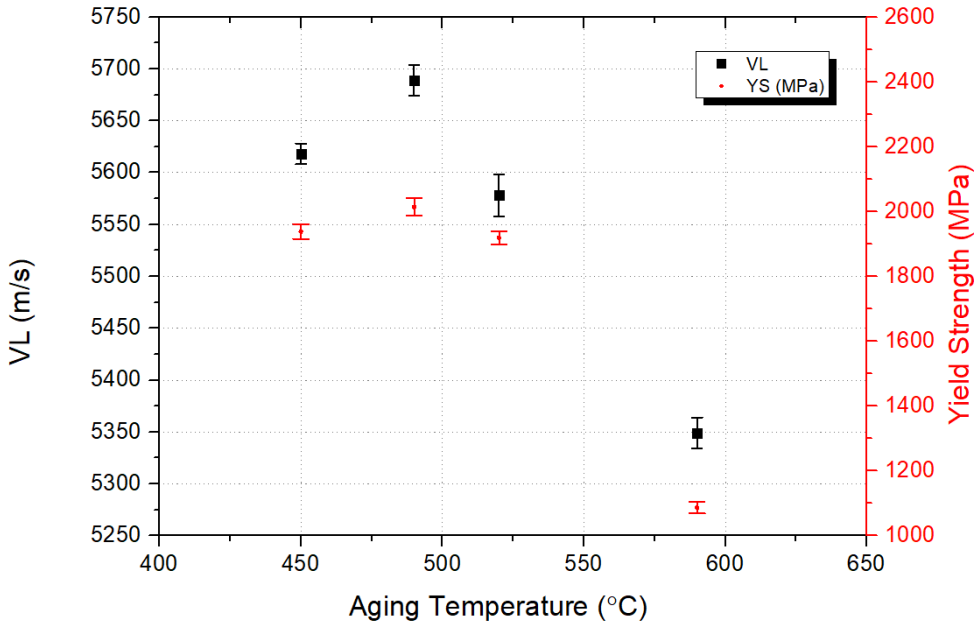

Figure B.2. Variation of longitudinal wave velocity and yield strength with aging temperature for the constant aging time of 6 hr

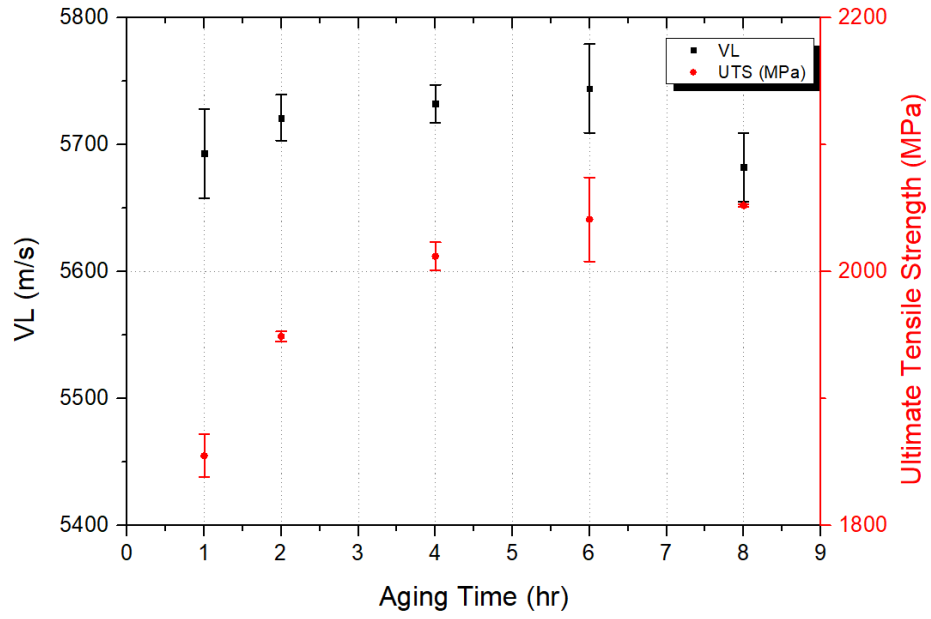

Figure B.3. . Variation of longitudinal wave velocity and ultimate tensile strength with aging time at 490 °C

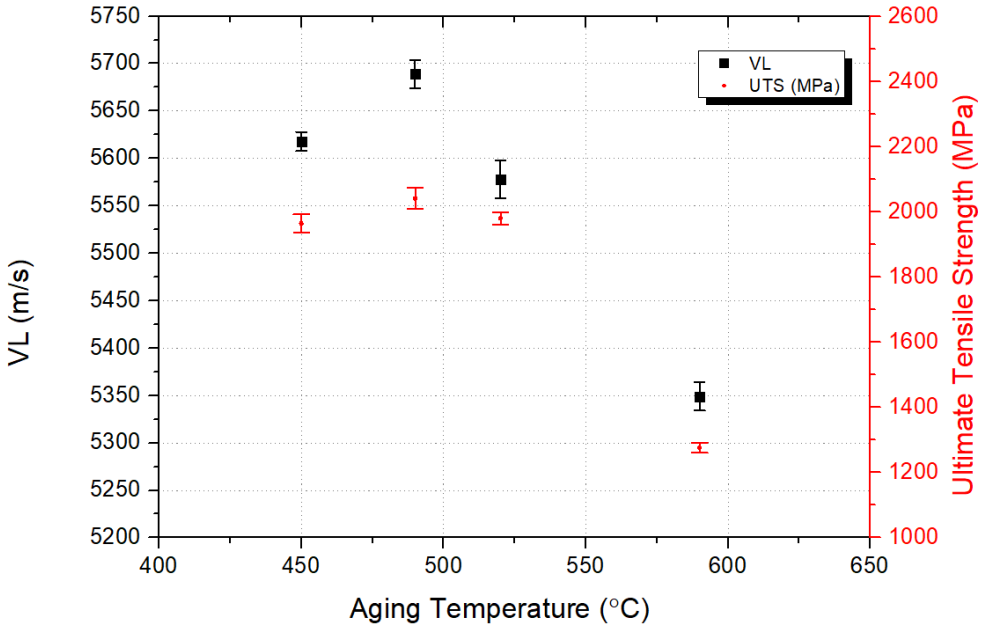

Figure B.4. Variation of longitudinal wave velocity and ultimate tensile strength with aging temperature for the constant aging time of 6 hr

TEZ İZİN FORMU / THESIS PERMISSION FORM

ENSTİTÜ / INSTITUTE

Fen Bilimleri Enstitüsü / Graduate School of Natural and Applied Sciences ☑

Sosyal Bilimler Enstitüsü / Graduate School of Social Sciences ☐

Uygulamalı Matematik Enstitüsü / Graduate School of Applied Mathematics ☐

Enformatik Enstitüsü / Graduate School of Informatics ☐

Deniz Bilimleri Enstitüsü / Graduate School of Marine Sciences ☐

YAZARIN / AUTHOR

Soyadı / Surname : AYDIN
Adı / Name : İBRAHİM
Bölümü / Department : Metallurgical and Materials Engineering

TEZİN ADI / TITLE OF THE THESIS (**İngilizce** / English):
Investigating Effects of Heat Treatment Processes on Microstructural and Mechanical Properties of Additively Manufactured 18Ni300 Maraging Steel

TEZİN TÜRÜ / DEGREE: **Yüksek Lisans** / Master ☑ **Doktora** / PhD ☐

1. **Tezin tamamı dünya çapında erişime açılacaktır. /** Release the entire work immediately for access worldwide. ☑
2. **Tez iki yıl süreyle erişime kapalı olacaktır.** / Secure the entire work for patent and/or proprietary purposes for a period of **two year. *** ☐
3. **Tez altı ay süreyle erişime kapalı olacaktır.** / Secure the entire work for period of **six months**. ***** ☐

***** *Enstitü Yönetim Kurulu Kararının basılı kopyası tezle birlikte kütüphaneye teslim edilecektir.*
A copy of the Decision of the Institute Administrative Committee will be delivered to the library together with the printed thesis.

Yazarın imzası / Signature **Tarih** / Date 09.10.2020